# Dissipative Double-Well Potential

## Mesoscopic Atom Number Detection and Cold Atom Dynamics

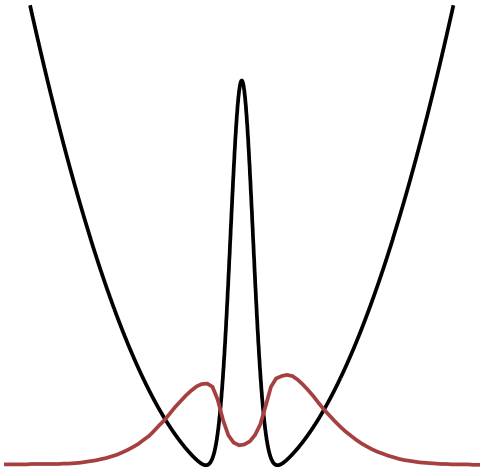

Ion Stroescu

2014

Dissertation
submitted to the
Combined Faculties of the Natural Sciences and Mathematics
of the Ruperto-Carola University of Heidelberg, Germany
for the degree of
Doctor of Natural Sciences

Put forward by

Dipl.-Phys. Ion Stroescu
Born in Bucharest, Romania

Oral examination: 22 July 2014

# Dissipative Double-Well Potential

## Mesoscopic Atom Number Detection and Cold Atom Dynamics

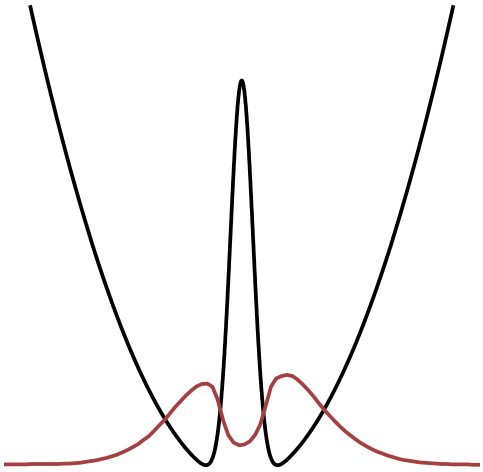

Referees: Prof. Dr. Markus K. Oberthaler
Prof. Dr. Selim Jochim

## Abstract

The ability to manipulate cold atoms has been constantly improved over the past three decades in an endeavour to achieve the best control and the best detection of these particles. Atom-light interaction has proven fundamental for the cooling and trapping of neutral atoms and several detection techniques have been developed, including absorption and fluorescence imaging. Here we present a detection technique based on fluorescence imaging, which is able to reach the ultimate limit of single-atom resolution for mesoscopic samples of up to 1200 particles. In order to render the detection sensitive to multiple hyperfine states of the atomic system, we developed a novel hybrid trap in form of a dissipative double-well potential. This allows the accurate determination of the difference in the hyperfine state population for samples with up to 500 particles. Furthermore, by varying the potential barrier height between the two sites of the double-well, with this unique system it is possible to measure hopping rates over five orders of magnitude. We confirm Arrhenius' law for small barriers and find that particle exchange induced by light-assisted collisions dominates the dynamics for large barriers. Finally, we observe the stochastic resonance effect, in which a weak external driving of the double-well system is amplified by the addition of thermal noise. Accurate measurements enable the extraction of both amplitude and phase lag of the linear system response and we see indications of a non-linear response as well as effects of intra-well motion.

## Zusammenfassung

Die Fähigkeit kalte Atome zu manipulieren wurde über die vergangenen drei Jahrzehnte immer wieder verbessert, in dem Bestreben die beste Kontrolle und die beste Detektion dieser Teilchen zu erreichen. Atom-Licht-Wechselwirkung erwies sich als fundamental für das Kühlen und Fangen von neutralen Atomen und verschiedene Detektionstechniken wurden entwickelt, inklusive Absorptions- und Fluoreszenzbildgebung. Hier präsentieren wir eine Detektionstechnik, die auf Fluoreszenzbildgebung basiert und in der Lage ist das ultimative Limit der Einzelatomauflösung für mesoskopische Proben mit bis zu 1200 Teilchen zu erreichen. Um die Detektion sensitiv auf mehrere Hyperfeinzustände des atomaren Systems zu machen, entwickelten wir eine neuartige Hybridfalle in Form eines dissipativen Doppelmuldenpotentials. Dies erlaubt die genaue Bestimmung der Differenz der Hyperfeinzustandspopulation für Proben mit bis zu 500 Teilchen. Des Weiteren ist es mit diesem einzigartigen System möglich, durch das Variieren der Höhe der Potentialbarriere zwischen den zwei Minima des Doppeltopfs, Hüpfraten über fünf Größenordnungen zu messen. Wir bestätigen das Arrhenius-Gesetz für kleine Barrieren und stellen fest, dass Teilchenaustausch induziert durch lichtunterstützte Kollisionen die Dynamik bei hohen Barrieren dominieren. Schließlich beobachten wir den Effekt der stochastischen Resonanz, bei der ein schwaches externes Treiben des Doppeltopfsystems durch zusätzliches thermisches Rauschen verstärkt wird. Präzise Messungen ermöglichen die Bestimmung sowohl der Amplitude als auch der Phasenverzögerung der linearen Systemantwort und wir sehen Indikationen einer nicht-linearen Antwort sowie Effekte von Bewegung innerhalb einer Senke.

*To my parents*

Mariuca Mihaela Stroescu
Sergiu Dan Stroescu

# Preface

"*We have to remember that what we observe is not nature herself, but nature exposed to our method of questioning.*"
— Werner Heisenberg

I would like to express my deep gratitude to numerous people who have contributed to the success of my doctoral studies. First of all, Markus Oberthaler who has given me the opportunity to work in his group. His excellent supervision has helped me focus on the essential questions and his enthusiasm was an exceeding source of motivation. Selim Jochim was kind enough to discuss various topics and to be the second referee for this thesis, while Thomas Gasenzer and Peter Bachert kindly agreed to take part in my disputation.

Copious thanks are due to David Hume for the intensive cooperation in and outside of the lab. His vast knowledge and physical intuition have helped to promote the experiment many times. We have had ample assistance from several students, as part of the ACE team, including Simon Murmann, Maxime Joos, Patrick Reiser, Lina Norton and Philipp Kunkel.

The BEC team, in particular Helmut Strobel, Wolfgang Müssel and Daniel Linnemann, have frequently contributed to the experimental discussions. Special thanks to Eike Nicklas for donating blood together and Moritz Höfer for rocking Southside Festival 2011. Thanks to the NaLi team, especially to Tobias Rentrop for hitting the gym together and his indispensable humour as well as Arno Trautmann for support with LuaLaTeX and a smashing time at YAO 2011. An honorable mention shall be given to Raphael Scelle for his acute sense of duty and Tobias Schuster for having the courage to speak the truth. Many thanks to the ATTA and the AEgIS teams for rounding out a fantastic work group. The team assistants Dagmar Hufnagel and Christiane Jäger have been very helpful with the administrative tasks and I wish to thank the entire workshop, in particular Werner Lamade, Morris Weißer and Siegfried Spiegel, for their assistance.

I am most thankful to the International Max Planck Research School for Quantum Dynamics in Physics, Chemistry and Biology for the valuable scholarship and several interesting workshops. Special thanks to Antonino Di Piazza for being an excellent coordinator of the school and for those most enjoyable motorcycle trips.

Huge thanks to my friends, including Martin Fast for sharing a good few academic experiences, Oliver Matula for proof-reading, Florian Borchers, Claudia Dilger, Dina Ibrahim, Sylvia Lorenz, Aaron Quick, Steffen Risius, Mirjam Sohler, Stefan Weiser and last, but certainly not least, to my sisters Craita Heiß and Simona Schor.

Heidelberg
10 June 2014

# Contents

# 1 Introduction

Since the advent of laser cooling and trapping of neutral atoms in the 1980s, the manipulation of cold atoms has been steadily refined [1–3]. The history of laser cooling begins with the proposition by Theodor Hänsch in 1975 to cool atomic gases by laser radiation [4]. Four years later, laser cooling of atoms was elaborated more quantitatively [5], however, it took another six years before the first experimental realisation [6]. Shortly after, trapping of atoms via optical dipole force [7] as well as magneto-optical trapping [8] was presented. The observed temperatures were considerably lower than expected from Doppler cooling theory, which required a new theoretical description based on polarisation gradient cooling [9].

We started out with the goal to find the best particle number detector for mesoscopic samples of atomic gases. Single-particle resolution in atom number detection, i. e. atom counting, is crucial in a number of ways. Spin-squeezing and entanglement in Bose-Einstein condensates has been shown [10, 11], as well as the resulting improvement of atom interferometry [12, 13]. Having a detector with single-particle resolution would eliminate technical detection noise, thereby fully harnessing the quantum resource of the interferometer, not only going beyond the standard quantum limit of the interferometric phase scaling with the atom number as $\Delta\phi \sim 1/\sqrt{N}$, but towards the Heisenberg limit $\Delta\phi \sim 1/N$.

Single-particle resolution is required for stringent tests of quantum mechanics, such as the Einstein-Podolsky-Rosen (EPR) paradox [14] and violations of quantum realism. This leads to the Bell inequality [15, 16], which has been first experimentally tested with photons in 1982 by Alain Aspect et al. [17] and later with strict condition of locality by sufficient spatial separation [18]. Bell's inequality has been tested with ions overcoming the detection loophole [19], however, an experiment with neutral atoms is pending. Furthermore, single-atom resolution would allow the detection of mesoscopic highly entangled quantum states like the Greenberger-Horne-Zeilinger (GHZ) state [20], the NOON state [21] or the W state [22]. With these one could study the effect of decoherence on many-particle entanglement. Photonic NOON states have been observed [23], however the mesoscopic atomic counterpart is yet to be realised and detected. Also with photons EPR-steering has been experimentally achieved [24], while so far on the neutral matter side, continuous-variable entanglement [25] has been shown. While it is difficult to create mesoscopic samples of entangled atoms, we show that the detection is within reach.

Using a magneto-optical trap single atoms have been observed [26–28], as well as a few atoms simultaneously [29], via fluorescence imaging. This technique was successfully extended to optical lattices [30–34] and cavities [35, 36]. Freely propagating atoms could be detected in a time-of-flight experiment [37, 38]. Lately, more exotic detection techniques like photoionisation of single atoms were demonstrated [39]. It was even shown that absorption imaging can be used to detect a single atom [40].

Detecting mesoscopic atom numbers, however, is a different story. The most common technique for this is absorption imaging [41], which can be improved by image processing [42] to a resolution

of about four atoms. Cavity based detection of mesoscopic samples has been shown [43], however, accurate atom counting is not possible due to inhomogeneous coupling of the standing-wave light to the atoms. We argue that fluorescence imaging in a magneto-optical trap is a very powerful approach, because of the large trap depth and the long lifetime, which enables ample integration time.

The probabilistic preparation of atom numbers is a topic of ongoing research [44, 45]. While sub-Poissonian loading of single atoms in dipole trap has been feasible for quite some time [46, 47], the focus has turned towards the access to full counting statistics for asymmetric noise, i. e. non-Gaussian distribution for which the third and higher cumulants do not vanish. We present a device which is able to detect Fock states and prepare a mesoscopic ensemble of thermal atoms with a defined atom number.

The requirement of state-selectivity in atom counting lead us to the concept of a novel hybrid trap, enabling magneto-optical trapping in two spatially separated regions. This dissipative double-well system allows the study of intra- and inter-well dynamics with a high level of control over the potential landscape and the temperature of the system. Our primary observations are described by reaction-rate theory [48, 49] which can also be applied to chemical processes. The system is enriched by the manifestation of cold collisions [50]. By changing the potential barrier between the two sites, we gain access to different energy scales. We are able to freeze out thermal hopping and enter a regime where collisional hopping starts to dominate the many-particle dynamics, while single-atom resolution allows us to measure the Poisson statistics of very rare hopping events for few particles in the system.

The dissipative double-well potential also allows us to investigate the stochastic resonance effect, whereby a weak external signal is amplified, i. e. the signal-to-noise ratio is improved, by the *addition* of noise [51]. Historically, the concept has been used to explain the incidence of ice ages [52], yet it has been since become evident that the stochastic resonance effect is so robust and general to bistable systems that it is found in a multitude of instances. Stochastic resonances are present in biological systems [53, 54] and can be beneficial for medical science [55]. Like in evolution, or in fact science itself, increasing the level of *noise* can sometimes yield new results more efficiently.

In Chapter 2 we introduce the concepts of laser cooling and trapping, relevant both for fluorescence imaging as well as the creation of a novel trap configuration in which we study the dynamics of cold atoms. Chapter 3 describes the accurate detection of mesoscopic atom numbers, including a model of the different noise contributions, which was published in [56]. The extension to state-selective atom counting is done in Chapter 4, where the dissipative double-well potential is introduced. In Chapter 5 we investigate the dynamics of cold atoms in this potential by measuring the hopping rates between the two sites and comparing those to reaction-rate theory. Finally, in Chapter 6, the stochastic resonance effect is introduced and experimentally demonstrated for the first time in such a system.

# 2 Laser cooling and trapping of neutral atoms

In this chapter we establish the basic concepts of atom-light interactions that are necessary to understand for both manipulating atoms with light, i. e. cooling and trapping the neutral particles, as well as detecting them via resonant fluorescence imaging. We will discuss Doppler and sub-Doppler cooling, as well as optical molasses, leading to atomic samples at low temperatures, which is beneficial for the detection. A crucial aspect of particle number detection via fluorescence imaging is the trapping of the atoms, at first realised by magneto-optical forces. In combination with the radiative force of an additional single laser beam, this enables the sequential state-selective detection of the atom number in an ensemble. Simultaneous state-selective detection, as well as investigating reaction rates and the stochastic resonance effect, require the addition of an optical dipole force, which realises a potential barrier.

Let us assume a two-level atomic system with states $|1\rangle$ and $|2\rangle$ having energies $E_1$ and $E_2$, respectively. The *resonant* absorption of a photon from a laser beam occurs when the condition

$$E_2 - E_1 = \hbar\omega, \tag{2.1}$$

is met, where $\omega$ is the light frequency. The inverse process, spontaneous emission of a photon by de-excitation of the atom, occurs on average after a typical radiative lifetime of the excited state. Spontaneous emission can be understood as a stimulated emission process randomly initiated by a vacuum photon. Considering the two-level approximation instead of the complex level structure of a real atomic system is valid when Eqn. 2.1 is fulfilled. The classical picture is that the light frequency $\omega$ is tuned to the frequency $(E_2 - E_1)/\hbar$ of the induced dipole oscillation of the atom, while all other transitions are *off-resonant*.

We can allow for small deviations from the strict resonance condition by setting $\omega = \omega_0 + \delta$, where $\delta \ll \omega_0$ is the *detuning* of the laser frequency $\omega$ with respect to the atomic transition $\omega_0$. The time-dependent Schrödinger equation for the two-level system reads

$$\hat{H}\Psi = i\hbar\frac{\partial\Psi}{\partial t}, \tag{2.2}$$

where the Hamiltonian can be split into a part which describes the unperturbed atom and one which describes the time-dependent interaction between the light and the atom

$$\hat{H} = \hat{H}_0(\boldsymbol{r}) + \hat{V}(t). \tag{2.3}$$

In the two-state approximation, Eqn. 2.2 is solved by

$$\Psi(\boldsymbol{r}, t) = c_1(t)\psi_1(\boldsymbol{r})e^{-iE_1t/\hbar} + c_2(t)\psi_2(\boldsymbol{r})e^{-iE_2t/\hbar}, \tag{2.4}$$

where the stationary properties are described by

$$\hat{H}_0(\boldsymbol{r})\psi_i(\boldsymbol{r}) = E_i\psi_i(\boldsymbol{r}), \tag{2.5}$$

for the two states $i = 1, 2$. The time evolution of the coefficients is given by

$$\dot{c}_1(t) = -\frac{i}{\hbar}\left(c_1(t)V_{11} + c_2(t)V_{12}e^{-i\omega_0 t}\right), \tag{2.6}$$

$$\dot{c}_2(t) = -\frac{i}{\hbar}\left(c_1(t)V_{21}e^{i\omega_0 t} + c_2(t)V_{22}\right), \tag{2.7}$$

where

$$V_{ij}(t) \equiv \langle i|\hat{V}(t)|j\rangle = \int \psi_i^*\hat{V}(t)\psi_j \,\mathrm{d}^3\boldsymbol{r}. \tag{2.8}$$

Semi-classically, we can write the interaction between the light and the atomic dipole as $\hat{V}(t) = e\boldsymbol{r}\cdot\boldsymbol{E}(t)$, where $e$ is the magnitude of the electron charge and $\boldsymbol{E}(t) = (E_x, 0, 0)\cos(\omega t)$ is the electric field of the light, chosen here with a polarisation along the $x$-axis [57]. This assumes the dipole approximation $\boldsymbol{k}\cdot\boldsymbol{r} \ll 1$, where $\boldsymbol{k}$ is the wave vector of the laser beam. The perturbation matrix elements can be rewritten as

$$V_{ij} = -\frac{E_x}{2}\left(e^{i\omega t} + e^{-i\omega t}\right)\mu_{ij}, \tag{2.9}$$

with the dipole matrix element

$$\mu_{ij} = -e\int \psi_i^* x\psi_j \,\mathrm{d}^3\boldsymbol{r}. \tag{2.10}$$

In the atomic dipole approximation $\mu_{11} = \mu_{22} = 0$, since $x$ has odd parity. Furthermore, because the dipole matrix elements are measurable, $\mu_{12}^* = \mu_{21}$, and thus $\mu_{12} = \mu_{21}$. Eqs. 2.6 and 2.7 can now be rewritten as

$$\dot{c}_1(t) = \frac{i}{2}\Omega_0\left(e^{i(\omega-\omega_0)t} + e^{-i(\omega+\omega_0)t}\right)c_2(t), \tag{2.11}$$

$$\dot{c}_2(t) = \frac{i}{2}\Omega_0\left(e^{-i(\omega-\omega_0)t} + e^{i(\omega+\omega_0)t}\right)c_1(t), \tag{2.12}$$

with the *Rabi frequency* $\Omega_0 \equiv |\mu_{12}E_x/\hbar|$. This set of coupled differential equations can be solved by making two approximations [58]. First, the *rotating-wave approximation* neglects rapidly oscillating terms with $\pm(\omega + \omega_0)$, since $\delta \ll (\omega + \omega_0)$ [59]. Second, we consider for now the resonant case of $\delta = 0$, and obtain

$$\dot{c}_1(t) = \frac{i}{2}\Omega_0 c_2(t), \tag{2.13}$$

$$\dot{c}_2(t) = \frac{i}{2}\Omega_0 c_1(t). \tag{2.14}$$

These equations can be decoupled and for the starting conditions $c_1(0) = 1$ and $c_2(0) = 0$, i. e. the atom being initially in the ground state, the solution is given by

$$c_1(t) = \cos(\Omega_0 t/2), \tag{2.15}$$

$$c_2(t) = i\sin(\Omega_0 t/2). \tag{2.16}$$

The oscillation between the probabilities to find the electron in state $|1\rangle$ or $|2\rangle$, given by $|c_1(t)|^2$ and $|c_2(t)|^2$, respectively, is called *Rabi flopping*. In case of finite detuning $\delta$, one obtains

$$|c_2(t)|^2 = \frac{\Omega_0^2}{\Omega^2}\sin^2(\Omega t/2), \tag{2.17}$$

where $\Omega = \sqrt{\Omega_0^2 + \delta^2}$ is the *effective* Rabi frequency.

If the laser frequency is set correctly, either close to the resonant transition or far detuned, the light can be used to cool and trap neutral atoms, enabling us to collect the emitted fluorescence over a much longer time, compared to a freely propagating atomic sample at room temperature.

## 2.1 Doppler cooling

In an ensemble of atoms in thermal equilibrium at temperature $T$ each particle has a thermal energy of $\frac{1}{2}k_\mathrm{B}T$ per degree of freedom, where $k_\mathrm{B}$ is the Boltzmann constant. Equating the thermal energy to the particle's kinetic energy $\frac{1}{2}mv_x^2$, we obtain the root-mean-square of the thermal velocity

$$v_x^{\mathrm{rms}} = \sqrt{\frac{k_\mathrm{B}T}{m}}. \tag{2.18}$$

Laser cooling relies on a mechanical force to slow down atoms, thereby achieving low temperatures [60]. Such low temperatures have been reached in solid states, however, here we are dealing with a low density *gas* of atoms, allowing us to study weakly interacting systems.

Let us consider an atom, moving along the $x$-direction with a thermal velocity $v_x$, and a counter-propagating laser beam with frequency $\omega = \omega_0 + \delta$. Due to the Doppler effect, the frequency of the laser is shifted up in the rest frame of the atom. The resulting frequency is

$$\omega' = \omega\left(1 + \frac{v_x}{c}\right) \simeq \omega_0 + \delta + \omega_0\frac{v_x}{c}, \tag{2.19}$$

assuming that $v_x$ is much smaller than the speed of light $c$. The shifted laser frequency is brought to resonance with the atomic transition, $\omega' = \omega_0$, for a detuning $\delta = -\omega_0 v_x/c$. This holds for atoms moving in $x$-direction, but not in any other direction [4].

Each time the atom absorbs a photon from the laser beam, its momentum is changed by $\Delta p_x = -h/\lambda$, where $\lambda$ is the wavelength of the laser. Eventually, the atom will emit a photon, typically after the characteristic lifetime $\tau$ of the excited state. Since the emission can occur in any direction, on average the momentum transfer from photon re-emission is zero. Hence, the atom experiences a net frictional force in $-x$-direction, which can be approximated by

$$F_x = \frac{\mathrm{d}p_x}{\mathrm{d}t} \approx \frac{\Delta p_x}{2\tau} = -\frac{h}{2\lambda\tau}. \tag{2.20}$$

The factor of two is introduced due to the fact that in this incoherent process the maximum population of the excited state is $1/2$, as will become clear later on.

The optimal detuning, at which the laser frequency resonates with the atomic transition, depends on the velocity of the particle. The slower the particle, the smaller the required detuning. Once the

detuning is on the order of the natural linewidth $\Gamma \equiv 1/\tau$ of the transition, the limit of Doppler cooling is reached. The minimum thermal energy of the atom can be estimated by $k_{\mathrm{B}} T_{\mathrm{min}} \sim \hbar\Gamma$, such that the minimum temperature

$$T_{\mathrm{min}} \sim \frac{\hbar}{k_{\mathrm{B}}\tau} \tag{2.21}$$

is limited by the lifetime of the transition.

## 2.2 Optical molasses

So far we have used a simple picture in order to intuitively understand the process of laser cooling. Let us now take a more detailed approach and consider again a laser beam with detuning $\delta$ and an atom with velocity $v_x$. We now also take into account the laser beam intensity $I$. The net force on the atom upon interaction with the light is given by the momentum change in each cycle of absorption and re-emission times the rate at which this process occurs, namely

$$F_x = -\hbar k \times R_{\mathrm{sc}}(I, \delta), \tag{2.22}$$

where $k \equiv 2\pi/\lambda$ is the photon wave vector [61]. The *scattering rate* $R_{\mathrm{sc}}$ corresponds to the absorption rate minus the rate of stimulated emission[1] and is given by

$$R_{\mathrm{sc}}(I, \delta) = \frac{\Gamma}{2}\left(\frac{I/I_{\mathrm{sat}}}{1 + I/I_{\mathrm{sat}} + 4(\delta + k v_x)^2/\Gamma^2}\right), \tag{2.23}$$

where $I_{\mathrm{sat}}$ is the saturation intensity [62]. For large intensities, $I \to \infty$, the scattering rate approaches $R_{\mathrm{sc}} = \Gamma/2$ as a limit, where we encounter the maximum excited state population of $1/2$, which we have introduced earlier. In the low intensity limit, $I/I_{\mathrm{sat}} \ll 1$, the scattering rate grows linearly with $I$.

We now add a second laser beam in the $x$-direction, counter-propagating with the first beam. The total force acting on the atom is

$$F_x = F_+ + F_-, \tag{2.24}$$

where $F_\pm$ denotes the individual forces arising from the laser beams traveling in $\pm x$-direction. For cold atoms the thermal velocity is reduced so much that $|k v_x| \ll \delta$, where the detuning $\delta$ is now chosen such that it is comparable to $\Gamma$, in which case we obtain

$$F_x = \frac{8\hbar k^2 \delta}{\Gamma}\left(\frac{s_0}{1 + s_0 + 4\delta^2/\Gamma^2}\right) v_x \equiv -\alpha v_x, \tag{2.25}$$

with the saturation parameter $s_0 = I/I_{\mathrm{sat}}$. For a negative detuning, the *damping coefficient* $\alpha$ is positive and the resulting damping is independent of the direction of $v_x$. This effect is called

[1] In the stimulated emission process, a photon interacts with an atom in its excited state, whereby the light particle is absorbed and two identical photons are re-emitted, resulting in a momentum transfer in the opposite direction of the incident photon.

*optical molasses*, due to the apparent "viscosity" the atom encounters when moving in the light field.

To find the temperature limit, we compare the cooling effect of the damping force

$$\left(\frac{\mathrm{d}E}{\mathrm{d}t}\right)_{\text{cool}} = F_x v_x = -\alpha v_x^2 \tag{2.26}$$

to the heating effect due to repeated absorption and re-emission of photons, given by

$$\left(\frac{\mathrm{d}E}{\mathrm{d}t}\right)_{\text{heat}} = \frac{D_p}{m}, \tag{2.27}$$

where $D_p$ is the momentum diffusion constant. The atoms undergo a random walk in momentum space, where $\langle p_x \rangle = 0$, but the second moment does not vanish and is given by $\langle p_x^2 \rangle = 2N(\hbar k)^2$, with the number of steps $N = 2R_{\text{sc}}t$ during the time $t$. The momentum diffusion constant can be expressed as

$$D_p \equiv \frac{1}{2}\frac{\mathrm{d}\langle p_x^2 \rangle}{\mathrm{d}t} = 4\hbar^2 k^2 R_{\text{sc}}. \tag{2.28}$$

Requiring the total energy change, i. e. the sum of the cooling and the heating rate given by Eqn. 2.26 and 2.27, respectively, to vanish, we obtain

$$\frac{D_p}{m} - \alpha v_x^2 = 0 \tag{2.29}$$

and thus $D_p = m\alpha v_x^2$. Using Eqn. 2.18 to eliminate $v_x$, the temperature of the ensemble can be expressed as

$$T = \frac{D_p}{\alpha k_{\text{B}}} = -\frac{\hbar\Gamma}{8k_{\text{B}}}\left(\frac{1 + s_0 + 4\delta^2/\Gamma^2}{\delta/\Gamma}\right). \tag{2.30}$$

For small intensities, $I \ll I_{\text{sat}}$, the lowest temperature is found at a detuning of $\delta = -\Gamma/2$ [3]. The so-called *Doppler limit* is given by

$$T_{\text{D}} = \frac{\hbar\Gamma}{2k_{\text{B}}} \equiv \frac{\hbar}{2k_{\text{B}}\tau}. \tag{2.31}$$

For laser cooling of $^{87}$Rb we use the $|5\ ^2\mathrm{S}_{1/2}\rangle \longleftrightarrow |5\ ^2\mathrm{P}_{3/2}\rangle$ transition with a lifetime of $\tau = 26\,\text{ns}$, resulting in a Doppler temperature $T_{\text{D}} = 146\,\mu\text{K}$. This corresponds to a minimum thermal velocity of 12 cm/s.

## 2.3 Sub-Doppler cooling

Experiments on sodium [63] and caesium [64] atoms have shown temperatures much lower than the Doppler limit, indicating that the simple considerations we have made so far omit important aspects of laser cooling. In order to explain the low temperatures in the experiments, the theory of *polarisation gradient cooling* was developed [9, 65, 66].

Let us consider an alkali atom, moving along the $x$-direction, with ground state $^2\mathrm{S}_{1/2}$ and excited state $^2\mathrm{P}_{3/2}$. The ground state has a total angular momentum of $J = 1/2$, which splits

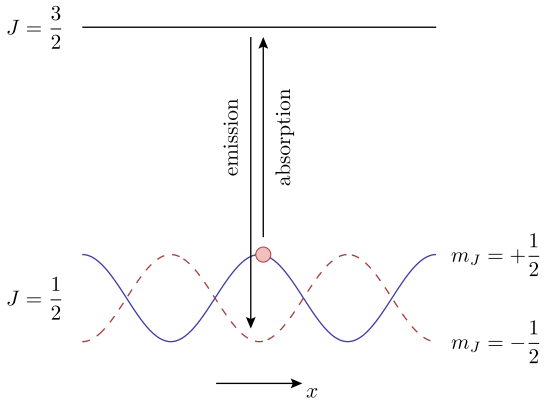


Figure 2.1: Scheme of the polarisation gradient cooling process. An atom travelling in $x$-direction only absorbs a photon, when it is at the maximum of the spatially oscillating energy landscape. If the decay from the $J = 3/2$ excited state occurs into the other $m_J$ state of the $J = 1/2$ ground state manifold, the total energy of the atom is reduced, and thus the temperature lowered.

into two Zeeman sub-levels with $m_J = \pm 1/2$. The atom shall be moving in the light field of two counter-propagating laser beams. The interference of the laser beams gives rise to a polarisation gradient, which is intrinsic to the configuration. This leads to a periodic spatial modulation of the multilevel structure of the $^2\mathrm{S}_{1/2}$ ground state, as shown in Fig. 2.1. The opposite differential light-shifts of the two sub-levels enable the following process. If the laser detuning is set correctly, the atom can only absorb a photon when it is a the top of the sinusoidal energy landscape. The subsequent decay from the $^2\mathrm{P}_{3/2}$ excited state can either occur into the initial $m_F$ sub-state or the other one, which at that position has a lower energy[2]. If the atom decays into the lower sub-state, the energy difference is carried away by the emitted photon and thus the total energy of the atom is reduced, leading to a cooling effect.

The temperature limit of this process is given by the recoil an atom experiences each time it emits a photon with momentum $h/\lambda$. If we equate the minimum thermal energy $\frac{1}{2}k_\mathrm{B}T_\mathrm{r}$ with the kinetic energy $\frac{1}{2m}(h/\lambda)^2$, we obtain the recoil temperature

$$T_\mathrm{r} = \frac{h^2}{mk_\mathrm{B}\lambda^2}, \tag{2.32}$$

which in the case of the $\mathrm{D}_2$ transition in $^{87}$Rb is $T_\mathrm{r} = 362\,\mathrm{nK}$. This corresponds to a recoil velocity of $v_\mathrm{r} = h/m\lambda = 5.9\,\mathrm{mm/s}$.

[2]Selection rules actually favour the energetically lower state, leading to an even more efficient cooling process.

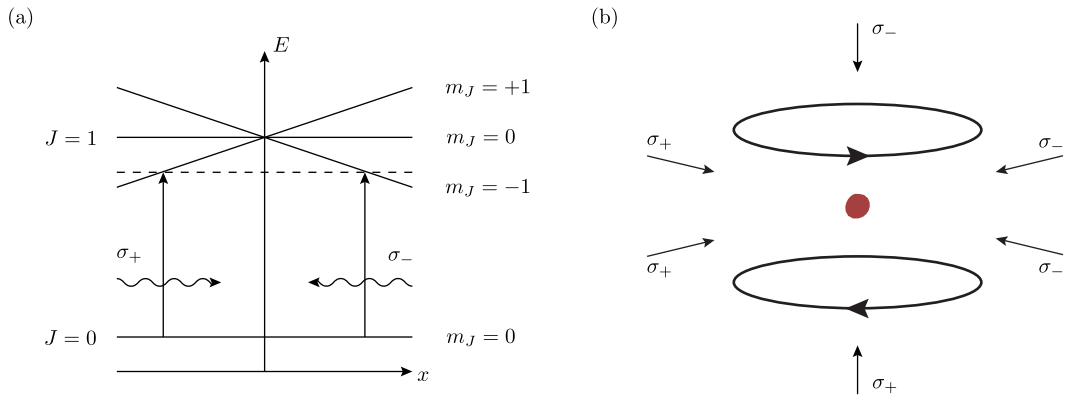


Figure 2.2: Scheme of magneto-optical cooling. (a) The energy of the $J = 1$ excited state of the atom is shifted by the magnetic field gradient. In the light field of two counter-propagating laser beams with opposite circular polarisation this leads to a position dependent restoring force. In this simplified picture we assume the ground state to have $J = 0$, without any sub-structure. (b) The magnetic field gradient is created by a pair of coils in the anti-Helmholtz configuration, in which the current is flowing in opposite directions. Three pairs of counter-propagating laser beams evoke cooling and trapping of the atoms in three dimensions.

## 2.4 Magneto-optical trapping

The laser cooling technique can be extended to three spatial dimensions by introducing two additional pairs of counter-propagating laser beams, both orthogonal to the first pair and to each other. This configuration alone, however, does not provide any confinement of the atoms, but merely slows them down. In order to trap the atoms, a position dependent force is required. For this a magnetic field gradient can be applied, creating a *magneto-optical trap* (MOT), which typically has a large volume and a large depth compared to the temperature of the atoms. Let us consider the one-dimensional case with an atom having a $J = 0$ ground state and a $J = 1$ excited state. There are again two counter-propagating laser beams present, both with the same detuning and the same intensity, but opposite circular polarisations $\sigma_\pm$. Due to the Zeeman effect, the energy levels are shifted in a magnetic field $B_x = B' \cdot x$, where $B'$ is the magnetic field gradient, such that the resonance condition for the optical transition to occur is met a different positions along $x$. The spatially dependent force imbalance between the two laser beams gives rise to a net restoring force, which pushes the atoms to the centre of the trap, where the net force vanishes, as depicted in Fig. 2.2. The total force, comprised of the frictional force from laser cooling and the restoring force from trapping, can be expanded about the centre of the trap, which yields

$$F_x \simeq -\alpha v_x - \kappa x, \tag{2.33}$$

where $\alpha$ is the damping coefficient defined in Eqn. 2.25 and the spring constant is given by

$$\kappa = 2k\mu B' s_0 \frac{-\delta\Gamma}{\delta^2 + \Gamma^2/4}, \tag{2.34}$$

where $\mu$ is the magnetic moment of the excited state [67].

As before, for laser cooling of alkali atoms, the cycling transition $|F = 2\rangle \longleftrightarrow |F' = 3\rangle$ is used. However, there can be some off-resonant population of the $|F' = 2\rangle$ excited state, followed by a decay into the $|F = 1\rangle$ ground state, which is not trapped. In order to prevent the loss of the atom, a repumping beam is needed, pumping the atom in $|F = 1\rangle$ back to $|F' = 2\rangle$, from where it can decay into the $|F = 2\rangle$ ground state. Among many beneficial properties of a MOT are its robustness and the relatively large recapture velocities of up to typically 20 m/s for rubidium. Magneto-optical trapping has been first demonstrated in the late 1980s [8, 68] and is still a valuable technique today.

One can estimate the expected size of the MOT assuming thermal equilibrium[3]. The equipartition theorem then states

$$\kappa\langle x^2\rangle = k_\mathrm{B} T. \tag{2.35}$$

Using Eqn. 2.34 with a detuning of $\delta = -\Gamma/2$, a saturation parameter of $s_0 = 1$, a typical magnetic field gradient of $B' = 0.1\,\mathrm{T\,m^{-1}}$ and assuming the magnetic moment of the excited state to be given by Bohr's magneton, i. e. $\mu = \mu_\mathrm{B}$, one obtains $\kappa = 1.5 \times 10^{-17}\,\mathrm{N\,m^{-1}}$ and a size of $\sqrt{\langle x^2\rangle} \sim 10\,\mu\mathrm{m}$ for a temperature of $T = 100\,\mu\mathrm{K}$. This assumes that the atomic density is small enough, such that there is no reabsorption of scattered photons. If the density is high enough, the gas is no longer non-interacting and *light-assisted collisions* can occur [70, 71].

## 2.5 Optical dipole traps

So far we have considered a detuning of the laser frequency comparable to the natural linewidth, which is close to the resonant transition frequency. We will now investigate a different regime, where the laser is detuned far from resonance and the atoms experience an optical dipole force. An electric field $\boldsymbol{E}(t) = (E_0, 0, 0)e^{-i\omega t}$, with polarisation chosen here along the $x$-axis, induces an atomic dipole moment $\boldsymbol{p}(t) = (p_0, 0, 0)e^{-i\omega t}$ oscillating at the driving frequency $\omega$. The relation between the amplitude of the dipole moment and the electric field amplitude is given by $p_0 = \alpha E_0$, where

$$\alpha = \frac{e^2}{m_e} \frac{1}{\omega_0^2 - \omega^2 - i\omega\Gamma_\omega} \tag{2.36}$$

is the complex polarisability [72], which depends on the classical damping rate

$$\Gamma_\omega = \frac{e^2\omega^2}{6\pi\varepsilon_0 m_e c^3} \equiv \left(\frac{\omega}{\omega_0}\right)^2 \Gamma, \tag{2.37}$$

where $\Gamma$ is the on-resonance damping rate. In the semiclassical picture of a two-level atom interacting with the light field, $\Gamma$ corresponds to the natural linewidth, i. e. the inverse lifetime of the excited state.

[3] This is technically not true, since the MOT is not an isolated system [69].

The two main properties of optical dipole traps are the interaction potential

$$U_{\text{dip}} = -\frac{1}{2}\langle \boldsymbol{p}\boldsymbol{E}\rangle = -\frac{1}{2\varepsilon_0 c}\,\mathrm{Re}(\alpha) I \tag{2.38}$$

and the scattering rate

$$\Gamma_{\text{sc}} = \frac{1}{\hbar\varepsilon_0 c}\,\mathrm{Im}(\alpha) I, \tag{2.39}$$

which both depend on the intensity $I = 2\varepsilon_0 c|E_0|^2$ of the light field. Here we are interested in the far-detuned case, where $\Gamma_{\text{sc}} \ll \Gamma$ and the conservative potential $U_{\text{dip}}$ gives rise to an optical dipole force $\boldsymbol{F}_{\text{dip}} = -\nabla U_{\text{dip}}$. In the rotating-wave approximation, discussed earlier in this chapter, we can write

$$U_{\text{dip}}(\boldsymbol{r}) = \frac{3\pi c^2}{2\omega_0^3}\frac{\Gamma}{\Delta} I(\boldsymbol{r}) \tag{2.40}$$

and

$$\Gamma_{\text{sc}}(\boldsymbol{r}) = \frac{3\pi c^2}{2\hbar\omega_0^3}\left(\frac{\Gamma}{\Delta}\right)^2 I(\boldsymbol{r}) \equiv \frac{\Gamma}{\hbar\Delta} U_{\text{dip}}(\boldsymbol{r}), \tag{2.41}$$

where $\Delta \equiv \omega - \omega_0$ is the detuning of the laser frequency to the resonance [72]. For red detuning, $\Delta < 0$, the interaction potential is negative and the atoms are attracted to the intensity maximum, forming an optical dipole trap. However, the idea is to split the magneto-optical trap in two parts, in which we can count the atoms individually. Therefore we superimpose a focused light-sheet onto the centre of the MOT. In order to create a potential barrier, from which the atoms are repelled, we choose a blue detuning, $\Delta > 0$ [73]. Usually it is favourable to use a large detuning, as to keep the scattering rate at a minimum. However, since the atoms experience constant cooling in the MOT, we can decrease the detuning to a few tens of GHz, before the scattering rate from the potential barrier starts to contribute significantly, meanwhile achieving the largest barrier height for a given intensity. The benefit of blue detuning is that the atoms are in the intensity minimum, such that the scattering rate is reduced compared to its maximum value at peak intensity.

# 3 Accurate detection of mesoscopic atom numbers

When it comes to detecting the particle number in experiments with neutral atoms, a widely used method is absorption imaging. A resonant laser beam is directed onto the atomic cloud, where part of the light is scattered and the reduced transmission is used to infer the atomic density. This method is favourable for large atom numbers ($\sim 10^4$ and higher), especially in combination with time-of-flight, which reduces the optical density. Due to the short imaging pulses on the order of a few µs, a certain degree of spatial resolution is given, which is limited by the expansion of the cloud due to heating. However, this imaging technique is limited in atom number resolution to about 4 particles [41, 42] for mesoscopic samples of hundreds of atoms. A single atomic ion has been detected with absorption imaging [40], albeit with an exposure time of 1 s and the signal-to-noise ratio does not scale favourably with the particle number.

An alternative imaging technique is fluorescence imaging, whereby the atoms are excited and the isotropically re-emitted light is collected. Laser cooling naturally exhibits the effect of repeatedly exciting the atoms with the advantage of simultaneously prolonging the interrogation time. If the atoms are additionally trapped, the detection time can be very long and is limited only by loss from the trap. We will see that this method is suitable not only for detecting single atoms with very high fidelities, but also for achieving single-particle resolution in mesoscopic ensembles with more than one thousand atoms. Measurements for small atom numbers have been performed in free space [37] and magneto-optical traps [26, 45, 74], as well as in optical dipole traps [44] and cavities [36, 75, 76]. Optical lattices have the disadvantage of high atomic densities, where light-assisted collisions quickly lead to pair-wise loss of the atoms, allowing only for the measurement of the parity, but not the actual atom number [30, 32, 77, 78]. Cavity based atom number detection is limited by inhomogeneous coupling of the atoms to the standing-wave probe light, allowing for a good signal stability up to 150 atoms, but not showing discrete steps with the addition of each further atom [43].

It is possible to count individual atoms by collecting the fluorescence from a magneto-optical trap, which intrinsically is very deep ($\sim 1\,\mathrm{K}$) compared to the temperature of the trapped atoms ($\sim 100\,\mu\mathrm{K}$) and therefore can have a long lifetime of hundreds of seconds. Considering the measurement of $N$ atoms, the accuracy is limited by two processes: fluorescence noise and atom loss. Photon shot noise contributes to the variance of the signal with $N/n_{\mathrm{ph}}$, where $n_{\mathrm{ph}} = \eta R_{\mathrm{sc}} t$ is the number of photons collected during the time $t$, given a photon scattering rate of the atoms of $R_{\mathrm{sc}}$ and an overall detector efficiency of $\eta$. Atom loss, on the other hand, contributes to the variance with $Nt/2\tau$, where $\tau$ is the lifetime of the MOT. In this simple model, the total variance

$$\sigma_N^2 = \frac{N}{\eta R_{\mathrm{sc}} t} + \frac{Nt}{2\tau} \tag{3.1}$$

is minimised for an optimal detection time of $t_{\text{opt}} = \sqrt{2\tau/\eta R_{\text{sc}}}$, independent of the atom number. By setting $\sigma_N^2 = 1$ to obtain the single-particle resolution threshold, we obtain an upper bound $N_{\text{max}} = \sqrt{\tau\eta R_{\text{sc}}/2}$. In the case of $^{87}$Rb, if we assume a saturation parameter $s_0 = 1$, a detuning of $\delta = -\Gamma/2$, a detector efficiency of $\eta = 0.01$ and a trap lifetime of $\tau = 100\,\text{s}$, we find $t_{\text{opt}} = 56\,\text{ms}$ and $N_{\text{max}} = 1800$. We will see that there are further contributions to the variance, limiting the maximum atom number that can be detected with single-particle resolution, however, by optimising experimental parameters, it is in principle possible to even surpass the limit of this simple consideration.

## 3.1 Laser system

Being fairly robust, the magneto-optical trap itself does neither require a very high stability of the laser frequency and intensity, nor a very good vacuum inside the experimental chamber. However, these are key issues when it comes to atom number detection, since a modulation of the laser frequency and intensity changes the scattering rate of the atoms, while residual background gas reduces the lifetime in the trap. We employ a tapered amplifier (TA) for the generation of the laser cooling light. The amplified spontaneous emission from the TA does not have a considerable impact on the MOT, since the scattering rate is already close to its maximum of $\Gamma/2$. A fast photo-diode detects the intensity of the laser, before it is divided into three counter-propagating pairs of MOT beams, and feeds the signal back to an acousto-optical modulator (AOM) which stabilises the power. The peak intensity, summed over all six beams, is $23\,\text{mW cm}^{-2}$, corresponding to a saturation parameter of $s_0 \simeq 7$. The laser frequency is locked to a Rb spectroscopy of the $|^2\text{S}_{1/2}, F = 2\rangle \longleftrightarrow |^2\text{P}_{3/2}, F = 3\rangle$ transition using a lock-in amplifier and a detuning of $\delta \simeq -\Gamma/2$ is set by the same AOM. With these parameters we estimate a scattering rate per atom of $R_{\text{sc}} = 15 \times 10^6\,\text{s}^{-1}$.

An additional single laser beam, resonant with the $|^2\text{S}_{1/2}, F = 1\rangle \longleftrightarrow |^2\text{P}_{3/2}, F = 2\rangle$ transition, with a waist of 3 mm and an intensity of $3.0\,\text{mW cm}^{-2}$ is employed in order to repump atoms that have decayed into the $|^2\text{S}_{1/2}, F = 1\rangle$ state.

In order to reduce the amount of stray light in the system, we use a motorised iris that reduces the MOT beam size to about 1 mm during the detection, while facilitating a higher loading rate with bigger beams during other stages of the experiment. A spatial filter after the motorised iris is implemented to reduce interference fringes on the MOT beams that can lead to intensity imbalance across the MOT and thus to fluorescence noise and heating [79]. The repumping is done via a single laser beam with a waist below 1 mm. Another measure to reduce stray light is the introduction of an intermediate image, as described in the following section.

## 3.2 Imaging system and detector non-linearity

The fluorescence light from the atoms, which are trapped inside an evacuated glass cell, is collected by an aspheric lens[1] with a numerical aperture (NA) of 0.23 and imaged onto a low-noise CCD

[1] Thorlabs AL2550-B, 50 mm effective focal length, 46 mm working distance.

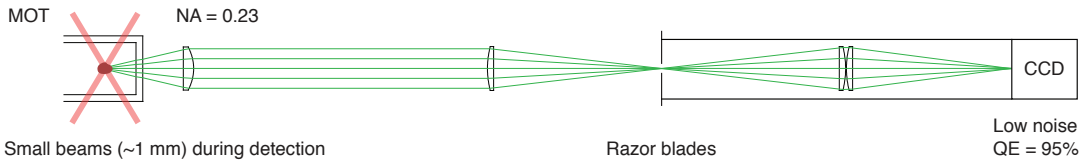


Figure 3.1: Ray traced illustration of the imaging system. An aspheric objective and a spherical secondary lens image the fluorescence from the trapped atoms onto an intermediate plane framed by razor blades. From there the signal is imaged 1:1 onto the CCD camera.

camera[2], as shown in Fig. 3.1. The covered solid angle is $\Omega = \mathrm{NA}^2/4 \approx 1.3\%$. A high quantum efficiency (QE) of $95\%$ of the CCD camera reduces the impact of photon shot noise onto the signal, while the read-out noise per pixel has to be small enough, such that the noise summed over the entire region of interest is smaller than the signal from a single atom. Taking into account the $4\%$ signal loss each time the fluorescence passes through one of the uncoated glass cell walls, the transmission coefficient is $T = 0.96^2$. The total detector efficiency is then given by $\eta = \Omega \cdot T \cdot \mathrm{QE} \approx 1.1\%$.

An intermediate image, located in the focus of the spherical secondary lens with $100\,\mathrm{mm}$ focal length, is framed by a small aperture, formed by razor blades, that strongly reduces the amount of stray light coming from reflections of the laser cooling light off the glass cell walls or other parts of the experimental setup. The intermediate image is transmitted by two spherical lenses with $100\,\mathrm{mm}$ focal length 1:1 onto the edge of the CCD on the opposite side of the read-out register. After an exposure, the charge built up in the illuminated pixels is shifted towards the register to allow for a subsequent exposure. This frame shifting technique enables us to expose up to 10 times, before closing the CCD shutter and starting the electronic read-out. Since the read-out typically takes about 4 seconds, the frame transfer greatly increases the duty cycle. It also allows for accurate timing between the exposures. A narrowband optical filter[3] centred at $780\,\mathrm{nm}$ reduces ambient stray light.

Quantitative measurements with CCD cameras rely on a good linearity between the number of collected photons and the digital output of the signal amplifier, even when approaching the full well capacity, i. e. when a pixel is close to saturation. There is no single definite measure for the nonlinearity of a camera. One way of characterising it uses a small input signal, like that from a low intensity light source. The average pixel count is recorded for varying exposure times, as shown in Fig. 3.2. A linear least-squares regression to the signal $S$ yields the residuals $R$ as the deviation of the measurement from the fit and the nonlinearity can be defined as

$$\text{Nonlinearity} = \frac{|\max(R)| + |\min(R)|}{\max(S)}, \tag{3.2}$$

the sum of the largest positive deviation and the largest negative deviation divided by the maximum of the signal. Here, the exposure time has been increased enough to reach a maximum signal of

[2]Princeton Instruments PIXIS 1024BR, back-illuminated, deep depletion CCD.
[3]Semrock LL01-780-25, $> 90\%$ transmission at $780\,\mathrm{nm}$, 3 nm typical FWHM bandwidth.

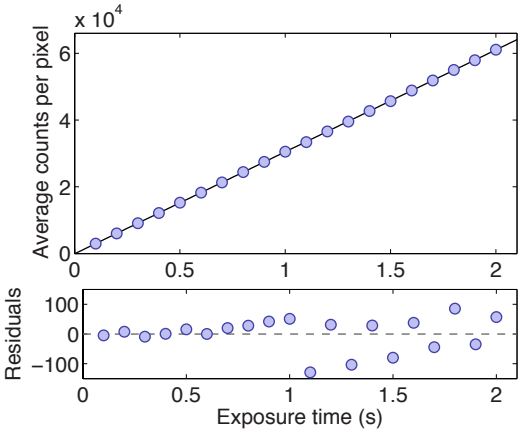


Figure 3.2: Dependence of the average pixel count on the exposure time and deviations from a linear least-squares fit. The sum of the largest positive deviation and the largest negative deviation in relation to the maximum signal give a measure for the nonlinearity of the CCD. (Data provided by Princeton Instruments.)

61080 counts, which is the full well capacity. With $\max(R) = 85$ and $\min(R) = -129$ we get a nonlinearity of $0.35\%$. However, if the average number of counts per pixel is kept below $3 \times 10^4$, if necessary by spreading the signal across many pixels with a higher magnification, the effective nonlinearity reduces to $0.1\%$.

## 3.3 Trap lifetime and temperature

As we have seen in a simple consideration of the noise contribution due to atom loss, the detector performance depends on the trap lifetime. A low pressure of less than $8 \times 10^{-12}$ mbar in the vacuum chamber ensures a low rate of collisions with background gas, which is one of the few measures to increase the thermal lifetime. Other experiments, e. g. with metastable helium [80], have shown that the lifetime is independent of the MOT parameters to within $20\%$. The second loss mechanism is light-assisted collisions, depicted in Fig. 3.3(a), where two Rb atoms, both in the S state, form a loosely bound molecule with large internuclear distance interacting through a van der Waals potential $V(r) = -C_6/r^6$. In the presence of the laser cooling light, one of the atoms is excited into the P state, while the other remains in the S state. The two atoms now interact via an attractive dipole-dipole potential $V(r) = -C_3/r^3$ and start to accelerate towards each other. The S + P state will eventually decay back into the S + S state and the energy gained in this process is released as kinetic energy of the atoms. The average distance between two atoms in a MOT is much larger than the distance at which the molecular potential has its minimum and the atoms only probe the long range limit of the potential. The decay process is random, governed by the lifetime of the excited state, therefore the time spent in the excited state, and thus the amount of energy gained, has an exponential distribution. If the tail of this distribution is large enough, which depends on the detuning of the excitation light, a considerable number of atoms gain enough energy to be expelled from the trap.

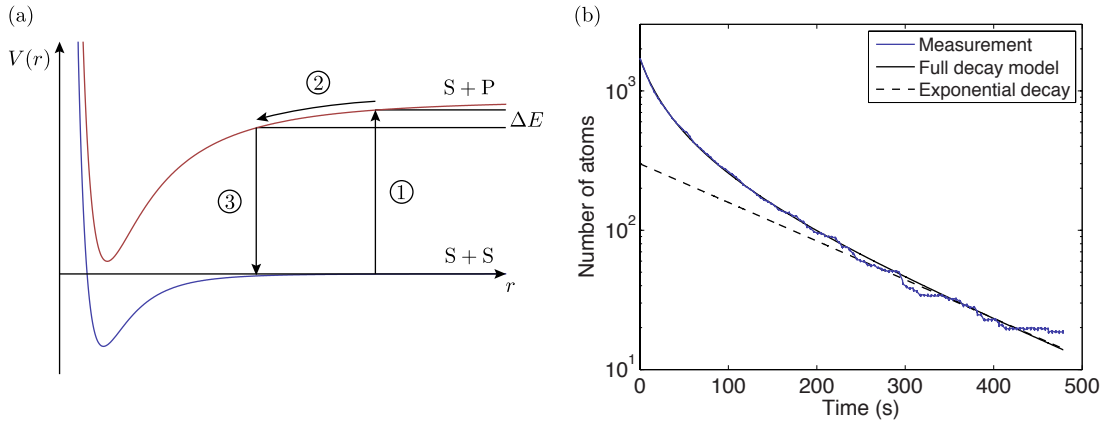


Figure 3.3: Light assisted collisions scheme and measurement. (a) In the presence of light, atoms in the van der Waals potential S + S can be excited into the dipole-dipole potential S + P (1). They will start accelerating towards each other (2) and finally decay back into the ground state (3). Depending on the time spent in the excited state, the acquired energy $\Delta E$ can large enough for the atoms to leave the trap. (b) Measurement of the atom number decaying in time. The full decay model describes both thermal loss and loss due to light-assisted collisions. The purely exponential decay, here fixed to the later half of the measurement, shows clear deviations for larger atom numbers.

Not only loss from the trap can change the atom number, but loading of atoms as well. If loading happens at a rate $L$, the rate equation for the change in atom number $N$ is given by

$$\frac{\mathrm{d}N}{\mathrm{d}t} = L - \frac{N}{\tau} - \beta' \int_V n^2(\boldsymbol{r}, t)\, \mathrm{d}^3\boldsymbol{r}, \tag{3.3}$$

where $\tau$ is the one-body loss rate and the rate of light-assisted collisions is given by the product of the rate $\beta'$ and the volume integral over the squared atom density $n(\boldsymbol{r}, t)$, since it is a two-body effect [50]. In the low density limit the atomic distribution is $n(\boldsymbol{r}, t) = n_0(t)e^{-\boldsymbol{r}^2/\sigma^2}$, where $\sigma$ is the waist of the Gaussian distribution. With a scaled rate $\beta = \beta'(2\pi)^{-3/2}\sigma^{-3}$ we can rewrite the rate equation as

$$\frac{\mathrm{d}N}{\mathrm{d}t} = L - \frac{N}{\tau} - \beta N^2. \tag{3.4}$$

If we neglect the loading and set $L = 0$, Eqn. 3.4 is solved by

$$N(t) = \frac{N_0}{e^{t/\tau}(1 + N_0\beta\tau) - N_0\beta\tau}, \tag{3.5}$$

with $N_0 = N(t = 0)$. If $N_0\beta \ll 1/\tau$, Eqn. 3.5 reduces to $N(t) = N_0 e^{-t/\tau}$. Fig. 3.3 (b) shows a typical decay curve, emphasising the difference between at fit using Eqn. 3.5 and a purely exponential decay. We observe a trap lifetime of $\tau \approx 160\,\mathrm{s}$ and a rate of light-assisted collisions of $\beta \approx 2 \times 10^{-5}\,\mathrm{s}^{-1}$. Hence, light-assisted collisions definitely become significant,

i. e. $N_0\beta\tau \sim 1$, for $N_0 > 300$. In the experiment we observe their influence already for $N \sim 100$. This is in accordance with previous experiments, stating that "under high-vacuum conditions light-assisted collisions dominate the loss from the trap" [81]. In order to constrain this loss, we have to lower the rate of light-assisted collisions, e. g. by increasing the MOT size. We verify experimentally that the MOT size is independent of the atom number (Fig. 3.4(a)). With a Gaussian waist $\sigma = 37.5\,\mu\text{m}$ of the atomic distribution, the two-body loss rate corresponds to $\beta' \approx 2 \times 10^{-11}\,\text{cm}^3\,\text{s}^{-1}$, close to the theoretically predicted value of $1.7 \times 10^{-11}\,\text{cm}^3\,\text{s}^{-1}$ for an intensity of $10\,\text{mW}\,\text{cm}^{-2}$ [82]. However, other experiments have measured significantly lower values around $1 \times 10^{-12}\,\text{cm}^3\,\text{s}^{-1}$ [83]. The least-square regression is not very sensitive to variations of the fit parameters, e. g. decreasing $\beta$ and adjusting $\tau$ yields similar results. We will later introduce an alternative method for extracting the decay rates from their contribution to the signal noise.

Besides the trap lifetime, the other important parameter is the temperature, which should be very low compared to the trap depth (typically on the order of 1 K) in order to reduce the chance of losing an atom during laser cooling. A small temperature usually results in a small MOT size. At the same time, the size of the atomic cloud should be large to reduce the density dependent rate of light-assisted collisions. This can be achieved by choosing a small magnetic field gradient. Here, we measure the temperature by turning off the MOT beams and measuring the size of the atomic cloud for varying times of free expansion. We check that we remain in a regime, where the atom number does not change significantly. A linear fit of the MOT radius versus expansion time yields a thermal velocity of $v_{\text{th}} = \sqrt{2k_{\text{B}}T/m} = 0.12\,\text{m}\,\text{s}^{-1}$ and thus a MOT temperature of $T = 75\,\mu\text{K}$. By increasing the laser detuning to $\delta \sim -3\Gamma$, lowering the laser intensity to $0.68I_{\text{sat}}$ and turning off the magnetic field gradient shortly before releasing the atoms, we cool the atoms in an optical molasses down to $T < 10\,\mu\text{K}$, corresponding to a thermal velocity of $v_{\text{th}} < 4\,\text{cm}\,\text{s}^{-1}$. We will show later how optical molasses can be beneficial for state-selective atom counting. For now, let us note that we can measure the diffusion of the atoms in the light field by imaging the cloud size for varying diffusion times $t$, as shown in Fig. 3.4(b). The area $A = \pi\sigma_x\sigma_y$, where $\sigma_x$ and $\sigma_y$ are the widths of the Gaussian density distributions in the imaging plane, increases with time as $A = 2\pi D_x t$, where $D_x$ is the spatial diffusion coefficient [84]. $D_x$ can be related to the momentum diffusion coefficient $D_p$ introduced in Section 2.2 via $D_p = \alpha^2 D_x$, where $\alpha$ is the damping coefficient. For Doppler cooling the spatial diffusion coefficient is given by [67]

$$D_x = \frac{\Gamma\lambda^2}{4\pi^2}\left(\frac{\delta}{\Gamma}\right)^2 \frac{I_{\text{sat}}}{I}, \tag{3.6}$$

which for our experimental parameters takes the value $D_x = 8 \times 10^{-2}\,\text{cm}^2\,\text{s}^{-1}$. We measure $D_x = 5.2 \times 10^{-3}\,\text{cm}^2\,\text{s}^{-1}$, which is an order of magnitude smaller, likely due to polarisation gradient cooling in the $\sigma^+$–$\sigma^-$ configuration[4].

In principle, it is possible to extract the temperature of an atomic ensemble by observing the fluorescence and determining the intensity correlation function $g^{(2)}(\tau)$, which is related to the Fourier transform of the velocity distribution [85], given by

$$g^{(2)}(\tau) = 1 + \exp\left(-\frac{k_{\text{B}}Tk^2\tau^2}{m}\right). \tag{3.7}$$

[4] The diffusion coefficient in the lin⊥lin configuration can be much larger.

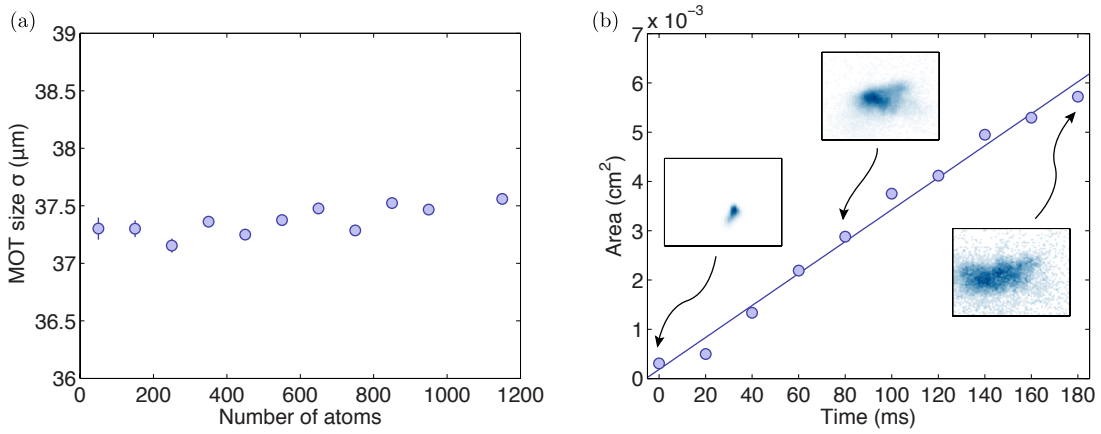


Figure 3.4: Atomic cloud size versus atom number in the MOT and optical molasses release time. (a) The waist of the Gaussian atomic density distribution in the MOT does not depend on the atom number. (b) After the release from the MOT, during molasses cooling, the atoms start to diffuse, as shown in the insets. The area of the density distribution increases linearly with the diffusion time.

The characteristic time $\tau_0$ is given by the inverse Doppler width $k\sqrt{k_\mathrm{B}T/m}$. For an ensemble temperature of about 100 µK, $\tau_0$ is on the order of 1 µs. This timescale is inaccessible with a CCD camera, however, it should be feasible with a fast photo diode.

## 3.4 Signal processing

As mentioned before, we acquire multiple images in a single frame, by employing the frame transfer mode of the CCD. The raw CCD images are divided up into individual stripes, shown in Fig. 3.5, separated in time by the duration of exposure (the shifting time of a few µs can be neglected) and the signal is extracted as the sum over all relevant pixels. We use an elliptical region of interest around the signal, reflecting the shape of the atomic cloud, in order to reduce the read-out noise from pixels with no information. At regular intervals, usually at the start of each dataset, we acquire several background images, where the magnetic field gradient was turned off long enough for all atoms to escape, and average over multiple realisations. In order to correct for random light fluctuations we employ the following background subtraction method (see Fig. 3.6). In addition to the first region of interest around the atoms, yielding the signal $S_1$, we draw a second region of interest of the same size in an empty region of the image and obtain the background signal $B_1$. Now we turn to the background image and sum over the same first region of interest to obtain $S_0$. The background image in the second image of interest results in $B_0$. We have now fixed a background calibration factor $S_0/B_0$, which we can use to scale the atomic signal $S$. If we assume that the light fluctuations affect both $S_1$ and $B_1$ in the same (linear) way, then $B_1 = \text{const.} \cdot B_0$ and $S_1 - S = \text{const.} \cdot S_0$. We can rewrite these conditions to eliminate

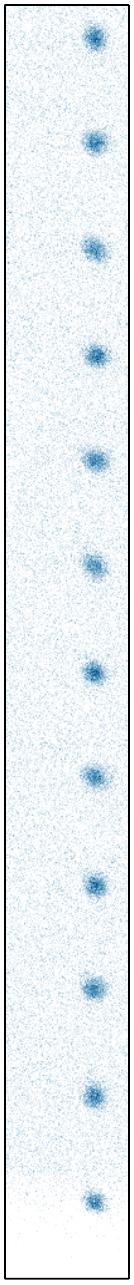

Figure 3.5: Example image of a single atom after applying the frame transfer multiple times before the read-out.

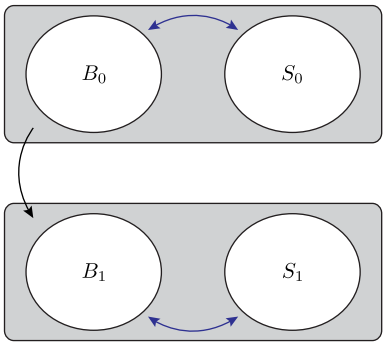


Figure 3.6: Scheme of the background scaling. The fixed ratio $S_0/B_0$ is determined from the background image in the beginning of each sequence and used to scale the background $B_1$ in the signal image. This method reduces homogenous long term drifts on the signal $S_1$.

the constant and obtain

$$S = S_1 - B_1 \frac{S_0}{B_0}. \tag{3.8}$$

In contrast to merely subtracting $S_0$ from $S_1$, this method adds some noise to the signal, because of the additional stray light fluctuations that are captured with $B_0$ and $B_1$, however the long term stability increases due to elimination of common drifts. We measure a background signal level that is smaller than that of three atoms.

## 3.5 Histograms of mesoscopic atom numbers

In order to analyse the detector performance across a wide range of atom numbers, we load the MOT until we reach a large particle number and observe the decay curve as a function of time. We repeat this measurement many times, in order to increase statistics. The uneven coverage of atom numbers, shown in the histogram in Fig. 3.7 (a), reflects the starting conditions of the measurements as well as the random nature of atom loss, where by change some atom number were detected more often than others. Since on average each atom contributes the same amount to the total signal, we observe discrete peaks, where the signal bunches at equidistant levels. We simultaneously fit multiple Gaussian distributions to the histogram peaks to extract the number of counts per atom, and thus measure the number of photons collected from each atom during the exposure time, in this case 100 ms. We obtain a single-atom count rate of $\eta R_{\mathrm{sc}}$ = 90310 counts/atom/s, which does not show any dependence on the atom number to within $0.02\%$ at $N = 250$ ($95\%$ confidence interval). Here we can already observe how the width of the distribution, which is a measure of the noise level, increases with the atom number. At $N = 100$, for example, we obtain a standard deviation of $\sigma = 0.14$ atoms, while at $N = 230$ it is $\sigma = 0.27$. The amount of expected photon shot noise, calculated from the count rate, is $\sigma_{\mathrm{psn}} = 0.11$ at $N = 100$ and $\sigma_{\mathrm{psn}} = 0.16$ at

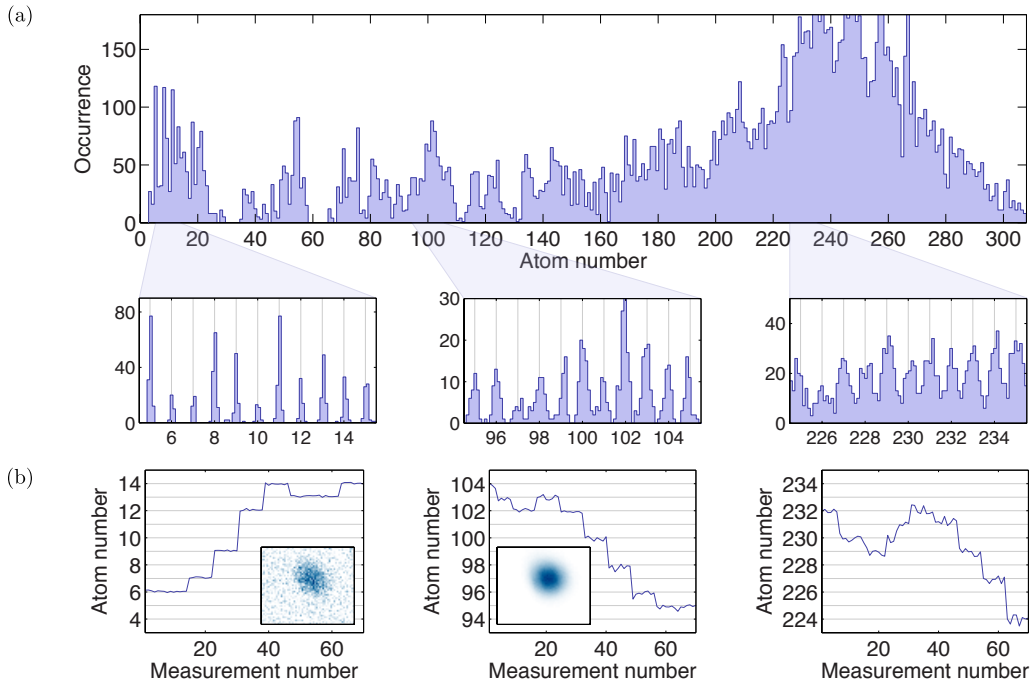


Figure 3.7: Overview of a typical measurement. (a) Frequency of occurrence versus calibrated atom number. A closer look into the histogram shows discrete peaks at the corresponding atom numbers. (b) Example signal traces for 10, 100 and 230 atoms. The insets show the experimental image of a single atom and 100 atoms, respectively.

$N = 230$. The discrepancy must arise from additional fluorescence noise, e. g. long-term drifts or a modulation of the laser amplitude or frequency. Noise contributions from atom loss are not reflected in the width of the distribution, but rather lead to an overall offset in the histogram, since the moment of the decay during the exposure is random.

## 3.6 Variance analysis

In order to understand the limiting noise contributions for atom number detection and find the optimal exposure time, we evaluate the two-sample atom variance

$$\sigma_N^2 = \frac{1}{2}\langle (S_{n+1} - S_n)^2 \rangle, \tag{3.9}$$

where $S_{n+1}$ and $S_n$ are consecutive measurements, each with an integration time $t$. This is analogous to the Allan variance in frequency measurements. At short integration times, we expect the major noise contribution to arise from photon shot noise $\sigma_{\mathrm{psn}}^2$ of the emitted fluorescence and additional fluorescence noise $\sigma_{\mathrm{fn}}^2$, due to frequency or intensity fluctuations of the excitation light. Averaging the signal over longer integration times reduces these contributions to the noise.

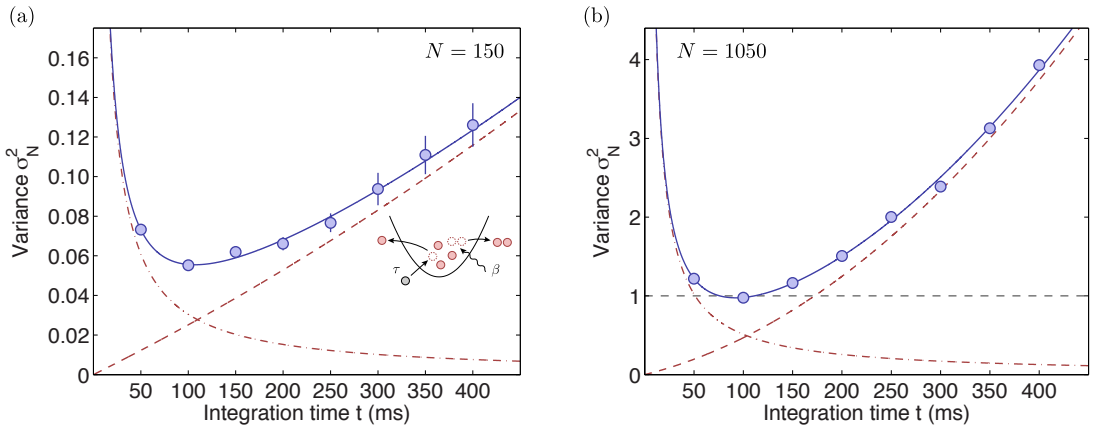


Figure 3.8: Atom variance as a function of the integration time. For short times, photon shot noise and additional fluorescence noise dominate (dash-dotted line), while for longer times, the contribution due to atom loss increases (dashed line). The optimal detection time is almost independent of the atom number, as shown for (a) $N = 150$ and (b) $N = 1050$.

However, for longer integrations times, the probability of atom loss due to one- and two-body decay increases, introducing another noise contribution $\sigma^2_{\text{loss}}$. In general, the variance depends on the integration time $t$, as well as on the atom number $N$ and reads

$$\sigma^2_N(N,t) = \sigma^2_{\text{psn}} + \sigma^2_{\text{fn}} + \sigma^2_{\text{loss}}. \tag{3.10}$$

We have already modelled photon shot noise by $\sigma^2_{\text{psn}} = N(\eta R_{\text{sc}} t)^{-1}$ in the first part of Eqn. 3.1. The additional fluorescence noise can be described by $\sigma^2_{\text{fn}} = (\alpha N)^2 t^{-1}$ with a frequency stability parameter $\alpha$ in units of $\sqrt{\text{s}}$. Each of the $N$ atoms contributes equally to the fluorescence, i. e. the noise contribution is maximally correlated, hence the quadratic scaling in the variance. While the frequency noise is correlated in atom number, it is, of course, random in time and thus scales with $t^{-1}$. Both photon shot noise and additional fluorescence noise average down with increasing integration time, while the probability of atom loss, and thus $\sigma^2_{\text{loss}}$, increases with time. This is shown in Fig. 3.8 from which we extract an optimal exposure time of 100 ms, almost independent of the atom number. The exact expression for $\sigma^2_{\text{loss}}$ can be derived either from a heuristic approach or from a master equation.

### 3.6.1 Heuristic approach

A simple approach to obtain an expression for the noise contribution due to atom loss is to calculate the decay probability as a function of atom number and integration time. Let us first consider only one-body loss, described by the rate equation

$$\frac{\mathrm{d}N}{\mathrm{d}t} = -\frac{N}{\tau}, \tag{3.11}$$

which, for the initial condition $N_0 = N(t=0)$, is solved by $N(t) = N_0 e^{-t/\tau}$. The mean number of lost atoms is $\lambda_1 = N_0 - N(t) = N_0(1 - e^{-t/\tau})$. For integration times much shorter than the

lifetime, $t \ll \tau$, we obtain $\lambda_1 = N_0 t/\tau$. The random loss process is Poisson distributed, such that the probability of $k_1$ loss events during the detection time $t$ is given by $P(k_1|\lambda_1) = e^{-\lambda_1}\lambda_1^{k_1}/k_1!$. Evaluating Eqn. 3.9 with this expression yields

$$\begin{aligned}\sigma_N^2 &= \frac{1}{2}\sum_{k_1=0}^{\infty}\frac{e^{-\lambda_1}\lambda_1^{k_1}}{k_1!}k_1^2 \\ &= \frac{1}{2}(\lambda_1 + \lambda_1^2) \\ &= \frac{1}{2}\left[\frac{N_0 t}{\tau} + \left(\frac{N_0 t}{\tau}\right)^2\right].\end{aligned} \tag{3.12}$$

We now consider two-body loss described by the rate equation

$$\frac{\mathrm{d}N}{\mathrm{d}t} = -\beta N^2. \tag{3.13}$$

For short integration times compared to the rate of light-assisted collisions, $\beta N t \ll 1$, we obtain $N_0 - N(t) = \beta N_0^2 t$. This process is also Poisson distributed and the probability of losing $2k_2$ atoms during the detection time $t$ is $P(k_2|\lambda_2) = e^{-\lambda_2}\lambda_2^{k_2}/k_2!$, with the mean number of two-body loss events $\lambda_2$. Since $\sum_{k_2} 2k_2 P(k_2|\lambda_2) = 2\lambda_2 = \beta N_0^2 t$, we find $\lambda_2 = \beta N_0^2 t/2$ and again evaluate Eqn. 3.9 to obtain

$$\begin{aligned}\sigma_N^2 &= \frac{1}{2}\sum_{k_2=0}^{\infty}\frac{e^{-\lambda_2}\lambda_2^{k_2}}{k_2!}(2k_2)^2 \\ &= 2(\lambda_2 + \lambda_2^2) \\ &= \beta N_0^2 t + \frac{1}{2}\beta^2 N_0^4 t^2.\end{aligned} \tag{3.14}$$

In the experiment, both one- and two-body loss processes can occur simultaneously and in higher orders, e. g. one light-assisted collision and two collisions with background gas during the exposure, hence cross terms of $\lambda_1$ and $\lambda_2$ have to be considered. In general

$$\sigma_N^2 = \frac{1}{2}\sum_{k=0}^{\infty} P(k)k^2, \tag{3.15}$$

with a probability $P(k)$ of losing $k$ atoms during the exposure, including both loss mechanism. This sum includes the term in Eqs. 3.12 and 3.14, as well as the cross terms

$$\sigma_N^2 = \frac{1}{2}e^{-\lambda_1-\lambda_2}\sum_{k=0}^{\infty} c_k k^2, \tag{3.16}$$

with the first non-zero coefficient $c_3 = \lambda_1\lambda_2$. Up to this order, with the approximation that $\lambda_1 + \lambda_2 \ll 1$, the entire loss contribution to the variance reads

$$\sigma_{\text{loss}}^2 = \left(\frac{N}{2\tau} + \beta N^2\right)t + \frac{1}{2}\left(\frac{N^2}{\tau^2} + \frac{9\beta N^3}{2\tau} + \beta^2 N^4\right)t^2. \tag{3.17}$$

### 3.6.2 Master equation approach

In an alternative approach, we will derive the total atom variance from a master equation and relate it to the two-sample variance given in Eqn. 3.9. We consider the probability $P(N,t)$ of having $N$ atoms in the trap at a given time $t$. The time evolution of this probability is given by the master equation

$$\frac{\partial}{\partial t}P(N,t) = \sum_{N'} W(N',N)P(N',t) - W(N,N')P(N,t). \tag{3.18}$$

The first term describes an increase of the probability $P(N,t)$ when the atom number changes from any $N'$ to $N$ with a weight $W(N',N)$. The second term accounts for a change in atom number from $N$ to any $N'$, weighted with $W(N,N')$, which reduces the probability. The two processes that change the atom number are one-body decay due to collisions with the background gas, which happens at a rate $K_1$, and light-assisted collisions, occurring with a rate $K_2$. Three-body losses can be neglected in this case, while loading events do not contribute significantly to the noise. The master equation for one- and two-body decay reads

$$\begin{aligned}\frac{\partial}{\partial t}P(N,t) = {} & K_1[(N+1)P(N+1,t) - NP(N,t)] \\ & + \frac{K_2}{2}[(N+2)(N+1)P(N+2,t) - N(N-1)P(N,t)],\end{aligned} \tag{3.19}$$

where $K_2$ has to be halved, since by definition it accounts for the loss of only one atom, while in the actual process two atoms are lost from the trap.[5]

We are primarily interested in the time evolution of the mean atom number and the atom variance, thus we calculate the moments of the probability distribution and consider only the first and second. The time evolution of the $k$-th moment is given by

$$\begin{aligned}\frac{\partial}{\partial t}\langle N^k\rangle &= \frac{\partial}{\partial t}\sum_N N^k P(N,t) \\ &= \sum_N N^k \frac{\partial}{\partial t}P(N,t) \\ &= \sum_N P(N,t)[K_1((N-1)^k N - N^{k+1}) \\ &\quad + \frac{K_2}{2}((N-2)^k(N-1)N - N^{k+1}(N-1))].\end{aligned} \tag{3.20}$$

[5] The probability of a two-body decay scales with $N(N-1)$, according to the urn model, where $k$ balls are drawn randomly without replacement, but considering the order, in which case the number of elements in the sample space is $|\Omega| = N\cdot(N-1)\cdot(N-2)\cdot\dots = N!/(N-k)!$.

First we consider the mean of the atom number ($k = 1$)

$$\begin{aligned}\frac{\partial}{\partial t}\langle N\rangle &= \sum_N P(N,t)[K_1((N-1)N-N^2)\\ &\quad + \frac{K_2}{2}((N-2)(N-1)N-N^2(N-1))]\\ &= \sum_N P(N,t)[-K_1N+K_2(-N^2+N)]\\ &= -K_1\langle N\rangle - K_2\langle N^2\rangle + K_2\langle N\rangle . \end{aligned} \tag{3.21}$$

In order to obtain the variance, we need to consider the second moment ($k = 2$)

$$\begin{aligned}\frac{\partial}{\partial t}\langle N^2\rangle &= \sum_N P(N,t)[K_1((N-1)^2N-N^3)\\ &\quad + \frac{K_2}{2}((N-2)^2(N-1)N-N^3(N-1))]\\ &= \sum_N P(N,t)[K_1N-2K_1N^2-2K_2N^3+4K_2N^2-2K_2N]\\ &= K_1\langle N\rangle - 2K_1\langle N^2\rangle - 2K_2\langle N^3\rangle + 4K_2\langle N^2\rangle - 2K_2\langle N\rangle . \end{aligned} \tag{3.22}$$

The atom variance $\mathrm{Var}(N) = \langle N^2\rangle - \langle N\rangle^2$ evolves in time as

$$\begin{aligned}\frac{\partial}{\partial t}\mathrm{Var}(N) &= \frac{\partial}{\partial t}\left(\langle N^2\rangle - \langle N\rangle^2\right) = \frac{\partial}{\partial t}\langle N^2\rangle - 2\langle N\rangle\frac{\partial}{\partial t}\langle N\rangle\\ &= K_1\langle N\rangle - 2K_1\langle N^2\rangle - 2K_2\langle N^3\rangle + 4K_2\langle N^2\rangle - 2K_2\langle N\rangle\\ &\quad + 2K_1\langle N\rangle^2 + 2K_2\langle N^2\rangle\langle N\rangle - 2K_2\langle N\rangle^2 . \end{aligned} \tag{3.23}$$

We can see that the differential equation for the $k$-th moment depends on moments of higher order $k+1$. In order to obtain a set of closed differential equations, one can make a *Gaussian ansatz*.

If a Gaussian probability distribution is assumed initially, numerical calculations for later times show that the probability distribution remains Gaussian. One can therefore assume that the probability distribution is Gaussian at all times, thus the higher moments are known and can be expressed in terms of mean value $\mu$ and variance $\sigma^2$. For a Gaussian probability distribution the second and third moment are

$$\langle N^2\rangle = \mu^2 + \sigma^2, \tag{3.24}$$

$$\langle N^3\rangle = \mu^3 + 3\mu\sigma^2. \tag{3.25}$$

This leads to the closed set of coupled differential equations

$$\frac{\partial}{\partial t}\langle N\rangle = -K_1\mu - K_2(\mu^2-\sigma^2-\mu) \tag{3.26}$$

and

$$\frac{\partial}{\partial t}\mathrm{Var}(N) = K_1(\mu-2\sigma^2) + K_2(4\sigma^2-4\mu\sigma^2+2\mu^2-2\mu), \tag{3.27}$$

which, in its entire form, can only be solved numerically. It is also interesting to consider the time evolution of the second moment

$$\frac{\partial}{\partial t}\left\langle N^2\right\rangle = K_1(\mu - 2\sigma^2 - 2\mu^2) + K_2(4\sigma^2 - 6\mu\sigma^2 + 4\mu^2 - 2\mu - 2\mu^3). \tag{3.28}$$

In the experiment the atom number ranges between 1 and $10^3$ and we investigate single-particle resolution, hence the atom variance is required to be smaller than unity. With this assumption, $\sigma^2 \ll \mu$, Eqs. 3.26, 3.27 and 3.28 reduce to

$$\frac{\partial}{\partial t}\left\langle N\right\rangle = -K_1\mu - K_2(\mu^2 - \mu), \tag{3.29}$$

$$\frac{\partial}{\partial t}\mathrm{Var}(N) = K_1\mu + K_2(2\mu^2 - 2\mu) \tag{3.30}$$

and

$$\frac{\partial}{\partial t}\left\langle N^2\right\rangle = K_1(\mu - 2\mu^2) + K_2(4\mu^2 - 2\mu - 2\mu^3), \tag{3.31}$$

which are now decoupled. Moreover, one can find a solution to Eqn. 3.29 and use it to solve Eqs. 3.30 and 3.31.

We can express the noise contribution from loss in terms of one-body lifetime $\tau = 1/K_1$ and the rate of light-assisted collisions $\beta = K_2$. Interpreting the mean of the Gaussian probability distribution $\mu$ as the mean atom number $\langle N\rangle$, we obtain

$$\frac{\partial}{\partial t}\left\langle N\right\rangle = -\frac{\langle N\rangle}{\tau} - \beta'\left(\left\langle N\right\rangle^2 - \left\langle N\right\rangle\right) \tag{3.32}$$

and

$$\frac{\partial}{\partial t}\mathrm{Var}(N) = \frac{\langle N\rangle}{\tau} + 2\beta'\left(\left\langle N\right\rangle^2 - \left\langle N\right\rangle\right), \tag{3.33}$$

as well as

$$\begin{aligned}\frac{\partial}{\partial t}\left\langle N^2\right\rangle &= \frac{\langle N\rangle - 2\left\langle N\right\rangle^2}{\tau} + 2\beta'\left(2\left\langle N\right\rangle^2 - \left\langle N\right\rangle - \left\langle N\right\rangle^3\right)\\ &= \frac{\partial}{\partial t}\mathrm{Var}(N) - 2\left(\frac{\left\langle N\right\rangle^2}{\tau} + \beta'\left(\left\langle N\right\rangle^3 - \left\langle N\right\rangle^2\right)\right).\end{aligned} \tag{3.34}$$

If we assume $\langle N\rangle \ll \left\langle N\right\rangle^2$ in Eqn. 3.32, which is a good approximation for large atom numbers, the mean atom decay, with the initial atom number $N_0$, is given by

$$\begin{aligned}\langle N(t)\rangle &= \frac{N_0}{\mathrm{e}^{t/\tau}(1 + N_0\beta\tau) - N_0\beta\tau}\\ &= N_0 - \left(\frac{N_0}{\tau} + \beta N_0^2\right)t + \mathcal{O}(t^2),\end{aligned} \tag{3.35}$$

where higher orders in $t$ can be neglected, if $t \ll \tau$. In order to analyse the variance for multiple realisations of the experiment, we select decay curves that begin at a fixed $N_0$, such that $\mathrm{Var}(N)|_{t=0} = 0$. Hence, initially, $\left\langle N^2\right\rangle = \left\langle N\right\rangle^2 = N_0^2$.

The total two-sample variance is given by

$$\begin{aligned}\frac{1}{2}\mathrm{Var}(S_{n+1}-S_n) &= \frac{1}{2}\langle (S_{n+1}-S_n)^2\rangle - \frac{1}{2}\langle S_{n+1}-S_n\rangle^2 \\ &= \sigma_N^2 - \frac{1}{2}\langle S_{n+1}-S_n\rangle^2,\end{aligned} \tag{3.36}$$

where the first term is the definition of the two-sample variance from Eqn. 3.9 and the second term represents the mean atom loss. From this we see the role of the Allan variance as a *two-sample second moment*.

In order to deduce the noise contribution from loss in the total two-sample variance for a detection time $t \ll \tau$, we use

$$\frac{1}{2}\mathrm{Var}(S_{n+1}-S_n) = \frac{1}{2}\mathrm{Var}(N(t)-N(0)) = \frac{1}{2}\mathrm{Var}(N(t)) \tag{3.37}$$

and solve Eqn. 3.33 with the condition that $\mathrm{Var}(N)|_{t=0} = 0$. In the limit of large atom numbers and short detection times we obtain

$$\frac{1}{2}\mathrm{Var}(S_{n+1}-S_n) = \frac{N}{2\tau}t + \beta N^2 t, \tag{3.38}$$

which has the character of an *atom shot noise*, proportional to $\sqrt{t}$ in the standard deviation and intrinsic to the random nature of the loss processes, both obeying Poisson statistics. The contribution from mean atom loss is obtained using Eqn. 3.35 as

$$\frac{1}{2}\langle S_{n+1}-S_n\rangle^2 = \frac{1}{2}\left(\frac{N_0}{\tau}+\beta N_0^2\right)^2 t^2. \tag{3.39}$$

In total the contributions to the two-sample variance are

$$\sigma^2_{\text{loss}} = \left(\frac{N}{2\tau}+\beta N^2\right)t + \frac{1}{2}\left(\frac{N}{\tau}+\beta N^2\right)^2 t^2. \tag{3.40}$$

A Monte-Carlo simulation of the loss process is shown in Fig. 3.9 to illustrate the difference to the result from the heuristic approach (Eqn. 3.17). Here, the loss parameters $\tau = 200\,\mathrm{s}$ and $\beta = 5\times10^{-7}\,\mathrm{s}^{-1}$ and a detection time of 100 ms were chosen. The two approaches agree for small atom numbers, where the cross-terms are not relevant. At larger atom numbers and for higher rates for light-assisted collisions the deviation becomes apparent.

The deterministic mean atom loss[6] can be accounted for, thus the noise level is reduced to the fundamental atom shot noise given in Eqn. 3.38. In the experiment, given a raw measurement $N$ of the atom number, the mean atom loss correction is done by calculating $N' = N + Nt/\tau + \beta N^2 t$ as the loss-compensated result. Conceptually, the contribution from mean atom loss is the difference between considering the total variance and the Allan variance, which is the second moment, as shown in Fig. 3.10. Generally, the optimal detection time is different for either case, however, here the difference is not significant. The atom variance $\sigma_N^2$ is shown in Fig. 3.11 for an integration time of 100 ms both with and without correction of the mean loss. In the first case, the single-atom

[6] Mean atom loss is a continuous effect, as opposed to the discrete nature of the loss events leading to atom shot noise.

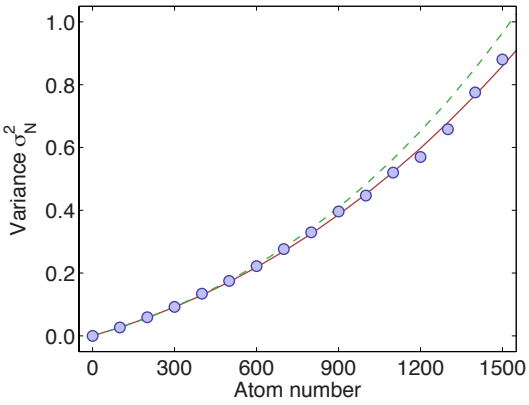


Figure 3.9: Monto-Carlo simulation of the noise contribution due to atom loss (blue circles). The master equation description (solid line) follows the data, while the heuristic result (dashed line) deviates at large atom numbers. For higher rates of light-assisted collisions the deviation becomes stronger.

resolution limit $\sigma_N^2 = 1$ is reached at $N = 1080$, while in the second case the limit is $N = 1200$. We perform a simultaneous fit of the noise model, given in Eqn. 3.10, to all atom numbers and all integration times with free parameters $\alpha$, $\tau$ and $\beta$. From this we can quantify the different noise contributions as a function of the atom number. Photon shot noise, which we have fixed given the number of detected photons per atom, increases linearly with $N$ and contributes only $\sim 10\%$ at the single-atom resolution threshold. The fluorescence noise is quantified by $\alpha = 1.9(1) \times 10^{-4}\,\mathrm{s}^{1/2}$, which would correspond to a frequency noise of the laser cooling light on the order of 10 kHz averaged over the detection time, and increases quadratically with the atom number, making up about half the total variance at $N = 1200$. The loss parameters $\tau = 246(44)$ s and $\beta = 3(3) \times 10^{-7}\,\mathrm{s}^{-1}$ enter into the atom shot noise, which is the second largest noise contribution at high atom numbers.

## 3.7 Fidelity of atom number detection

We use the noise model and its parameters to calculate the detection fidelity $F$ for different atom numbers. Variance and fidelity (or equivalently the error probability) give complementary information. The variance quantifies how far away the measurement is from reality, which is especially important for variances larger than unity, while the fidelity, given single-atom resolution, states the level of confidence in the result. Given a certain atom number $N_0$ at the beginning of the detection, we define the fidelity $F$ as the probability that the measurement corresponds exactly to $N_0$. While photon shot noise and additional fluorescence noise lead to a Gaussian distribution of the measurements, atom loss does not. The latter follows the Poisson distribution and is highly biased in the sense that loading events are negligible and the atom number can only decrease. In order to take this non-Gaussian effect into account, we cannot simply rely on the atom variance, but rather we have to estimate the fidelity using the obtained parameters $\alpha$, $\tau$ and $\beta$ and perform a

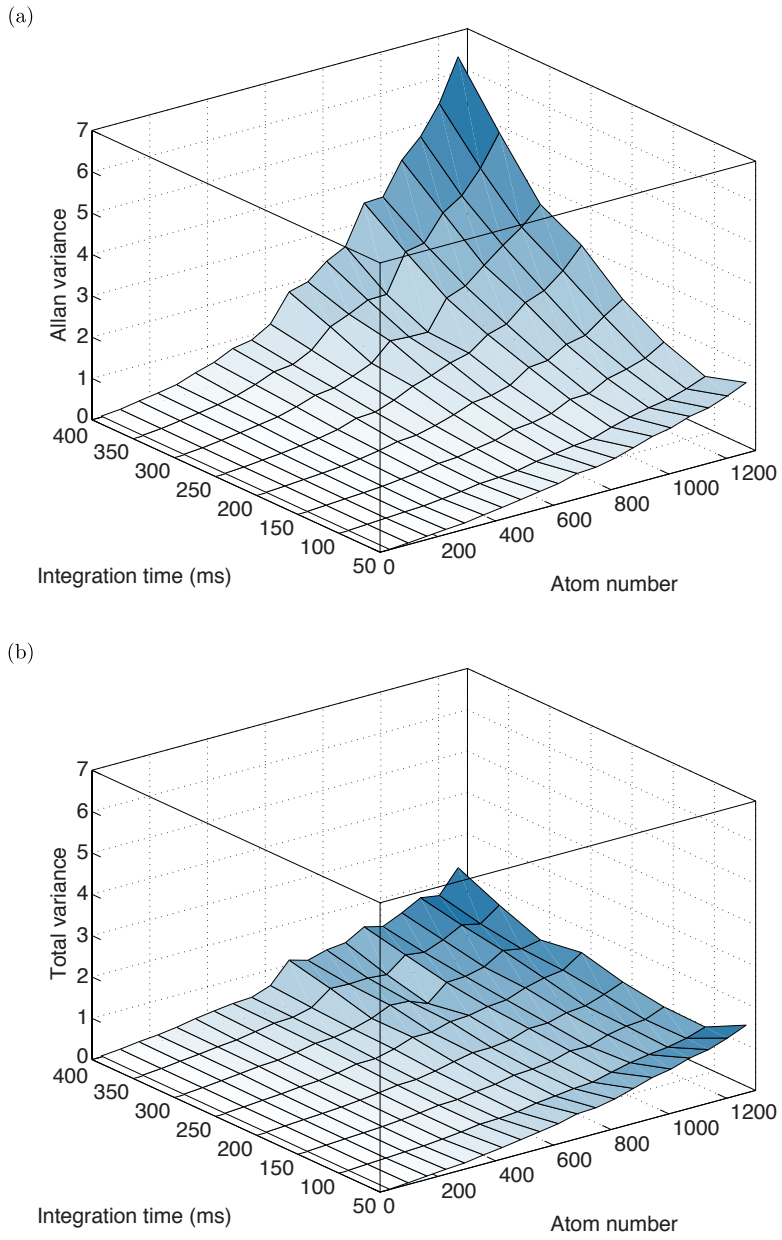


Figure 3.10: Measurement of the atom variance including (a) and excluding (b) the contribution from mean atom loss.

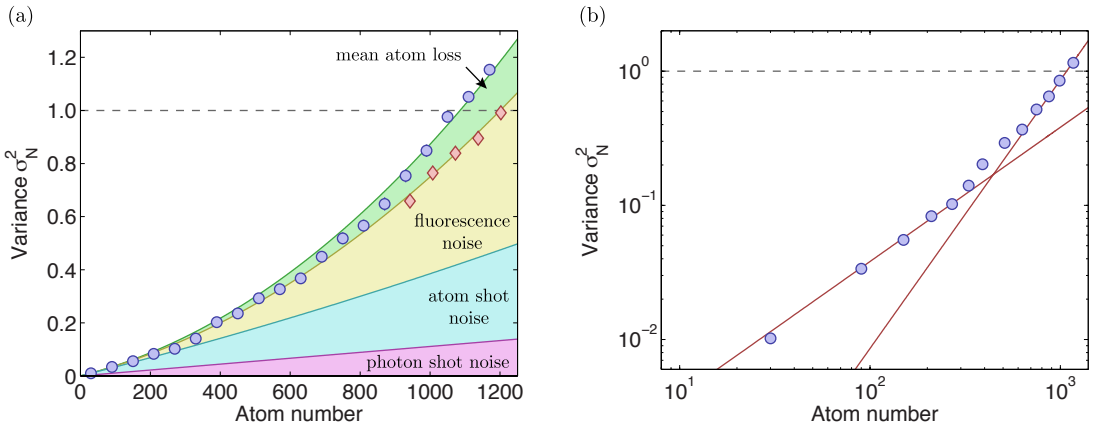


Figure 3.11: Atom variance as a function of the atom number, measured with an integration time of 100 ms. (a) The individual noise contributions are shown as a function of the atom number and discussed in the main text. The single-atom resolution limit $\sigma_N^2 = 1$ is reached at $N = 1080$ (blue circles). This can be improved by correcting the raw measurement for mean atom loss (red diamonds), reaching a maximum atom number of $N = 1200$. (b) A linear increase of $\sigma_N^2$ for small atom numbers transitions into a quadratic increase for large atom numbers.

Monte-Carlo simulation of the detection, given an initial atom number $N_0$. At each iteration step $k$ the simulation determines the atom number $N_k$ and the corresponding CCD counts after a time interval $\delta t$ much shorter than the integration time of $t = 100$ ms. Atom number decay is simulated by drawing from a convolution of Poisson distributions that quantify one- and two-body losses. The probability of losing a single atom due to a collision with background gas is $P_1 = N_k \delta t$, while loss due to light-assisted collisions occurs with a probability of $P_2 = \beta N_k^2 \delta t/2$. From the number of atoms $N_k$ we obtain the number of CCD counts $c_k$ in each time step by randomly drawing from a Gaussian distribution with mean $\langle c_k \rangle = N_k \eta R_{\mathrm{sc}} \delta t$ and variance $\sigma_c^2 = (\sigma_{\mathrm{psn}}^2 + \sigma_{\mathrm{fn}}^2)\eta^2 R_{\mathrm{sc}}^2$. The total number of counts $C = \sum_k c_k$ yields the measured atom number $N = C/t$, which is corrected for the mean atom loss to obtain $N' = N(1 + t/\tau + \beta N t)$ and rounded to the nearest integer. This result is compared to the initial atom number $N_0$. For atom numbers up to $N_0 = 200$ the error probability $1 - F$ is dominated by one-body loss with the probability $P_{\mathrm{loss}} \simeq N_0 t/2\tau$. Note that only a loss event occurring during the first half of the exposure will lead to a measurement error, hence the factor of 2 in $P_{\mathrm{loss}}$. Beyond $N_0 = 200$ the dominant noise source is fluorescence noise, which is described by a Gaussian distribution

$$f(N) = \frac{1}{\sqrt{2\pi}\sigma_{\mathrm{f}}} e^{-(N-N_0)^2/2\sigma_{\mathrm{f}}^2}, \tag{3.41}$$

where $\sigma_{\mathrm{f}}^2 = \sigma_{\mathrm{psn}}^2 + \sigma_{\mathrm{fn}}^2$. The probability of a measurement lying outside the interval $[N_0 - \frac{1}{2}, N_0 + \frac{1}{2}]$ is

$$P_{\mathrm{f}} = 1 - \mathrm{erf}\left(\frac{1}{\sqrt{8}\sigma_{\mathrm{f}}}\right). \tag{3.42}$$

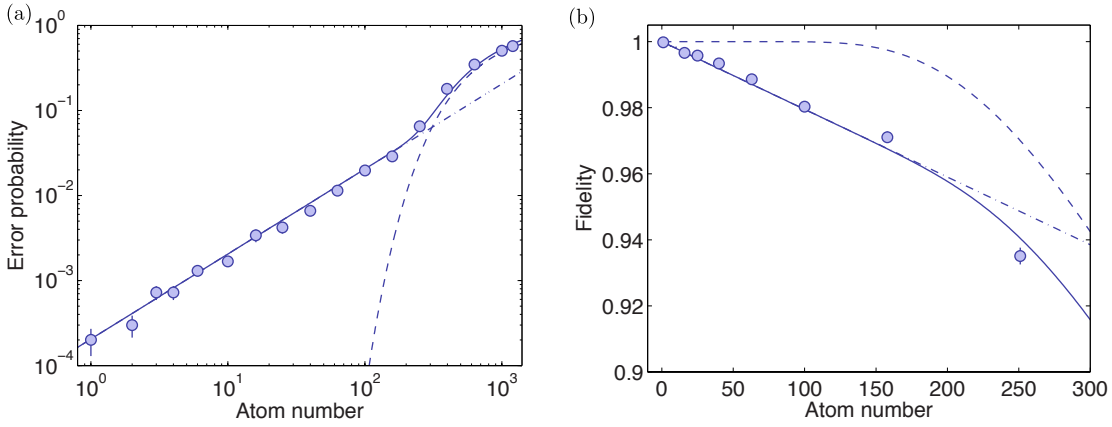


Figure 3.12: Error probability for exact atom number detection. (a) The error probability $1 - F$ is dominated by the probability of one-body decay (dash-dotted line) for small atom numbers. Above $10^2$ atoms the probability of making an error due to fluorescence noise (dashed line) becomes the dominant term. Both these contributions together (solid line) excellently describe the simulated detection (blue circles). (b) The fidelity $F$ remains greater than $98\%$ for atom numbers up to 100, where fluorescence noise is negligible.

Both $P_{\mathrm{loss}}$ and $P_{\mathrm{f}}$ are plotted in Fig. 3.12 and show excellent agreement with the simulated data in the appropriate regimes.

# 4 State-selective atom counting

After having shown single-atom resolution for the total atom number in a mesoscopic sample with up to 1200 particles, we now turn to the task of measuring the atom number of each individual state of a two-component gas. These states will be $|F = 1\rangle$ and $|F = 2\rangle$ of the hyperfine manifold of the $^{87}$Rb ground state $^2\mathrm{S}_{1/2}$, shown in Fig. 4.1 (a), and the atom numbers $N_1$ and $N_2$, respectively. First, we will present a sequential method, in which all atoms are released from the trap, the atoms in state $|F = 2\rangle$ are expelled from the trap using a resonant laser beam and, subsequently, the atoms in $|F = 1\rangle$ are re-trapped for fluorescence imaging. By determining the total atom number $N = N_1 + N_2$ before a Ramsey sequence and measuring $N_1$ after the sequence, we can deduce the number of atoms $N_2$ that were expelled from the trap.

We will then show a more refined method in which the individual atom numbers are detected simultaneously in a novel hybrid trap. A blue-detuned focused light-sheet is superimposed on the MOT to create a potential barrier between the two sites of the resulting double-well system. Consider a spinor BEC with states $|1\rangle = |F = 2, m_F = -1\rangle$ and $|2\rangle = |F = 1, m_F = 1\rangle$. These two states can be used for quantum enhanced metrology in an SU(2) interferometer. At the end of the Ramsey sequence, the difference between the atom number $N_1$ in state $|1\rangle$ and the atom number $N_2$ in state $|2\rangle$ has to be determined. The two states can be spatially separated with a Stern-Gerlach pulse and individually recaptured in the two sites of the split MOT. For this step optical molasses cooling of the atoms can be beneficial, since the dense atomic cloud can be slowly expanded, instead of loading it directly into the hybrid optical trap and risking fast atom loss due to light-assisted collisions. Once the atoms are loaded into the split MOT, we again perform fluorescence imaging, however, now we have to take into account particle exchange between the sites and thus extend our noise model.

During laser cooling the atom spends a considerable time in the excited state, for which the blue-detuned light-sheet is not repulsive, but attractive. In order to avoid this situation, the light-sheet beam and the MOT beams are pulsed alternately on a timescale which is faster than the particle movement but slower than the lifetime of the excited state. Averaging over many pulsing cycles during the exposure time inevitably leads to a reduced number of emitted photons per atom, thus increasing the photon shot noise.

## 4.1 Sequential detection using resonant laser pulses

As a first step, we measure the efficiency of releasing the atoms from the MOT and recapturing them without the application of a push pulse. We turn off the trap light for several release times $t$ up to $4\,\mathrm{ms}$ and measure a recapture efficiency of above $99.92(1)\%$ for release times up to $2\,\mathrm{ms}$. The error probability scales with $t^3$, which is consistent with isotropic thermal expansion. The magnetic field gradient is kept on during the release time, since we do not expect it to significantly

influence the motion of the atoms. We then check the efficiency of pushing the $|F = 2\rangle$ atoms out of the recapture volume by applying a laser beam resonant with the $|F = 2\rangle \longleftrightarrow |^2\mathrm{P}_{3/2}, F' = 3\rangle$ transition while the MOT beams are turned off. The pushing beam has a waist of 3 mm and an intensity of $4.4\,\mathrm{mW/cm^2}$. The pulse is applied during two CCD exposures on the same image, making use of the frame-transfer mode (see Fig. 4.1 (b)). Upon excitation the atoms in $|F = 2\rangle$ receive multiple photon recoil momenta and we check that a pulse time of more than $100\,\mu\mathrm{s}$ is enough for them to leave the recapture volume. Ideally, the $|F = 1\rangle$ atoms are not affected by this process, however, there is a small probability for off-resonant excitation at a detuning of $6.8\,\mathrm{GHz}$ between the $|F = 2\rangle$ and $|F = 1\rangle$ states. In order to reduce this effect to a minimum, the resonant laser pulse time is not increased beyond $100\,\mu\mathrm{s}$. We observe a change of the push efficiency of about $1.5\%$ when changing the polarisation of the laser beam between $\sigma$- and $\pi$-polarisation.

In the steady state of magneto-optical trapping almost all atoms are cycling between the states $|^2\mathrm{S}_{1/2}, F = 2\rangle$ and $|^2\mathrm{P}_{3/2}, F' = 3\rangle$, while the population of $|F = 1\rangle$ is very small. In order to choose a different population of the states as a starting condition for state-selective atom counting, we perform optical pumping with a preparation beam resonant to the $|F = 2\rangle \longleftrightarrow |F' = 1\rangle$ transition. This beam has a waist of 4.7 mm and an intensity of $18.5\,\mathrm{mW/cm^2}$. The sequence for obtaining the overall detection efficiency starts by turning off the MOT beams. We then optically pump all the atoms into the $|F = 1\rangle$ state and subsequently apply the push pulse. Ideally there would be no atoms in the $|F = 2\rangle$ state and off-resonant excitation of the $|F = 1\rangle$ atoms is kept at a minimum. Finally, we turn on the trapping beams, recapturing the atoms, and perform fluorescence imaging, comparing the final atom number to the initial one. Here the error probability scales with $t^3 + t$. In addition to the thermal expansion, there is a force along the $k$-vector of the laser beam resulting from off-resonant optical pumping, which leads to the linear increase with $t$. We chose an optimal release time of 2.2 ms, where the error probability for efficient pushing is equal to the one for the entire sequence, including optical pumping. There, as shown in Fig. 4.1 (c), we obtain an average detection fidelity of $99.6(1)\%$, allowing us to state-selectively detect the atom number in a sample with 250 atoms.

To understand the process of expelling the $|F = 2\rangle$ atoms with radiation pressure, we consider both an analytical model as well as Monte-Carlo simulations.

### 4.1.1 Analytical model

The dependence of the push efficiency on the release time can be understood by first considering the individual steps of the process. First the MOT beams are turned off, such that the atoms, with their initial thermal distribution ($T \sim 80\,\mu\mathrm{K}$), start spreading out. Immediately after the trapping beams have been turned off, a laser pulse resonant with the $|F = 2\rangle \longleftrightarrow |F' = 3\rangle$ transition is applied to impart momentum on the atoms and push them out of the capture range, which is given by the MOT beam size $r_0 = 1\,\mathrm{mm}$. After a release time $t$, the trapping light is turned on and the number of recaptured atoms is measured.

The initial thermal distribution has a width of $\sigma = \sqrt{k_\mathrm{B}T/m} = 0.0875\,\mathrm{m/s}$, which is much smaller than the critical velocity $v_\mathrm{c} = r_0/t \sim 1\,\mathrm{m/s}$, therefore the thermal distribution can be neglected for this process. Instead, the velocity distribution $f(v)$ after a release time $t$ is given by the number of scattered photons during the push pulse times the recoil velocity $v_\mathrm{rec} = h/m\lambda = 5.9\,\mathrm{mm/s}$. When the MOT is released it is assumed that all atoms are in $|F = 2\rangle$, equally distributed

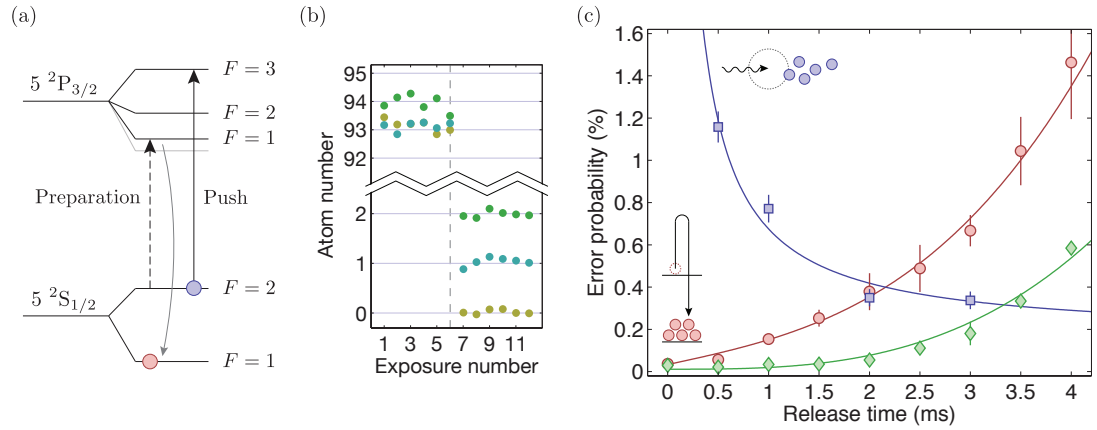


Figure 4.1: Efficiency of state-selective detection via radiation pressure. (a) Level scheme of the $D_2$ transition in $^{87}$Rb. During the release time, atoms in $|F = 2\rangle$ are pushed out of the recapture volume by a laser beam resonant with respect to the $|F' = 3\rangle$ state. An arbitrary population imbalance can be prepared by optical pumping via the $|F' = 1\rangle$ state. (b) Example measurement of the pushing efficiency, comparing initial and final atom number. The push pulse is applied between exposure 6 and 7, denoted by the dashed line. (c) The measured recapture efficiency without additional pulses (green diamonds) is consistent with thermal isotropic expansion (green line). The error probability for expelling $|F = 2\rangle$ atoms (blue squares) is described by an analysis of the depumping rate from $|F = 2\rangle$ to $|F = 1\rangle$, taking into account imperfect polarisation of the pushing beam (blue line). The overall error probability for preparing atoms in $|F = 1\rangle$ (red circles) includes contributions from thermal expansion, as well as off-resonant optical pumping (red line).

among the $m_F$ sub-levels. It is beneficial to use circular polarised light in order to eventually reach the cycling transition $|F = 2, m_F = 2\rangle \longleftrightarrow |F = 3, m_F = 3\rangle$. The probability to excite an atom into the $|F' = 2\rangle$ state, instead of the $|F' = 3\rangle$ state, is given by $\Omega_0^2/2\Omega_{\text{eff}}^2$, where $\Omega_0 = \Gamma\sqrt{s_0/2}$ is the Rabi frequency with $s_0 = 2.6$, corresponding to an intensity of $I = 4.4\,\text{mW}\,\text{cm}^{-2}$, and $\Omega_{\text{eff}} = \sqrt{\Omega_0^2 + \Delta^2}$ is the effective Rabi frequency with a detuning of $\Delta = 43.95\,\Gamma$. The factor of 2 comes from time averaging of the Rabi flopping over the pulse time. By summing over the corresponding Clebsch-Gordan coefficients, quantifying the strength of the transitions from each ground state sub-level to each excited state sub-level, one obtains a branching ratio of 1:1 for the transitions $|F' = 2\rangle \to |F = 1\rangle$ and $|F' = 2\rangle \to |F = 2\rangle$. Thus the probability of a subsequent decay to $|F = 1\rangle$, where the atom becomes dark for the push pulse, is $1/2$ and the total decay rate is given by

$$R_{\text{D}} = \varepsilon \frac{1}{2} \frac{\Omega_0^2}{2\Omega_{\text{eff}}^2} R_{\text{sc}} = \varepsilon \frac{\Omega_0^2}{4\Omega_{\text{eff}}^2} \frac{\Gamma}{2}, \tag{4.1}$$

where $\varepsilon < 1$ accounts for the fact that the decay rate is reduced, once the cycling transition is reached. If the atom reaches the $|F = 1\rangle$ state after the first excitation, the velocity of the atom

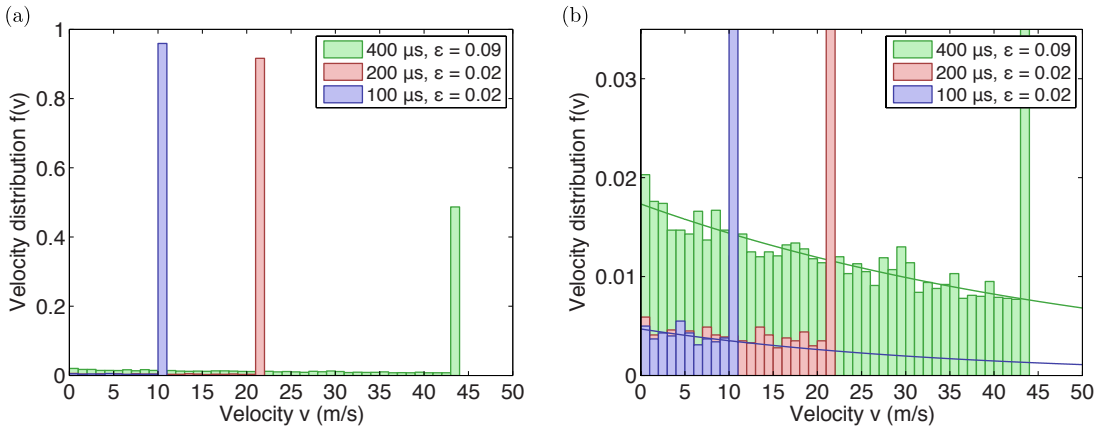


Figure 4.2: Velocity distribution after pushing obtained from the simulation number of scattered photons. (a) Most of the atoms will scatter the maximum amount of photons given the pulse length (shown here for 100 µs, 200 µs and 400 µs), resulting in a peak of the velocity distribution $f(v)$ at the highest possible velocity. Below that there is a plateau of almost equaly distributed velocities. (b) A closer look at small values of $f(v)$ reveals the exponential decay of the plateau (solid lines), which we can assume to be essentially flat for small velocities. The contribution at these small velocities depends on $\varepsilon$.

increases only by $v_{\mathrm{rec}}$ along the direction of the push beam. We then have $f(0)v_{\mathrm{rec}} = R_{\mathrm{D}}/R_{\mathrm{sc}}$. The probability for larger numbers of scattering processes, i. e. higher velocity gain, drops exponentially, as one would expect for a Poisson process (many repetitions of an event with small probability). The maximum number of scattered photons $n_{\mathrm{max}} = \tau_{\mathrm{pulse}}\Gamma/2$ depends on the pulse duration $\tau_{\mathrm{pulse}}$ and leads to a sharp cut-off of the velocity distribution at $v_{\mathrm{max}} = n_{\mathrm{max}}v_{\mathrm{rec}}$. In general, the pulse duration will not change $f(v)$ for small velocities ($v_{\mathrm{c}} \ll v_{\mathrm{max}}$), where we can assume the distribution to be flat. A simulation of the number of scattered photons $n_{\mathrm{p}}$ yielding the velocity distribution $f(v)$ is shown in Fig. 4.2. Given the initial flat distribution over all magnetic sub-levels, we simulate their redistribution taking into account the appropriate branching ratios. Without loss of generality we chose $\sigma^+$-polarisation for the pushing beam. Once the cycling transition is reached, the probability to decay into the dark state $|F = 1\rangle$ is dramatically reduced. However, due to imperfect polarisation there is a small probability of performing a $\pi$- or $\sigma^-$-transition. It turns out that a probability of $2\%$ of exciting the wrong state (either by $\pi$- or $\sigma^-$-transition) is able to describe our measured error probabilities.

The probability of recapturing an atom as a function of the critical velocity is given by

$$P(v_{\mathrm{c}}) = \int_0^{v_{\mathrm{c}}} f(v)\,\mathrm{d}v = f_0 v_{\mathrm{c}} = \frac{f_0 r_0}{t} \equiv \frac{t_0}{t}. \tag{4.2}$$

The probability to decay after the first excitation is $f_0 v_{\mathrm{rec}}$. Likewise, since the probability distribution is flat, it is the same probability $R_{\mathrm{D}}/R_{\mathrm{sc}}$ to decay after any number of excitations. This leads

to

$$f_0 = \frac{R_\mathrm{D}}{R_\mathrm{sc} v_\mathrm{rec}} = \varepsilon \frac{\Omega_0^2}{4\Omega_\mathrm{eff}^2} \frac{1}{v_\mathrm{rec}}, \tag{4.3}$$

which can be used to obtain

$$t_0 = \varepsilon \frac{\Omega_0^2}{4\Omega_\mathrm{eff}^2} \frac{r_0}{v_\mathrm{rec}}. \tag{4.4}$$

In our case $t_0/\varepsilon = 2.9 \times 10^{-5}$ s. From the non-linear regression fit, shown in Fig. 4.1 (c), we obtain $t_0 = (5.14 \pm 2.86) \times 10^{-6}$ s. A resulting $\varepsilon = 0.2(1)$ means that the cycling transition allows for about five times more scattered photons before a decay to the dark state.

### 4.1.2 Monte-Carlo simulation

In order to check the validity of the analytical model, the error probability for resonantly pushing the $|F = 2\rangle$ atoms out of the recapture volume can be obtained from a Monte-Carlo simulation. The scattering of photons at a rate $R_\mathrm{sc}$ results in a radiation force on the atoms of $F_\mathrm{rad} = \hbar k R_\mathrm{sc}$ and thus an acceleration $a_0 = R_\mathrm{sc} h/m\lambda = v_\mathrm{rec} R_\mathrm{sc}$. We simulate one atom at a time, averaging over many realisations in the end. First we draw, for each spatial dimension $i \in \{x, y, z\}$, a random thermal velocity $v_0^i$ from a Gaussian distribution $f(v_i) = \sqrt{m/2\pi k_\mathrm{B} T} \exp\left(-m v_i^2 / 2 k_\mathrm{B} T\right)$ and random initial positions $x_0$, $y_0$ and $z_0$ from a Gaussian density distribution with a width of 35 µm. The pushing time is given by $\tau_\mathrm{pulse} = n_\mathrm{p} \tau$, with the number of scattered photons $n_\mathrm{p}$ and the atomic lifetime $\tau = 26$ ns. A constant acceleration over this time, here chosen along the $x$-direction, results in a final velocity of $v_1^x = a_0 \tau_\mathrm{pulse}$. A random walk of the atom due to heating during the scattering can be simulated by drawing $x_\mathrm{d}$, $y_\mathrm{d}$ and $z_\mathrm{d}$ from a Gaussian distribution with $\sigma_\mathrm{d} = v_\mathrm{rec} \sqrt{R_\mathrm{sc}} \tau_\mathrm{pulse}^{3/2} / 3$ [86]. The classical trajectories are then given by

$$x(t) = x_0 + x_\mathrm{d} + v_0^x t + v_1^x t + \frac{1}{2} a_0 \tau_\mathrm{pulse}^2 \tag{4.5}$$

$$y(t) = y_0 + y_\mathrm{d} + v_0^y t \tag{4.6}$$

$$z(t) = z_0 + z_\mathrm{d} + v_0^z t. \tag{4.7}$$

We calculate $r(t) = \sqrt{x^2 + y^2 + z^2}$ for varying release times $t$ and compare it to a MOT capture radius of $r_0 = 1$ mm, given by the size of the repumping beam. The results are shown in Fig. 4.3. We reach excellent agreement between the simulation and the measurement and we are able to confirm the analytical model previously obtained. In particular we see that indeed the initial position of the atoms, as well as their thermal velocity and heating during the scattering can be neglected and the problem reduces to one dimension.

We have shown the capability of state-selective atom counting in samples with up to 250 atoms for the sequential method. This relies on the measurement of the total atom number before the experimental sequence, from which the number of expelled atoms is deduced. The detection can be significantly improved by simultaneously detecting the number of atoms in each state at the end of the experiment.

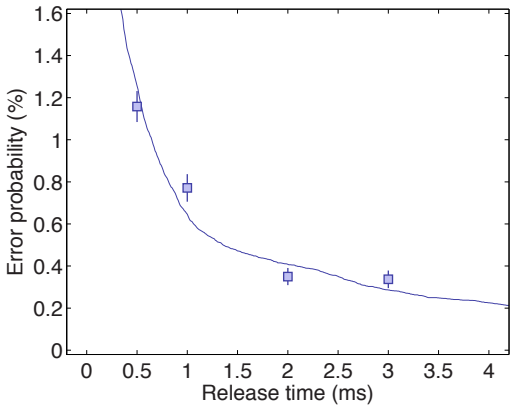


Figure 4.3: Monto-Carlo simulation of the error probability for varying release times. The simulation explains the measurement and confirms the analytical model of a scaling $\propto t^{-1}$.

## 4.2 New imaging system

The simultaneous state-selective detection of atom numbers in a split MOT, depicted in Fig. 4.4, requires a different imaging system than the detection of the total atom number. State-independent detection in a regular MOT favours a small magnification, possibly imaging the entire fluorescence onto a single CCD pixel or equivalently using an avalanche photo diode to generate the signal. The split MOT configuration requires a good optical resolution in order to reduce blurring of the two atomic densities and suppress signal overlap. A larger magnification reduces the effect of misalignment and mechanical instability when choosing a static region of interest.

### 4.2.1 Magnification

We exchange the secondary lens with a focal length of $f = 100\,\mathrm{mm}$ from the previous imaging system with an $f = 250\,\mathrm{mm}$ lens and use a gold foil, illuminated with collimated light from the back, as a test object to characterise the new imaging system. A $4\,\mathrm{mm}$ glas plate is placed between the gold foil and the objective lens to simulate the glas cell wall that is present in the actual experimental setup. The gold foil has a square pattern of holes with a spacing of $s = 20\,\mu\mathrm{m}$. Each hole has a diameter of $650\,\mathrm{nm}$, so we can treat it essentially as a point-like light source. The CCD image, shown in Fig. 4.5 (a), reveals the expected regular pattern. From a fit to multiple Gauss functions we obtain a mean distance of the peaks of $\Delta y = 6.01(8)$ pixels on the CCD image (Fig. 4.5 (b)). For this measurement a CCD camera[1] with a pixel size of $d = 17.2\,\mu\mathrm{m}$ was used. This results in a magnification of $M = d\Delta y/s = 5.17(7)$, in good agreement with the simple estimate of focal length ratios $M \sim 250\,\mathrm{mm}/50\,\mathrm{mm} = 5$.

[1] AVT Guppy F-044B NIR, using binned 'F7M2_Mono8_376x288' mode.

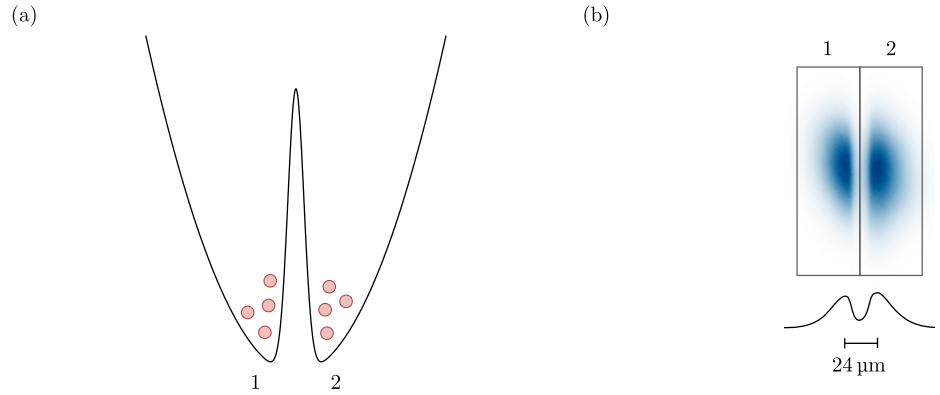


Figure 4.4: Scheme of the hybrid optical trap. (a) A blue-detuned focused light-sheet is superimposed with the harmonic MOT potential, resulting in a dissipative double-well system. (b) Example image of the atomic density in the split MOT. The line profile below, obtained by summing over the pixel columns, shows the separation of the density peaks in real space.

### 4.2.2 Depth of field

When an object is captured out of focus, its image is blurred. Due to the finite spatial extent of the atomic distribution, its image can be blurred and some of the signal lost, even when the focus is set correctly to the center of the cloud. This effect is quantified by the depth of field, which tells us how far an atom can be out of focus, before reaching an unacceptable blurring.

In order to obtain the depth of field, we measure the waist of the Gaussian signal distribution in image space for different distances of the objective lens from the test object, shown in Fig. 4.6 (a). We find the focus, i. e. the minimal waist, at a position of $+5\,\mu\text{m}$. The depth of field is obtained by finding the position at which the waist has increased by a factor of $\sqrt{2}$, in this case at $+33\,\mu\text{m}$. This yields a depth of field DOF $\approx 2(33\,\mu\text{m} - 5\,\mu\text{m}) = 56\,\mu\text{m}$.

The objective lens has a diameter of $D = 23\,\mu\text{m}$ and an effective focal length of $f = 50\,\text{mm}$, resulting in an $f$-number of $f/D = 2.17$. The circle of confusion $c$, a measure for the acceptable blurring in image space, can be assumed as the pixel size. When the object distance is close to the focal length, the depth of field can be approximated by [87]

$$\text{DOF} = \frac{2f(M+1)/M}{(fM)/(Nc) - (Nc)/(fM)} \approx 2c\frac{f}{D}\frac{M+1}{M^2} = 17\,\mu\text{m}. \tag{4.8}$$

The discrepancy between the calculation and the measurement can be explained by the limited resolution of the CCD chip, given by the pixel size, which makes the blurring harder to detect.

### 4.2.3 Resolution

The resolution of an imaging system is connected to its point-spread function (PSF), which is the system response to a point source. The resulting intensity is obtained by convoluting the object

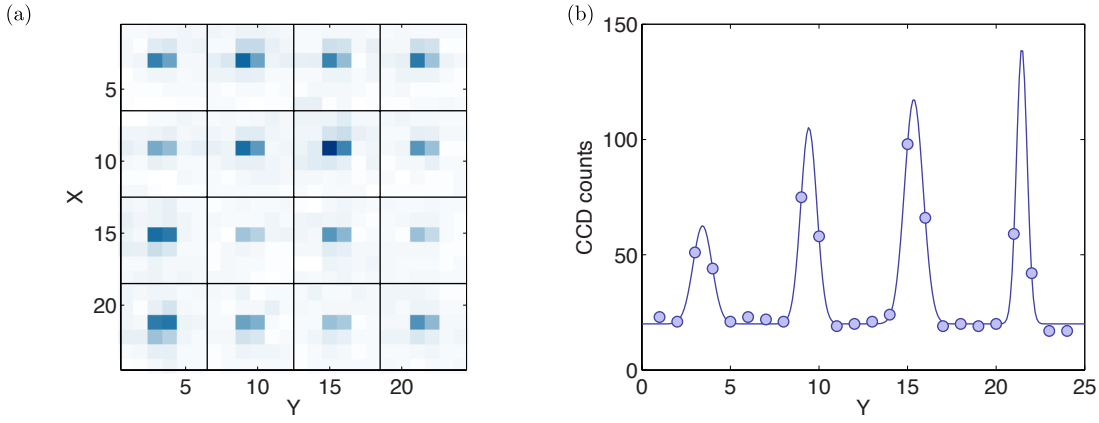


Figure 4.5: Measurement of the imaging magnification. (a) CCD image of the test object, a gold foiled with regularly spaced holes, which act as point-like light sources. (b) The magnification is deduced from a fit to the signal distribution using multiple Gauss functions.

plane field with the PSF. It can be shown that the intensity in the focus of the image plane is described by an Airy function

$$I(x) = I_0 \left( \frac{2J_1(x)}{x} \right)^2 , \tag{4.9}$$

where $I_0$ is the maximum intensity at the center, $J_1$ is the Bessel function of the first kind of order one and $x = \pi q/\lambda N$ with $q$ being the radial distance from the optical axis [88]. The $f$-number $N = (2\mathrm{NA})^{-1}$ can be substituted for the numerical aperture NA and we obtain $x = 2\pi q \mathrm{NA}/\lambda$. The best achievable resolution, i. e. the minimum distance between two distinguishable points, is given by the Rayleigh criterion as the first zero of $J_1(x)$, which is at $x = 3.83$. This corresponds to a dark ring at a radial distance of $q = 1.22\lambda N = 0.61\lambda/\mathrm{NA}$, defined as the resolution $\Delta r$. We calculate $\Delta r = 2.1\,\mu\mathrm{m}$ for the new imaging system.

In order to experimentally obtain the resolution, we average over the images of all 16 holes shown in Fig. 4.5 (a), where the objective was focused onto the center of the atomic cloud and obtain the number of CCD counts distributed across the $y$-direction. We fit the Airy function in Eqn. 4.9 to the intensity profile and obtain a resolution in image space of $\Delta r = 22\,\mu\mathrm{m}$. The results are shown in Fig. 4.6 (b). This corresponds to a resolution in object space of $\Delta r/M = 4.3\,\mu\mathrm{m}$. It is not surprising that the measured value is larger than the optimal resolution, since the theoretical limit assumes no aberrations.

## 4.3 Realisation of the light-sheet barrier

The purpose of the light-sheet is to split the MOT into a double-well potential. We set the wavelength close to the $D_1$ transition between $^2S_{1/2}$ and $^2P_{1/2}$ at $749.979\,\mathrm{nm}$ and chose a blue detuning of a few tens of GHz. For a limited laser power we can achieve a higher potential barrier

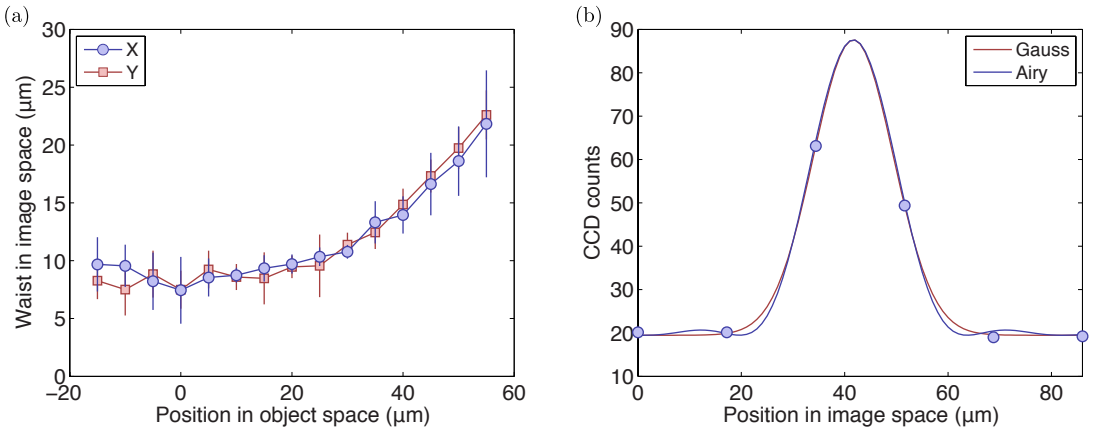


Figure 4.6: Measurement of depth of field and resolution. (a) The waist in image space for varying positions of the objective in object space is used to determine the depth of field. (b) A fit of the Airy function to the measured CCD counts reveals the resolution in image space. We see that a Gaussian distribution is a very good approximation of the Airy function.

height with by tuning the frequency close to resonance. Since we employ a narrowband optical filter at 780 nm, as described in Section 3.2, we chose the $D_1$ transition for the light-sheet in order to avoid stray light on the detected images. The light is generated by a Coherent Ti:Sa MBR laser with a maximum output power of 1.7 W, given our available pump power of 9.2 W. After acousto-optic modulation and fibre coupling of the light, as well as shaping the beam profile, we end up with a maximum of 400 mW at the position of the atoms. The Stark shift which causes the repulsion of the atoms from the intensity maximum of the barrier detunes the atomic states, rendering laser cooling inefficient. Therefore we have to alternately switch between light-sheet barrier and MOT beams. The pulsing is done with an acousto-optic modulator at a pulsing frequency of 125 kHz, a time scale much faster than the motion of the atoms in the trap, yet much slower than the lifetime of the excited state, such that laser cooling is still efficient during the period in which the MOT beams are turned on. Since the laser intensity inside the AOM is rather high, we observe considerable heating of the crystal manifested in a temporal efficiency change, such that we cannot choose pulsing frequencies below 5 kHz and it is best to stay well above.

In the following we will discuss in detail the creation of the light-sheet by shaping a spherical Gaussian laser beam into an elliptical beam with a large aspect ratio, as well as the calibration of the potential barrier height and the calculation of the trap frequencies.

### 4.3.1 Optical system

Let us first consider a spherical Gaussian laser beam, emitted from an optical fibre with a numerical aperture of NA $= 0.12$, corresponding to the opening angle $\theta$ of the divergent beam. The intensity distribution of a spherical Gaussian beam as a function of the radial distance $r$ to the optical axis

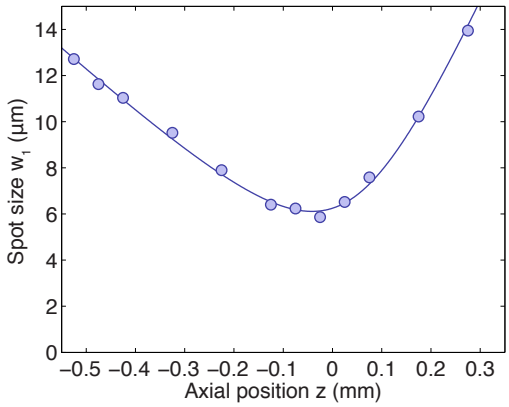


Figure 4.7: Spot size of the focused light-sheet without use of the cylindrical lens pair. An imperfect collimation leads to a tilt of the profile, which can be modelled as described in the main text.

and the position $z$ along the optical axis is

$$I(r,z) = I_0 \left(\frac{w_0}{w(z)}\right)^2 e^{-2r^2/w^2(z)}, \tag{4.10}$$

where $I_0 = I(0,0)$ is the maximum intensity and $w(z) = w_0\sqrt{1+(z/z_\mathrm{R})^2}$ is the spot size with $w_0 = w(z=0)$ being the minimal radial extent, i. e. the waist [88]. The Rayleigh range $z_\mathrm{R} = \pi w_0^2/\lambda$ depends on the wavelength, which for the characterisation of the optical system was $\lambda = 780\,\mathrm{nm}$. We collimate the divergent beam[2] using an achromatic doublet with a focal length of $f_0 = 50\,\mathrm{mm}$ and measure a waist of $w_0 = 5.98\,\mathrm{mm}$. This corresponds to a waist at the fibre end of $w' = \lambda f_0/\pi w_0 = 2.1\,\mu\mathrm{m}$ or equivalently an opening angle of $\theta \simeq \lambda/\pi w' = 0.12$, confirming the numerical aperture stated in the fibre data sheet.

Next, we focus the Gaussian beam using an achromatic doublet with a focal length of $f_1 = 100\,\mathrm{mm}$, expecting a waist of $\lambda f_1/\pi w_0 = 4.2\,\mu\mathrm{m}$. A razor blade measurement of the spot size at different axial positions, shown in Fig. 4.7, reveals a tilt of the profile, possibly due to imperfect collimation, which can be modelled by

$$w(z) = w_1\sqrt{1+\left(\frac{z}{z_\mathrm{R}}\right)^2} + az. \tag{4.11}$$

We find $a = 1.5(3)\times 10^{-2}$ and a waist of $w_1 = 6.1(4)\,\mu\mathrm{m}$.

In order to achieve an elliptically shaped beam we use a pair of cylindrical lenses, which alter only one dimension of the radial beam profile. The pair, which consist of a plano-convex lens with focal length $f_2 = 200\,\mathrm{mm}$ and a plano-concave lens with a focal length of $-f_2$, is placed in between the collimating lens with focal length $f_0$ and the focusing lens with focal length $f_1$, as

[2] We check the collimation using a Melles Griot shear plate.

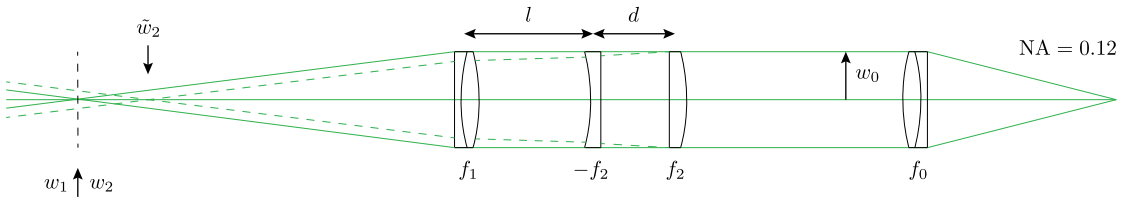


Figure 4.8: Scheme of the light-sheet optical system. The fibre output is collimated to a waist $w_0$ and slightly focused in one transversal dimension (dashed red lines) by a pair of cylindrical lenses with focal lengths $f_2$ and $-f_2$, separated by a distance $d$. After free propagation over a distance $l$, both transversal dimensions are focused by an aspherical doublet with focal length $f_1$, resulting in a shift of the waist $\tilde{w}_2$ towards the focusing lens. At the position of the atoms (dashed black line) we obtain an elliptical beam with a large aspect ratio between the spot sizes $w_1$ and $w_2$.

shown in Fig. 4.8. The two cylindrical lenses are separated by a distance $d$ and placed at a distance $l$ from the spherical focusing lens. In this configuration the pair of cylindrical lenses introduces a slight focusing of the beam along one radial dimension, such that, after passing the spherical lens, the focus in that dimension is shifted with respect to the focus of the unperturbed dimension. This leads to an increased spot size $w_2$ at a distance of $f_1$ from the spherical lens, i. e. at its focus. We will show that $w_2$ can be adjusted over a large range by varying $d$, while it is independent of the distance $l$, rendering the configuration versatile, yet stable.

A Gaussian beam can be described by the complex beam parameter $q(z) = z + iz_\mathrm{R}$ or its inverse form

$$\frac{1}{q(z)} = \frac{1}{R(z)} - \frac{i\lambda}{\pi w^2(z)} \tag{4.12}$$

with the radius of curvature $R(z) = z(1 + (z_\mathrm{R}/z)^2)$. The Rayleigh length is given by $z_\mathrm{R} = \mathrm{Im}(q)$ and the distance from the waist by $s = -\mathrm{Re}(q)$. Changes to an initial beam parameter $q_1$, e. g. through propagation in free space or focusing with a thin lens, resulting in a final beam parameter $q_2$, can be expressed with help of a *ray transfer matrix*

$$\begin{pmatrix} q_2 \\ 1 \end{pmatrix} = k \begin{pmatrix} A & B \\ C & D \end{pmatrix} \begin{pmatrix} q_1 \\ 1 \end{pmatrix}, \tag{4.13}$$

where $k$ has to be chosen such, that the final vector is correctly normalised [88]. Equivalently the new beam parameter can be expressed as

$$q_2 = \frac{Aq_1 + B}{Cq_1 + D}. \tag{4.14}$$

The ray transfer matrix of a propagation in free space over a distance $d$ is given by

$$\begin{pmatrix} 1 & d \\ 0 & 1 \end{pmatrix}, \tag{4.15}$$

whereas the focusing with a thin lens with focal length $f$ is described by

$$\begin{pmatrix} 1 & 0 \\ -1/f & 1 \end{pmatrix}. \tag{4.16}$$

We begin our analysis of the beam after its collimation using the $f_0$ spherical lens. The radius of curvature can be assumed infinite and we are left with an initial beam parameter $q_0 = i\pi w_0^2/\lambda$. Let us first consider the optical system without the pair of cylindrical lenses. The beam undergoes free propagation, which at a large waist of $w_0$ does not significantly change the beam parameter, until it reaches the spherical lens, where it is focused. We are interested in the beam parameter $q_1$ at a distance $f_1$ from the focusing lens, where it is given by

$$\begin{pmatrix} q_1 \\ 1 \end{pmatrix} = k \begin{pmatrix} 1 & f_1 \\ 0 & 1 \end{pmatrix} \begin{pmatrix} 1 & 0 \\ -1/f_1 & 1 \end{pmatrix} \begin{pmatrix} q_0 \\ 1 \end{pmatrix} = k \begin{pmatrix} f_1 \\ 1 - q_0/f_1 \end{pmatrix}. \tag{4.17}$$

Normalisation is given by $k = (1 - q_0/f_1)^{-1}$ and we obtain $q_1 = f_1(1 - q_0/f_1)^{-1}$. The Rayleigh range in this case is

$$z_{\mathrm{R},1} = \mathrm{Im}(q_1) = \frac{f_1^2 \pi w_0^2 \lambda}{\pi^2 w_0^4 + f_1^2 \lambda^2} \simeq \frac{f_1^2 \lambda}{\pi w_0^2} = 69\,\mu\mathrm{m}, \tag{4.18}$$

from which we calculate a waist of $w_1 = \sqrt{z_{\mathrm{R},1}\lambda/\pi} = f_1\lambda/\pi w_0 = 4.2\,\mu\mathrm{m}$, in accordance with our previous theoretical expectation.

Now we introduce the cylindrical lens pair and consider $q_2$, again at the position $f_1$ from the spherical focusing lens, where it is given by

$$\begin{pmatrix} q_2 \\ 1 \end{pmatrix} = k \begin{pmatrix} 1 & f_1 \\ 0 & 1 \end{pmatrix} \begin{pmatrix} 1 & 0 \\ -1/f_1 & 1 \end{pmatrix} \begin{pmatrix} 1 & l \\ 0 & 1 \end{pmatrix} \begin{pmatrix} 1 & 0 \\ 1/f_2 & 1 \end{pmatrix} \begin{pmatrix} 1 & d \\ 0 & 1 \end{pmatrix} \begin{pmatrix} 1 & 0 \\ -1/f_2 & 1 \end{pmatrix} \begin{pmatrix} q_0 \\ 1 \end{pmatrix}. \tag{4.19}$$

Using the correct normalisation we obtain

$$q_2 = \frac{f_1^2(f_2^2 + d(f_2 - q_0))}{f_2^2(f_1 - l - q_0) - d(f_2 - f_1 + l)(f_2 - q_0)} \tag{4.20}$$

and a Rayleigh range of

$$z_{\mathrm{R},2} = \mathrm{Im}(q_2) \simeq \frac{f_2^4 f_1^2 \lambda}{(f_2^2 - d(f_2 - f_1 + l))^2 \pi w_0^2}, \tag{4.21}$$

which in the limit of $d \to 0$ reduces to the result in Eqn. 4.18. For a finite distance $d$ the Rayleigh range is increased and thus also the waist $\tilde{w}_2$. At the same time, the focus, i. e. the axial position of the waist, is shifted by

$$s = -\,\mathrm{Re}(q_2) \simeq -\frac{f_1^2 d}{f_2^2 - d(f_2 - f_1 + l)}, \tag{4.22}$$

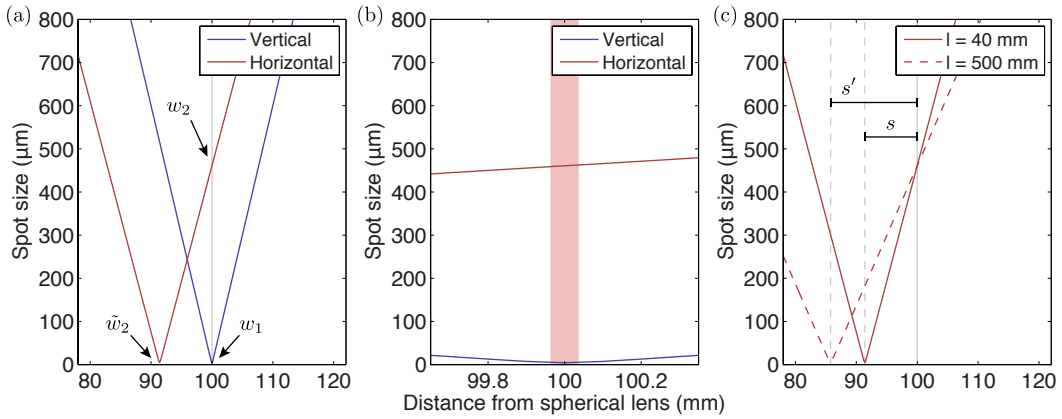


Figure 4.9: Calculations of the expected light-sheet spot sizes. (a) Overview of the vertical and horizontal spot sizes inside the glass cell for parameters $d = 30\,\mathrm{mm}$ and $l = 40\,\mathrm{mm}$. The focus of the horizontal dimension $\tilde{w}_2$ is shifted towards the focusing lens, resulting in a large spot size $w_2$ at the position of the vertical focus $w_1$. (b) The red shaded area illustrates the region occupied by the atoms, over which the horizontal beam spot size changes be less than $1\%$. (c) Changing the position of the cylindrical lens pair $l$, results in a different shift of the focus, however, the spot size at the position of the atoms is unaffected.

hence we have to consider the spot size at a distance $f_1$ from the focusing lens

$$w_2 = \tilde{w}_2\sqrt{1+\left(\frac{s}{z_{\mathrm{R},2}}\right)^2} = \sqrt{\frac{\lambda}{\pi}\left(z_{\mathrm{R},2}+\frac{s^2}{z_{\mathrm{R},2}}\right)} \equiv \sqrt{\frac{\lambda}{\pi}\frac{|q_2(s)|^2}{\mathrm{Im}(q_2(s))}}$$
$$= \frac{f_1}{\pi w_0}\sqrt{\frac{d^2\pi^2 w_0^4 + f_2^2(d+f_2)^2\lambda^2}{f_2^4}} \simeq \frac{df_1}{f_2^2}w_0, \tag{4.23}$$

which is independent of the distance $l$ and can be linearly tuned by varying $d$. Fig. 4.9 shows calculations of the beam profile around the focal length $f_1$ in a region which corresponds to the size of the glass cell and a smaller region on the order of the atom cloud size. Since we image the atoms horizontally, we will chose the vertical axis as the one with the small waist $w_1$, while horizontally the beam will have a spot size of $w_2$ at the position of the atoms. Note that the uncoated glass cell wall with a thickness of $4\,\mathrm{mm}$ shifts both focal points by $1.3\,\mathrm{mm}$, but leaves the spot sizes $w_1$ and $w_2$ unchanged.

Experimentally we realise the optical system as follows. The optical elements, such as fibre out-coupler and lenses, are mounted onto a Thorlabs cage system, shown in Fig. 4.10(a), which ensures a fixed optical axis. We use rotation mounts to adjust the tilt of the two cylindrical lenses[3] and a high-precision zoom housing[4] for the final adjustment of the spherical focusing lens

[3]Thorlabs LJ1653RM-B ($f = 200\,\mathrm{mm}$) and LK1069RM-B ($f = -200\,\mathrm{mm}$).
[4]Thorlabs SM1ZM, non-rotating, 4 mm travel.

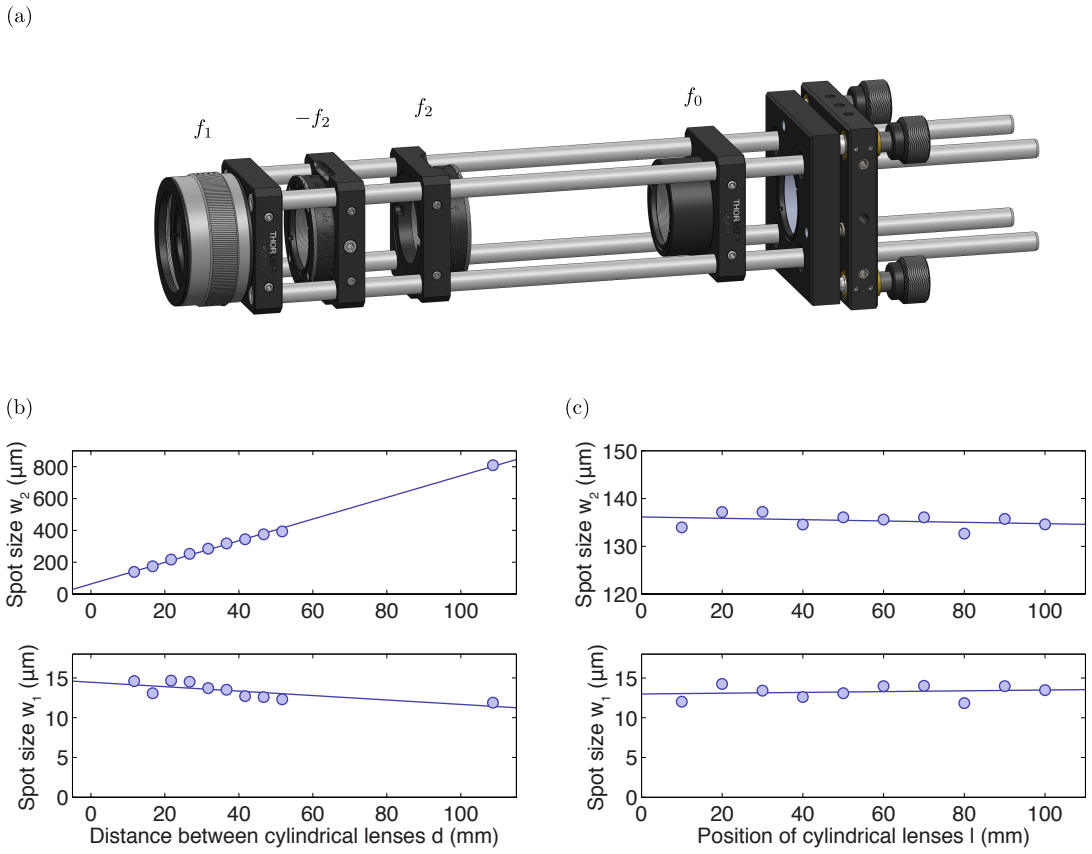


Figure 4.10: Experimental realisation of the light-sheet. (a) A cage system is used to co-axially mount the optical elements. (b) Measurement of the spot sizes confirm that $w_2$ can be linearly tuned by varying the distance $d$ between the cylindrical lenses. Due to the limited resolution of the imaging, given in this case by a pixel size of $17.2\,\mu m$, a precise measurement of the spot size $w_1$ is not possible, however, we can give an upper bound for the change. (c) Varying the position $l$ of the cylindrical lens pair leaves both $w_2$ and $w_1$ unaffected.

position. We use a CCD camera to adjust the tilt of the light-sheet and measure the beam profile, from which we extract both vertical and horizontal spot sizes for different distances between the cylindrical lenses (Fig. 4.10(b)) and different positions of the cylindrical lens pair along the optical axis (Fig. 4.10(c)). This particular setup allows us to set the distance $d$ between $12\,mm$ and a maximum of $109\,mm$. The resulting range of horizontal spot sizes from $140\,\mu m$ to $810\,\mu m$, corresponds to a variable aspect ratio of the light-sheet between 23:1 and 140:1. Limited laser power favours a small waist in order to increase the intensity, while a larger waist reduces the probability that the atoms travel to regions of the light-sheet where the intensity is significantly reduced compared to $I_0$. With this in mind, we chose a horizontal waist of $w_2 = 400\,\mu m$ as the final configuration.

### 4.3.2 Calibration of the potential barrier height

The precise determination of the atom number in each site of the split MOT requires a large potential barrier that suppresses particle exchange. Here we will calculate the potential barrier height for our experimental laser parameters. The intensity profile of the elliptical Gaussian laser beam is given by

$$I(x,y,z) = I_0 \frac{w_1}{w_1(z)} \frac{w_2}{w_2(z)} \exp\left(\frac{-2xy}{w_1(z)w_2(z)}\right), \tag{4.24}$$

where $I_0 = I(0,0,0) = 2P/(\pi w_1 w_2)$ is the intensity at the center of the beam with power $P$ and $w_i(z) = w_i\sqrt{1+(z/z_{\mathrm{R},i})^2}$ with the Rayleigh ranges $z_{\mathrm{R},i} = \pi w_i^2/\lambda$. The $D_1$ line has a wavelength of $\lambda = 795\,\mathrm{nm}$ and a natural linewidth $\Gamma = 2\pi \times 5.7\,\mathrm{MHz}$. The waists are $w_1 = 6\,\mu\mathrm{m}$ and $w_2 = 400\,\mu\mathrm{m}$, as described above. Assuming $\pi$-polarisation, the saturation intensity for the $D_1$ line is $I_{\mathrm{sat}} = 44.86\,\mathrm{W/m^2}$. The corresponding Rabi frequency is

$$\Omega = \Gamma\sqrt{\frac{I}{2I_{\mathrm{sat}}}}, \tag{4.25}$$

and the potential barrier height, given by the resulting Stark shift, can be expressed as

$$\Delta V = \frac{\hbar\Omega^2}{4\Delta} = \frac{\hbar}{4\Delta}\frac{\Gamma^2}{I_{\mathrm{sat}}}\frac{P}{\pi w_1 w_2}, \tag{4.26}$$

where $\Delta$ is the light sheet detuning. For the state-selective detection of atom numbers we use a detuning of $\Delta = 2\pi \times 13\,\mathrm{GHz}$ and we can reach mean laser powers of up to $200\,\mathrm{mW}$[5]. With these parameters we expect a barrier height of up to $18\,\mathrm{mK}$. We will later see that the observed potential barrier heights are lower than expected from Eqn. 4.26, albeit still much larger than the MOT temperature of $\sim 80\,\mu\mathrm{K}$. Scattering from the light-sheet can happen at a maximum rate of $R_{\mathrm{sc}} = \Gamma\Delta V/\hbar\Delta \approx 2\pi \times 0.2\,\mathrm{MHz}$, although usually the rate is much lower, since the atoms are repelled from the position of highest intensity. In any case, the scattering rate is considerably smaller than the scattering rate from the MOT light, which is close to $\Gamma/2$.

### 4.3.3 Calculation of the trapping frequencies

Superimposing the light-sheet onto the MOT results in a double-well with two potential minima and a local maximum at the centre. We will now calculate the trapping frequencies of the system and compare them to the trapping frequency of the harmonic potential of the MOT. The MOT is characterised by the detuning $\delta = -\Gamma$, the saturation intensity $s_0 = I/I_{\mathrm{sat}} = 7$ and the magnetic field gradient $B' = 10\,\mathrm{G/cm}$. A laser wavelength of $\lambda = 780\,\mathrm{nm}$ corresponds to a wavenumber of $k = 2\pi/\lambda = 8 \times 10^6\,\mathrm{m^{-1}}$. The MOT spring constant is given by

$$\kappa = m\omega^2 = \frac{8k\mu_{\mathrm{B}}B' s_0(-\delta/\Gamma)}{(1+(2\delta/\Gamma)^2)^2} = 1.7 \times 10^{-17}\,\mathrm{N\,m^{-1}}, \tag{4.27}$$

[5]We recall that the light-sheet is pulsed, resulting in an average laser power of half the maximum value that we would reach in a continuous mode.

where $m$ is the $^{87}$Rb mass and $\mu_\mathrm{B}$ is the Bohr magneton [89]. This gives a natural MOT trapping frequency of $\omega = 2\pi \times 1.7\,\mathrm{kHz}$. The damping coefficient follows as

$$\gamma = \frac{\hbar k}{\mu_\mathrm{B} B'}\omega^2 = \frac{\hbar k}{\mu_\mathrm{B} B'}\frac{\kappa}{m} = \frac{\alpha}{m} = 2\pi \times 17\,\mathrm{kHz}, \tag{4.28}$$

with the damping constant $\alpha$ obeying

$$\boldsymbol{F}_\mathrm{molasses} = m\frac{\mathrm{d}\boldsymbol{v}}{\mathrm{d}t} = -\alpha\boldsymbol{v} \rightarrow \boldsymbol{v}(t) = \boldsymbol{v}_0 e^{-\gamma t}. \tag{4.29}$$

The MOT potential is given by $V_\mathrm{MOT}(x) = m\omega^2 x^2/2$ and the light sheet potential by $V_\mathrm{LS}(x) = \Delta V \exp(-2x^2/w_1^2)$ with a beam waist of $w_1 = 6\,\mu\mathrm{m}$ and the potential barrier height $\Delta V$. The extreme values of the total potential $V = V_\mathrm{MOT} + V_\mathrm{LS}$ are obtained from

$$V'(x) = m\omega^2 x + \Delta V \exp\left(-\frac{2x^2}{w_1^2}\right)\left(-\frac{4x}{w_1^2}\right) = 0 \tag{4.30}$$

and given by the position of the barrier $x_\mathrm{b} = 0$ and the two potential minima

$$\pm x_\mathrm{m} = \pm w_1 \sqrt{\frac{1}{2}\log\left(\frac{4\Delta V}{\kappa w_1^2}\right)}. \tag{4.31}$$

The trapping frequencies are calculated from

$$V''(x) = m\omega^2 + \Delta V \exp\left(-\frac{2x^2}{w_1^2}\right)\left\{\frac{16x^2}{w_1^4} - \frac{4}{w_1^2}\right\}. \tag{4.32}$$

The (anti-)trapping frequency at the position of the barrier is given by

$$\omega_\mathrm{b} = \sqrt{\frac{|V''(x_\mathrm{b})|}{m}} = \omega\sqrt{\left|1 - \frac{4\Delta V}{\kappa w_1^2}\right|} \tag{4.33}$$

and the trapping frequency at the potential minima by

$$\omega_0 = \sqrt{\frac{V''(x_\mathrm{m})}{m}} = \omega\sqrt{2\log\left(\frac{4\Delta V}{\kappa w_1^2}\right)}. \tag{4.34}$$

For $\Delta V \rightarrow 0$, the natural trapping frequency $\omega$ is retrieved at the center of the trap $x_\mathrm{b} = 0$, while for $\Delta V \leq \kappa w_1^2/4 = k_\mathrm{B} \times 0.5\,\mu\mathrm{K}$ there no longer is a trapping frequency at $x_\mathrm{m}$. Calculations of the trapping frequencies for a range of barrier heights are shown in Fig. 4.11.

## 4.4 Covariance analysis

In order to investigate the limits of simultaneous state-selective atom counting, we turn to a noise analysis similar to the one in Chapter 3, but now extended to our novel hybrid trap. We have

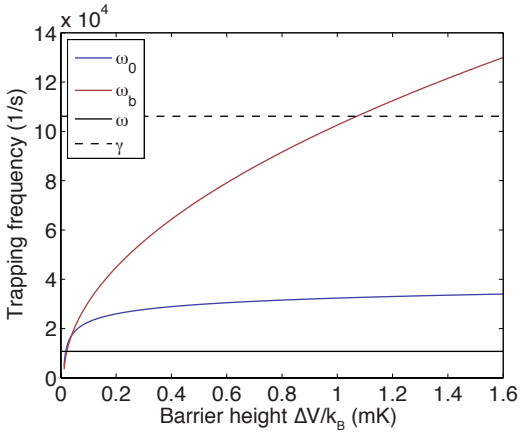


Figure 4.11: The trapping frequency $\omega_0$ (blue solid line) and the (anti-)trapping frequency $\omega_\mathrm{b}$ (red solid line) both increase as a function of the barrier height $\Delta V$, whereas the unperturbed MOT trapping frequency $\omega$ (black solid line) and the damping constant $\gamma$ (black dashed line) are not influenced. While $\omega_0 < \gamma$ at all times, $\omega_\mathrm{b}$ becomes comparable to $\gamma$ at large barrier heights.

seen before, that loss out of the trap can be a major limitation for single-particle resolved atom number detection. We consider the number of particles $N_1$ and $N_2$ in site 1 and 2, respectively, and quantify the rates of loss due to collisions with the background gas by the lifetimes $\tau_1$ and $\tau_2$. Loss due to light-assisted collisions is described by the rates $\beta_1$ and $\beta_2$. Additionally, atoms can hop from one site to the other, either by thermal activation, denoted as $\tau_{12}$ and $\tau_{21}$, or by gaining enough energy in the process of a light-assisted collision ($\beta_{12}$ and $\beta_{21}$). All the processes are illustrated in Fig. 4.12. The change in the atom numbers $N_1$ and $N_2$ can be described by

$$\begin{aligned}\begin{pmatrix}\dot{N}_1\\ \dot{N}_2\end{pmatrix} &= \begin{pmatrix}-(\tau_1^{-1}+\tau_{12}^{-1}) & \tau_{21}^{-1}\\ \tau_{12}^{-1} & -(\tau_2^{-1}+\tau_{21}^{-1})\end{pmatrix}\begin{pmatrix}N_1\\ N_2\end{pmatrix}\\ &\quad+\begin{pmatrix}-(\beta_1+\beta_{12}) & \beta_{21}\\ \beta_{12} & -(\beta_2+\beta_{21})\end{pmatrix}\begin{pmatrix}N_1^2\\ N_2^2\end{pmatrix}\\ &\equiv R\begin{pmatrix}N_1\\ N_2\end{pmatrix}+B\begin{pmatrix}N_1^2\\ N_2^2\end{pmatrix},\end{aligned} \tag{4.35}$$

where matrices $R$ and $B$ account for one- and two-body dynamics, respectively. This leads to an extension of the noise model, which we have discussed in Section 3.6. The total variances in site 1 and 2 can be expressed as

$$\begin{aligned}\sigma_1^2 = &\frac{N_1}{\eta R_\mathrm{sc}}t^{-1}+(\alpha N_1)^2 t^{-1}+\frac{N_1}{2\tau_1}t+\frac{N_1}{2\tau_{12}}t+\frac{N_2}{2\tau_{21}}t\\ &+\beta_1 N_1^2 t+\beta_{12}N_1^2 t+\beta_{21}N_2^2 t\end{aligned} \tag{4.36}$$

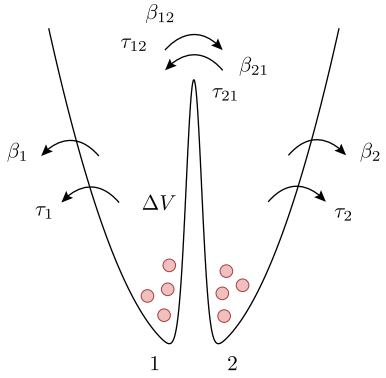


Figure 4.12: Scheme of the dynamics in the hybrid trap. In addition to loss via background scattering and light-assisted collisions in each site, there is particle exchange between the sites, induced either by thermal activation or collisional activation.

and

$$\sigma_2^2 = \frac{N_2}{\eta R_{\mathrm{sc}}} t^{-1} + (\alpha N_2)^2 t^{-1} + \frac{N_2}{2\tau_2} t + \frac{N_2}{2\tau_{21}} t + \frac{N_1}{2\tau_{12}} t + \beta_2 N_2^2 t + \beta_{21} N_2^2 t + \beta_{12} N_1^2 t, \tag{4.37}$$

where we have assumed that the photon shot noise parameter $\eta R_{\mathrm{sc}}$ and the fluorescence noise parameter $\alpha$ are independent of the site. We see that the variance in one site depends on the atom number in the adjacent one. In order to simplify the model and extract the relevant experimental parameters, we consider the case in which $N_1 \approx N_2$ and obtain for i = 1,2

$$\sigma_i^2 = \frac{N_i}{\eta R_{\mathrm{sc}}} t^{-1} + (\alpha N_i)^2 t^{-1} + \frac{N_i}{2\tilde{\tau}_i} t + \tilde{\beta}_i N_i^2 t, \tag{4.38}$$

with $\tilde{\tau}_i^{-1} = \tau_i^{-1} + \tau_{12}^{-1} + \tau_{21}^{-1}$ and $\tilde{\beta}_i = \beta_i + \beta_{12} + \beta_{21}$. Due to increased background signal with the new imaging system, we have to include a noise term $\gamma t^{-1}$ into our model, which was previously insignificant. This term, independent of the atom number, quantifies noise due stray light, which averages down with increasing integration time. We fix $\eta R_{\mathrm{sc}} = 58\,496\,\mathrm{s}^{-1}$ and fit the resulting noise model

$$\sigma_i^2 = \frac{N_i}{\eta R_{\mathrm{sc}}} t^{-1} + \gamma t^{-1} + (\alpha N_i)^2 t^{-1} + \frac{N_i}{2\tilde{\tau}_i} t + \tilde{\beta}_i N_i^2 t \tag{4.39}$$

to the experimentally obtained two-sample variance $\mathrm{Var}(S_{n+1} - S_n)/2$, shown in Fig. 4.13(a), for a range of four different integration times and ten different mean atom numbers. Figure 4.13(b) shows a representation of this simultaneous fit for a fixed atom number of 450 and different integration times. We find an optimal integration time between 80 ms and 120 ms, coinciding with the value of 100 ms from the total atom number measurement in Section 3.6. In Fig. 4.13(c) we plot

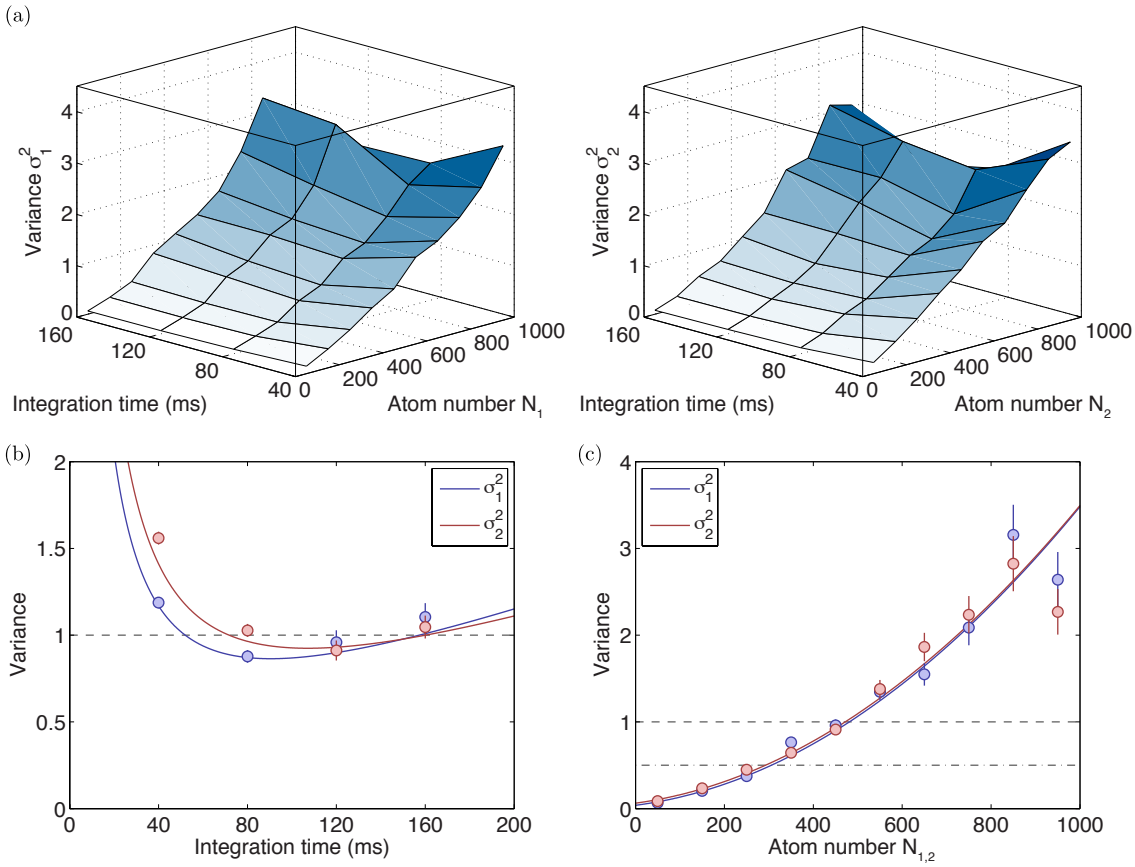


Figure 4.13: Variance analysis with extended noise model. (a) Entire measurement of the total variance in each site. (b) The variance, shown here for about 450 atoms in each site, reveals a minimum for an optimal integration time between 80 ms and 120 ms. The solid lines are representations of simultaneous fits to four different integration times and and a range of ten different atom numbers. (c) For an integration time of 120 ms, the variance reaches the single-particle resolution limit $\sigma^2 = 1$ at 470 atoms in each site. Precisely measuring the atom number difference $N_1 - N_2$ might be naively expected up to a variance of $\sigma^2 = 1/2$, as described in the main text.

Table 4.1: Fit parameters for the different noise models.

| Noise model | $\gamma$ [s] | $\alpha$ [$s^{1/2}$] | $\tilde{\tau}$ [s] | $\tilde{\beta}$ [$s^{-1}$] |
|---|---|---|---|---|
| $\sigma_1^2$ | $4.6(7) \times 10^{-3}$ | $3.6(3) \times 10^{-4}$ | 120(52) | $1.4(7) \times 10^{-5}$ |
| $\sigma_2^2$ | $7.6(12) \times 10^{-3}$ | $4.1(4) \times 10^{-4}$ | 110(67) | $1.1(10) \times 10^{-5}$ |
| $\sigma_+^2$ | $1.2(2) \times 10^{-2}$ | $2.6(2) \times 10^{-4}$ | 120(59) | $5(30) \times 10^{-7}$ |
| $\sigma_-^2$ | $1.2(2) \times 10^{-2}$ | $2.9(3) \times 10^{-4}$ | 100(51) | $1.2(5) \times 10^{-5}$ |

the variance as a function of the atom number for a fixed integration time of 120 ms in order to find the single-particle resolution limit $\sigma^2 = 1$. Since the atom numbers $N_1$ and $N_2$ were kept equal in the experiment, the noise is similar in both sites and we find a limit of single-particle resolved detection of up to 470 atoms in each site. We might naively expect a single-atom resolution limit for measuring the atom number difference of $\sigma_1^2 + \sigma_2^2 = 1$, which in our case is reached for 300 atoms in each site. However, we will see that this is not the full expression for the variance of a difference measurement.

We turn to the analysis of the total atom number $N_+ = N_1 + N_2$ and the atom number difference $N_- = N_1 - N_2$, shown in Figure 4.14, for which the noise model reads

$$\sigma_{+,-}^2 = \frac{N_+}{\eta R_{\mathrm{sc}}} t^{-1} + \gamma_+ t^{-1} + (\alpha_+ N_+)^2 t^{-1} + \frac{N_+}{2\tilde{\tau}_{+,-}} t + \tilde{\beta}_{+,-} N_+^2 t, \tag{4.40}$$

where $\tilde{\tau}_+$ and $\tilde{\beta}_+$ are equivalent to the one- and two-body decay parameters introduced in Section 3.3. Table 4.1 shows the noise parameters obtained from the different noise models. Comparing the results for $\sigma_1^2$ and $\sigma_2^2$ we find that, within the error of the measurement, $\alpha$ is indeed independent of the site, as expected. The same holds for the one-body parameter $\tilde{\tau}$ and the two-body parameter $\tilde{\beta}$.

For $\sigma_+^2$ the fluorescence noise parameter $\alpha_+$ is slightly smaller, in agreement with the measurement in Section 3.6. The one-body parameter $\tilde{\tau}$, here corresponding to the lifetime of the trap, is reduced compared to the earlier measurement, and coincides with the one-body parameter in $\sigma_{1,2}^2$. From this we deduce that the potential barrier height of $\Delta V / k_{\mathrm{B}} = 1.4\,\mathrm{mK}$ is large enough, such that thermal hopping between the two sites of the double-well is negligible, and the one-body limitation is solely given by the loss from the trap. The situation is different for dynamics due to light-assisted collisions. From $\sigma_+^2$ we obtain a two-body parameter, comparable to earlier measurements, which is orders of magnitude smaller than the $\tilde{\beta}$ parameter in $\sigma_1^2$ and $\sigma_2^2$, where the noise is dominated by collisionally activated hopping. With the given barrier height we are in a regime in which thermal hopping between the sites is strongly suppressed, however, light-assisted collisions, due to their longer-ranged exponential energy distribution still contribute significantly.

A measurement of the atom number difference $N_1 - N_2$ has a variance of $\sigma_-^2$ and the fit parameters, shown in Table 4.1, enforce the interpretation that the noise is dominated by particle exchange due to light-assisted collisions. We find a single-particle resolution limit of $\sigma_-^2 = 1$ for a

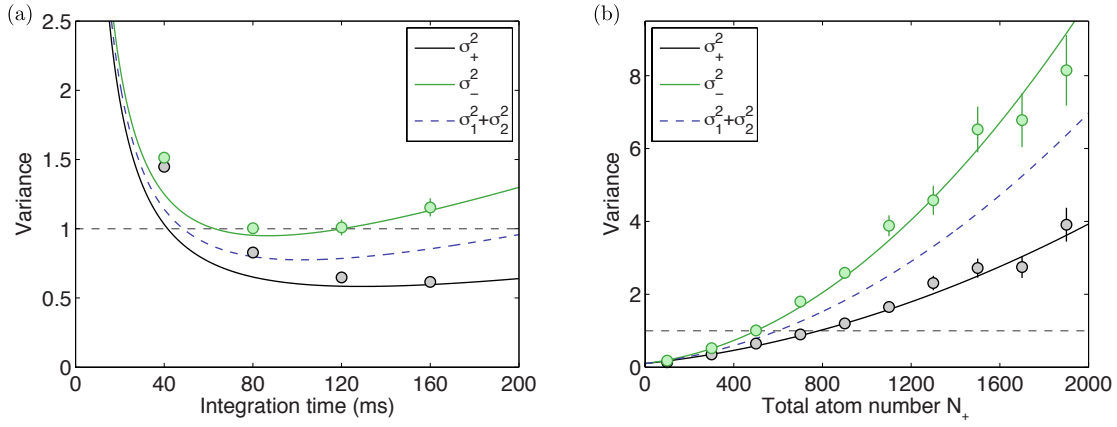


Figure 4.14: Variance analysis of the total atom number and the atom number difference. (a) We find different optimal integration times for measuring the sum and the difference atom number, shown here for a mean atom number of 500. (b) For an integration time of 120 ms, optimised for measuring the atom number difference, we find the single-particle resolution limit at 500 atoms for measuring $N_-$ (green solid line) and close to 800 atoms for measuring $N_+$ (black solid line). In between lies the sum of the individual variances (blue dashed line).

total atom number of 500. This is worse than the 600 atoms, naively estimated from the condition $\sigma_1^2 + \sigma_2^2 = 1$, i. e. $\sigma^2 = 1/2$, with $\sigma_1^2 \approx \sigma_2^2$. The reason for this will be discussed in the following.

We consider the expression

$$\begin{aligned}\sigma_1^2 + \sigma_2^2 = &\frac{N_1 + N_2}{\eta R_{\mathrm{sc}}} t^{-1} + 2\gamma t^{-1} + \alpha^2 (N_1^2 + N_2^2) t^{-1} \\ &+ \frac{N_1 + N_2}{2\tau} t + \frac{N_1 + N_2}{\tau_{\mathrm{ex}}} t + \beta (N_1^2 + N_2^2) t + 2\beta_{\mathrm{ex}} (N_1^2 + N_2^2) t, \end{aligned} \tag{4.41}$$

with decay parameters $\tau \equiv \tau_1 \approx \tau_2$ and $\beta \equiv \beta_1 \approx \beta_2$, as well as exchange parameters $\tau_{\mathrm{ex}} \equiv \tau_{12} \approx \tau_{21}$ and $\beta_{\mathrm{ex}} \equiv \beta_{12} \approx \beta_{21}$, and compare it to the sum variance

$$\begin{aligned}\sigma_+^2 = &\frac{N_1 + N_2}{\eta R_{\mathrm{sc}}} t^{-1} + \gamma_+ t^{-1} + \alpha_+^2 (N_1 + N_2)^2 t^{-1} \\ &+ \frac{N_1 + N_2}{2\tau} t + \beta (N_1 + N_2)^2 t. \end{aligned} \tag{4.42}$$

First of all, we equate $\gamma_+ = 2\gamma$, in accordance with the fit parameters in Table 4.1. Since we consider similar atom numbers $N_1 \approx N_2$, we can set $(N_1 + N_2)^2 \approx 2(N_1^2 + N_2^2)$. This results in $\sqrt{2}\alpha_+ = \alpha$, also evident from the obtained fit parameters. Overall we find

$$\sigma_+^2 = \sigma_1^2 + \sigma_2^2 + 2\mathrm{Cov}(N_1, N_2) \tag{4.43}$$

with the atom covariance

$$\mathrm{Cov}(N_1, N_2) \equiv -\frac{1}{2} \left( \frac{N_1 + N_2}{\tau_{\mathrm{ex}}} + \beta_{\mathrm{ex}} (N_1 + N_2)^2 \right) t. \tag{4.44}$$

Analogously, we set

$$\sigma_-^2 = \sigma_1^2 + \sigma_2^2 - 2\mathrm{Cov}(N_1, N_2) \tag{4.45}$$

and now it becomes clear, why the variance of the difference measurement is larger than the sum of the two individual variances. Likewise the variance for the sum measurement is reduced, since it is independent of particle exchange between the sites. Both trends can be observed in the measurements shown in Fig. 4.14. We can express the atom covariance as $\mathrm{Cov}(N_1, N_2) = (\sigma_+^2 - \sigma_-^2)/4$ and use Eqn. 4.44 to extract the particle exchange rates from the measurement of the sum and difference variances, as will be explained in the following chapter.

# 5 Dynamics in a dissipative double-well

In the previous chapter we have established that the dynamics in the MOT, in particular the particle exchange between two sites of a double-well configuration, are governed by thermal activation and light-assisted collisions. In this chapter we will introduce basic aspects of reaction-rate theory, resulting in a description of the hopping rate as a function of the potential barrier height and temperature of the system. We will then discuss several techniques to measure the particle exchange rate, depending on the activation mechanism and particle number. For large atom numbers, we can create a strong imbalance, i. e. all atoms in one site of the double-well, and observe the initial population transfer to the empty site. For small atom numbers, which we can easily resolve at a single-particle level, there are two methods of extracting the hopping rate. One involves the observation of anti-correlated atom number changes, e. g. $(N_1, N_2) \rightarrow (N_1 + 1, N_2 - 1)$, which are interpreted as hopping events. The other method relies on measuring the fluorescence noise from which the hopping rate can also be extracted. Combining these methods, our rate measurement range spans five orders of magnitude. We will describe the measured particle exchange rates with a multi-tailed atomic velocity distribution, caused by the different dynamics in the system. Finally, the effect of alternately pulsing between MOT and light sheet potential on the hopping rates are discussed.

## 5.1 Reaction-rate theory

Let us consider a chemical reaction with an activation energy $E_\mathrm{a}$. It can be modelled by a potential, similar to the one depicted in Fig. 5.1(a) with a potential barrier of height $E_\mathrm{a}$. Once the activation energy is overcome, the reactant transforms into the product. The beginnings of reaction-rate theory in physical chemistry date back to 1889, when Svante Arrhenius presented an empirical temperature dependence of the reaction rate $r$ given by the Arrhenius equation

$$r = Ae^{-E_\mathrm{a}/k_\mathrm{B}T}, \tag{5.1}$$

where $A$ is a constant rate pre-factor and $T$ the temperature of the system [90]. Taking the natural logarithm, Eqn. 5.1 can be rewritten as

$$\log(r) = \frac{-E_\mathrm{a}}{k_\mathrm{B}} T^{-1} + \log(A). \tag{5.2}$$

Representing the measurement in an *Arrhenius plot*, i. e. plotting $\log(r)$ against the inverse temperature $T^{-1}$, results in a straight line, from which we can determine $E_\mathrm{a}$ as the slope and $A$ as the offset. A modified Arrhenius equation reads

$$r = A \left(\frac{T}{T_0}\right)^n e^{-E_\mathrm{a}/k_\mathrm{B}T}, \tag{5.3}$$

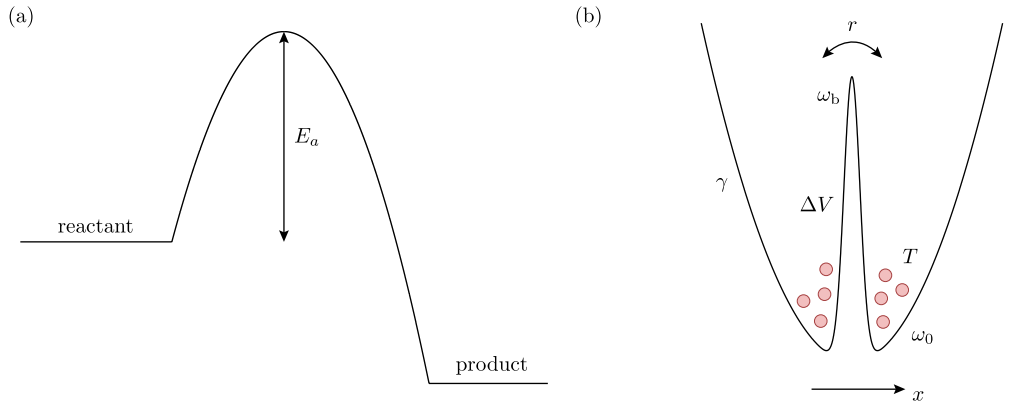


Figure 5.1: Typical potentials in reaction rate theory. (a) In chemical reactions the transition from reactant to product has to overcome an activation energy $E_a$. (b) Typical double-well potential in which one can study the particle hopping rate $r$ between the sites, separated by a potential barrier of height $\Delta V$. The atoms, having a temperature $T$ and experiencing a frictional constant $\gamma$, are located mainly at the potential minima, where the trapping frequency is $\omega_0$. The (anti-)trapping frequency at the peak of the barrier is $\omega_b$.

where $T_0$ is a temperature scale and the exponent $n$, taking into account a (slow) variation of the rate pre-factor with the temperature, typically takes values $-1 < n < 1$.

More than 45 years later, a refined understanding of the activation energy and the pre-factor of the reaction rate was given in the transition state theory (TST), developed by Henry Eyring, as well as Meredith Gwynne Evans and Michael Polanyi, in which one can express the reaction rate as

$$r = \frac{k_B T}{h} e^{-\Delta G / k_B T}, \tag{5.4}$$

where $h$ is Planck's constant and $\Delta G$ the Gibbs free energy [91]. At first it looks like a linear dependence of the pre-factor on the temperature, however, the Gibbs free energy itself depends on $T$. Eqn. 5.4 can be rewritten as an Arrhenius equation with $n < 1$. Two conditions in TST are on the one hand thermodynamic equilibrium at all times and on the other hand, that once a particle has crossed the activation barrier, the reaction is accomplished.

In 1940, Hendrik Anthony Kramers extended TST to a system with moderate-to-strong friction [92], leading to a description of overcoming a reaction barrier for a thermal sample with Brownian motion. Let us consider a one-dimensional double-well potential $V(x)$, like the one shown in Fig. 5.1(b), with reaction coordinate $x$ and a barrier height of $\Delta V$. The system is in thermal equilibrium with temperature T and exerts a linear friction force $-\gamma m \frac{\mathrm{d}x}{\mathrm{d}t}$, where $\gamma$ is the friction constant and $m$ the particle mass. Brownian motion, in our case the random walk due to photon scattering, is modelled by Gaussian random fluctuations $f(t)$ with zero mean, i. e. $\langle f(t) \rangle = 0$. The average can be taken over many observations of the same particle or simultaneously over a number of particles, given that their interaction can be neglected. The fluctuations $f(t)$ have a strong

temporal variation and obey the fluctuation-dissipation relation $\langle f(t)f(t')\rangle = 2m\gamma k_\mathrm{B}T\delta(t-t')$. The $\delta$-distribution resembles the Markov property of instantaneous dissipation, meaning that each photon scattering event is instantaneous and that the scattering events are uncorrelated [93]. This leads to a Newton equation of motion in form of the Langevin equation

$$m\frac{\mathrm{d}^2x}{\mathrm{d}t^2} = -\frac{\mathrm{d}V(x)}{\mathrm{d}x} - \gamma m\frac{\mathrm{d}x}{\mathrm{d}t} + f(t). \tag{5.5}$$

Kramers considered the time evolution of the probability density $p(x,\dot{x},t)$, expressed in a Fokker-Planck equation, and calculated the flux over the barrier to find a description of the reaction rate pre-factor in the moderate-to-strong friction regime [48]. The Kramers rate reads

$$r_\mathrm{K} = \frac{1}{\omega_\mathrm{b}}\left(\sqrt{\frac{\gamma^2}{4}+\omega_\mathrm{b}^2} - \frac{\gamma}{2}\right)\frac{\omega_0}{2\pi}e^{-\Delta V/k_\mathrm{B}T}, \tag{5.6}$$

where $\omega_0$ is the trapping frequency in the potential minima and $\omega_\mathrm{b}$ is the (anti-)trapping frequency at the position of the potential barrier. In the Smoluchowski limit of strong (over-damped) friction, i. e. $\gamma \gg \omega_\mathrm{b}$, the reaction rate reduces to

$$r_\mathrm{K} = \frac{\omega_\mathrm{b}}{\gamma}\frac{\omega_0}{2\pi}e^{-\Delta V/k_\mathrm{B}T}. \tag{5.7}$$

In the strong friction limit, one can consider a random walk for the reaction coordinate, in which the path may cross the barrier, but return to the initial site, contradicting the second TST condition. In this regime, one speaks of a *spatial-diffusion-controlled rate* as opposed to the *energy-diffusion-controlled rate* in the low friction limit. The Kramers rate can be seen as an extension of the TST result $r_\mathrm{TST} = \frac{\omega_0}{2\pi}\exp(-\Delta V/k_\mathrm{B}T)$ with a correction factor $\kappa \equiv r_\mathrm{K}/r_\mathrm{TST} = \omega_\mathrm{b}/\gamma$. Calculations of reaction rate constants always include the activation energy as a lower bound. Kramers correction of the constant *lowers* the rate, such that the increased effective activation energy is closer to the true value.

There are limitations to the concept of a simple activation energy, when the microscopic details of the reactant, in particular interaction between the particles, are involved. Under near-collisional conditions, molecular reaction dynamics dominate the system. Collision theory, proposed by Max Trautz in 1916 and William Lewis in 1918, states that only a fraction of the occurring collisions lead to enough energy of the reactant to overcome the activation energy [94]. Increasing the density of the sample leads to a higher number of trials and therefore more *successful* collisions. The reaction rate can be expressed as

$$r_\mathrm{CT} = Z\rho e^{-E_\mathrm{a}/k_\mathrm{B}T}, \tag{5.8}$$

where the collision frequency $Z = n\sigma v$ depends on the molecular density $n$, the reaction cross section $\sigma$ and the mean particle velocity $v$. The steric factor $\rho$ is the ratio of successful collisions to the total number of collisions.

In Section 4.3 we have seen that the trapping frequencies $\omega_0$ and $\omega_\mathrm{b}$ both depend on the potential barrier height $\Delta V$. Figure 5.2(a) shows a comparison of the reaction rate results from TST and the Kramers expression in the strong and moderate-to-strong friction regimes for different barrier heights. Comparing the inverse Arrhenius factor $k_\mathrm{B}T/\Delta V$ for a MOT temperature of 80 µK to the friction strength $\gamma/\omega_\mathrm{b}$ in our system, as shown in Fig. 5.2(b), we see that we are indeed in the *spatial-diffusion-controlled rate* regime at moderate-to-strong friction.

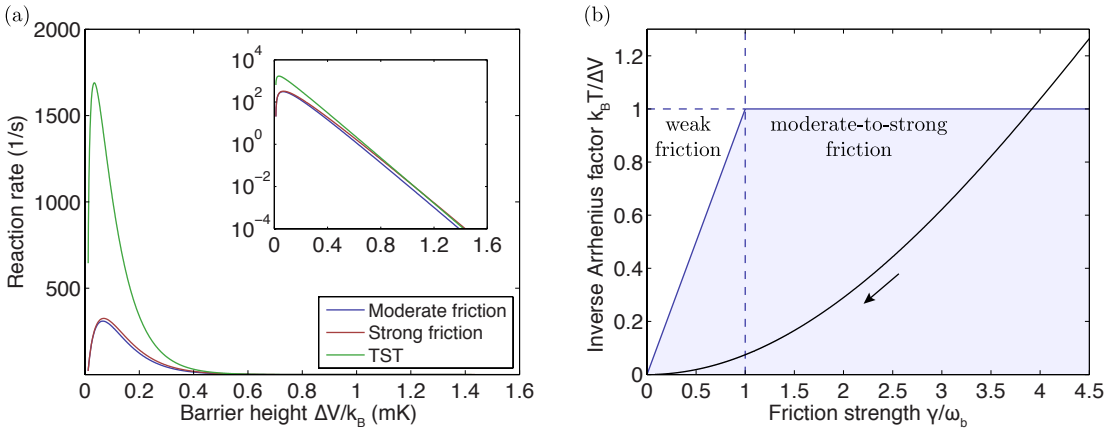


Figure 5.2: Reaction rate comparison and validity of Kramers' description. (a) The Kramers correction to the reaction rate coefficient leads to a reduced rate compared to the TST result. All three expressions show a similar behaviour in the exponential tail (inset). (b) The solid line shows the prevailing regime for a system temperature of 80 µK. The arrow indicates increasing barrier heights. For large enough $\Delta V$ the friction strength becomes smaller than unity, however due to the low temperature we are still in the moderate-to-strong friction regime, where the Kramers rate description is valid.

## 5.2 Rate measurement

We investigate several methods of rate measurement, depending on the underlying reaction process and the atom number regime. In order to simplify the analysis, we assume the particle exchange rates to be symmetric and define the exchange parameters $\tau_{\text{ex}} \equiv \tau_{12} \approx \tau_{21}$ and $\beta_{\text{ex}} \equiv \beta_{12} \approx \beta_{21}$. Likewise, we define the decay parameters $\tau \equiv \tau_1 \approx \tau_2$ and $\beta \equiv \beta_1 \approx \beta_2$. The atom number dynamics are then given by

$$\dot{N}_1 = -\frac{N_1}{\tau} - \frac{N_1}{\tau_{\text{ex}}} + \frac{N_2}{\tau_{\text{ex}}} - \beta N_1^2 - \beta_{\text{ex}} N_1^2 + \beta_{\text{ex}} N_2^2 \tag{5.9}$$

and

$$\dot{N}_2 = -\frac{N_2}{\tau} - \frac{N_2}{\tau_{\text{ex}}} + \frac{N_1}{\tau_{\text{ex}}} - \beta N_2^2 - \beta_{\text{ex}} N_2^2 + \beta_{\text{ex}} N_1^2, \tag{5.10}$$

as well as

$$\dot{N}_+ = \dot{N}_1 + \dot{N}_2 = -\frac{N_1 + N_2}{\tau} - \beta(N_1^2 + N_2^2). \tag{5.11}$$

### 5.2.1 Initial imbalance

In order to measure the rate of hopping due to light-assisted collisions, we initially set an atom number imbalance $N_1 \gg N_2$ by switching off the light-sheet, displacing the MOT with a vertical magnetic offset field, turning the light-sheet back on and reverting the MOT displacement. The last step defines $t = 0$, at which all atoms (typically a few thousand) are in site 1 and none in site 2.

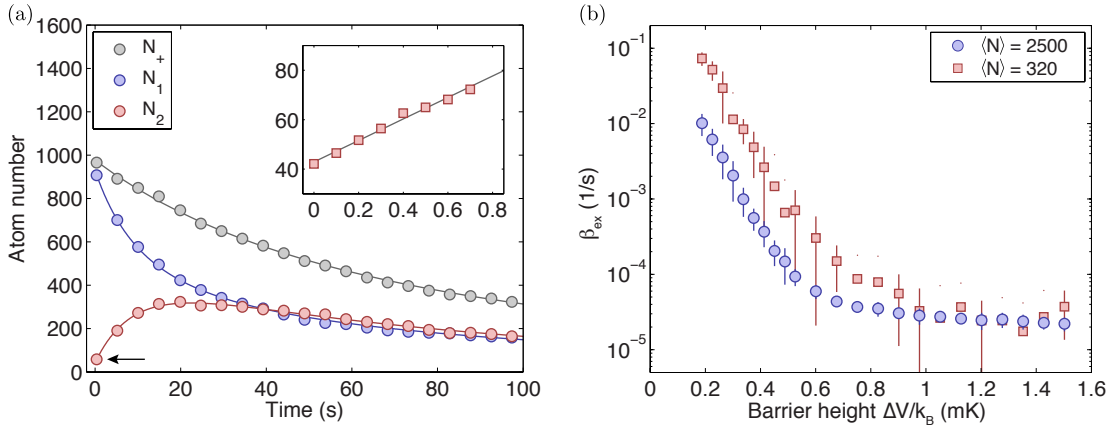


Figure 5.3: Measurement of the collisional hopping rate. (a) A large initial atom imbalance equilibrates over time. We analyse the rate of atom number increase in the initially scarcely populated site. The measurement indicated by the arrow consists in fact of 8 time steps, from which we extract the slope (inset). (b) The collisional hopping parameter $\beta_{\mathrm{ex}}$ reaches a value on the order of $10^{-5}$ at large barrier heights, where it does not depend on the atom number.

We observe the time evolution of the individual atom numbers, exemplarily shown in Fig. 5.3(a), which, for $N_1 \gg N_2$ and hence $N_1^2 \gg N_2^2$, is given by $\dot{N}_1 = -(\beta + \beta_{\mathrm{ex}})N_1^2$ and $\dot{N}_2 = \beta_{\mathrm{ex}} N_1^2$. Taking an image right after the atomic imbalance has been created, we can extract

$$\beta_{\mathrm{ex}} = \frac{1}{N_1^2}\frac{\Delta N_2}{\Delta t}, \tag{5.12}$$

where $\Delta N_2$ is the atom number increase in site 2 between two exposures and $\Delta t$ is the integration time. Here $N_1$ is the mean atom number in site 1 during $\Delta t$. We repeat the measurement for an initial imbalance towards site 2, i. e. $N_2 \gg N_1$ and $N_2^2 \gg N_1^2$, and extract $\beta_{\mathrm{ex}}$ from the atom number increase in site 1, given by $\dot{N}_1 = \beta_{\mathrm{ex}} N_2^2$.

The collisional hopping parameter $\beta_{\mathrm{ex}}$ is shown in Figure 5.3(b) as a function of the potential barrier height $\Delta V$ for two mean total atom numbers. At large barrier heights it reaches a value of about $2.5 \times 10^{-5}$, independent of the atom number.[1] This value is close to the fit parameter describing particle exchange due to light-assisted collisions in the noise model presented in Section 4.4. For smaller barrier heights we observe an exponential dependence of $\beta_{\mathrm{ex}}$ on $\Delta V$, as well as an atom number dependence. This indicates that the underlying exchange mechanism must be something else than two-body collisions.

[1] For some measurements at the lower atom number the error bar is larger than the value, and thus the lower bound cannot be displayed on a logarithmic scale. For the larger atom number this it not the case.

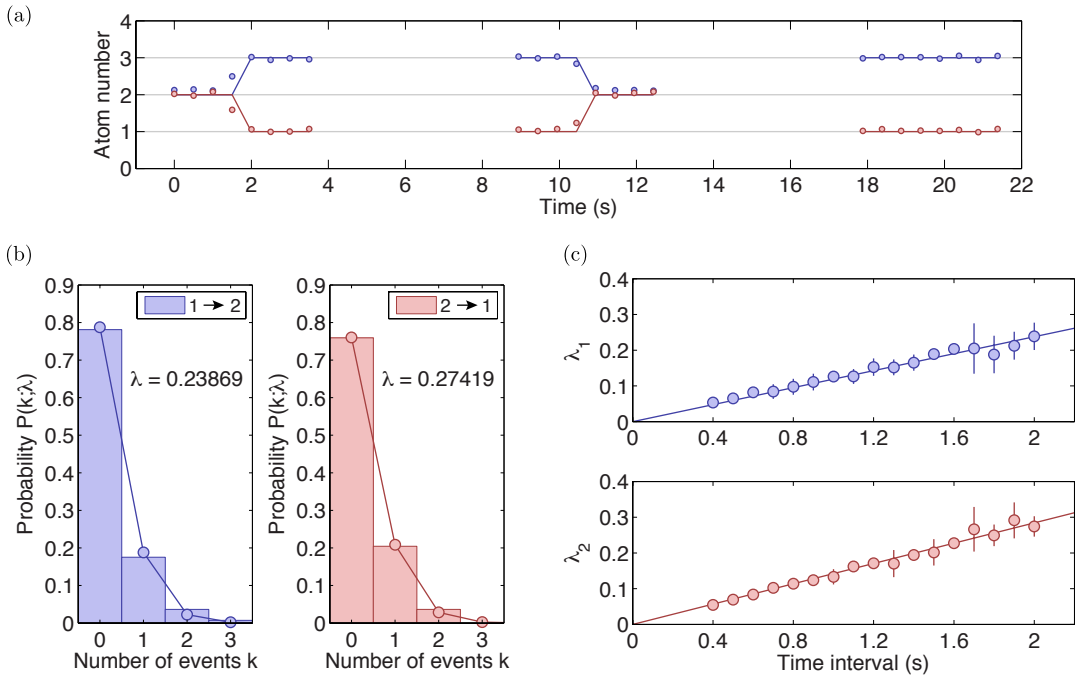


Figure 5.4: Extraction of the exchange rate from the number of Poisson distributed hopping events. (a) A step finding algorithm is employed to trace the atom numbers $N_1$ (blue) and $N_2$ (red) and detect hopping events, i. e. anti-correlated atom number changes. (b) The normalised occurrences of the number of hopping events in a given time interval (histogram) obey the Poisson distribution (circles). (c) The mean of the Poisson distribution increases linearly with the length of the time interval in which the hopping events are counted.

### 5.2.2 Step detection

For very small atoms numbers we can neglect the influence of light-assisted collisions, which is confirmed in the data by the lack of two-atom hopping events, and consider the exchange dynamics as a one-body effect. We employ a step finding algorithm to trace the atomic signal and extract the exact atom numbers $N_1$ and $N_2$ in each frame. The algorithm is based on an adaptive maximum-likelihood analysis of the fluorescence signal, given initial estimates of the experimental parameters, including lifetime and the number of counts per atom. As time progresses, the Bayesian algorithm finds new estimates of these parameters and is thereby able to give the best estimate for the atom number at each point in time. An example of this is shown in Fig. 5.4(a). If we neglect decay events, by post-selecting for $\dot{N}_+ = 0$, the dynamics are governed by

$$\dot{N}_1 = -\frac{N_1 - N_2}{\tau_{\mathrm{ex}}} \tag{5.13}$$

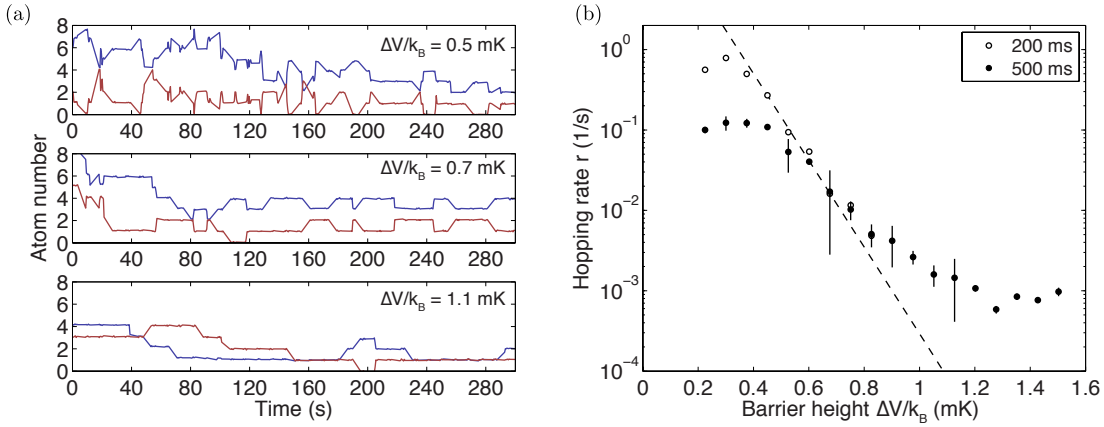


Figure 5.5: Few particle hopping rate for different potential barrier heights. (a) Example signal traces of $N_1$ (blue) and $N_2$ (red) for increasing barrier heights from top to bottom. (b) Hopping rate for a mean atom number of 3.7 and two different exposure times. The long exposure time is favourable for low rates, because it reduces the contribution of fluorescence noise. For small barrier heights, the long exposure time averages of many hopping events and underestimates the exchange rate. Here the shorter exposure time leads to a rate that is closer to the expected exponential dependence at a temperature of 80 µK (dashed line).

and

$$\dot{N}_2 = -\frac{N_2 - N_1}{\tau_{\mathrm{ex}}}. \tag{5.14}$$

We see that $\dot{N}_1 = -\dot{N}_2$ and while the rate equation is an average property of the system, the same equation holds for individual hopping events, which we count as an anti-correlated atom number change from one exposure to the next, all in one frame-transferred image. We do not include atom number changes between two images, since we do not have information about the atom numbers during the read-out process. Figure 5.4(b) shows an example measurement of the normalised occurrence of the number of hopping events $k$ in a time interval of 2 s at a barrier height of 0.6 mK. Here the exposure time was 100 ms. The data is well described by a Poisson distribution $P(k;\lambda)$, from which we can extract the mean number of hopping events $\lambda = \langle N \rangle T/\tau_{\mathrm{ex}}$. Increasing the observation time interval $T$, we find a linear increase of $\lambda$, as shown in Fig. 5.4(c). With a mean atom number of $\langle N \rangle = 5.51$, the extracted mean slope of $\lambda/T = 0.1305(64)\,\mathrm{s}^{-1}$ corresponds to a hopping rate of $r \equiv \tau_{\mathrm{ex}}^{-1} = \lambda/\langle N \rangle T = 0.0237(12)\,\mathrm{s}^{-1}$.

We measure the few particle hopping rate for different potential barrier heights $\Delta V$. An example measurement, shown in Fig. 5.5(a), illustrates the basic feature, that the hopping rate goes down with increasing barrier height. From Eqn. 5.6 we would expect that the hopping rate decreases exponentially with the barrier height, at least for large $\Delta V$, where the change of the trapping frequencies is negligible. We can confirm this behaviour up to a barrier height of 0.8 mK, however, there is an experimental feature that needs to be addressed. For high rates a long exposure time is beneficial, since both fluorescence noise and photon shot noise are averaged

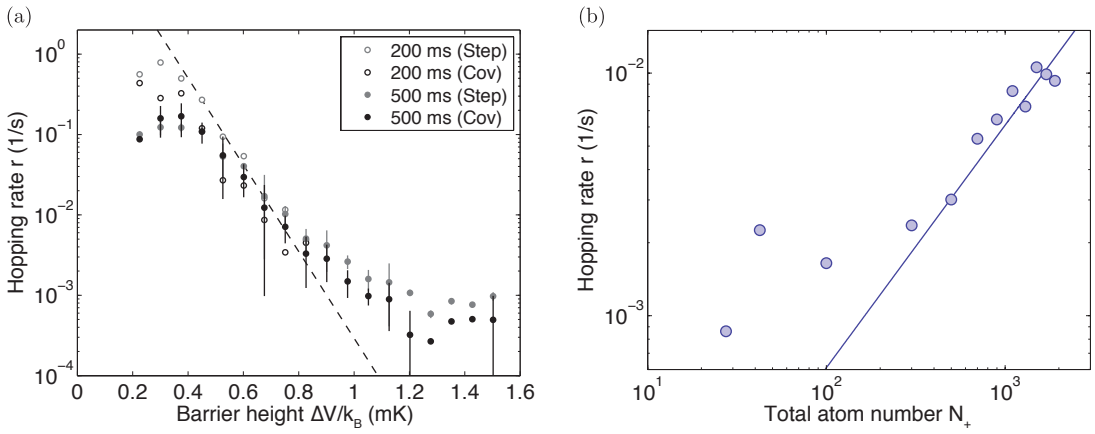


Figure 5.6: Hopping rate extraction from noise contribution. (a) Comparison of the two methods for extracting the few particle hopping rate. The method relying on the covariance analysis of the atom signal (black circles) agrees in all characteristic features with the results obtained via the step finding algorithm (grey circles), both for an exposure time of 200 ms (open circles) and 500 ms (filled circles). (b) The hopping rate shows a linear increase with large atom numbers, indicating collisional particle exchange, while the behaviour for small atoms numbers is consistent with thermal hopping.

down. In this regime we use an integration time of 500 ms. If the hopping dynamics (at low barrier heights) are too fast however, multiple hopping events occur during one long exposure time and the hopping rate is underestimated. Hence we measure the higher rates with a shorter exposure time of 200 ms as well and obtain a result which is closer to the Kramers rate expectation, as shown in Figure 5.5(b). At large potential barrier heights we observe a deviation from the expected exponential decrease of the hopping rate. At this point our resolution is limited by the total detection time, i. e. the experimentally available duration integrated over all exposures, not including the read-out time. We achieve a detection time of $t_{\mathrm{det}} = 3430\,\mathrm{s}$ for each datapoint and thus a resolution of $\sim t_{\mathrm{det}}^{-1} = 3 \times 10^{-4}\,\mathrm{s}^{-1}$, corresponding to one hopping event in about one hour. The effect of the hopping rate levelling off at $\sim 10^{-3}\,\mathrm{s}^{-1}$, apparently not explained by a limited detection time, will be discussed later in this chapter.

### 5.2.3 Noise contribution

As we have seen from Eqn. 4.44 derived in the previous chapter, we can express the covariance between atom numbers $N_1$ and $N_2$ in terms of the one- and two-body exchange parameters $\tau_{\mathrm{ex}}$ and $\beta_{\mathrm{ex}}$. At the same time, the covariance depends on the sum and difference variances $\sigma_+^2$ and $\sigma_-^2$, respectively. For very small atom numbers we can again neglect collisional hopping and the covariance reduces to

$$\mathrm{Cov}(N_1, N_2) = -\frac{N_1 + N_2}{2\tau_{\mathrm{ex}}} t = -\frac{N_+}{2\tau_{\mathrm{ex}}} t \tag{5.15}$$

and we can rewrite the hopping rate as

$$r \equiv \frac{1}{\tau_{\text{ex}}} = \frac{\sigma_-^2 - \sigma_+^2}{2\langle N \rangle t}, \tag{5.16}$$

where $\langle N \rangle$ is the mean total atom number during the measurement. We have previously seen that $\sigma_-^2 \geq \sigma_+^2$, so $r \geq 0$ is ensured. Eqn. 5.16 allows us to extract the hopping rate from the measurement of the signal variance, given our noise model. In Figure 5.6(a) we compare the results from such a measurement with the rate obtained via the step finding algorithm. The agreement extends to all characteristic features, such as the levelling off at higher potential barrier heights and the underestimation of high hopping rates.

In Section 4.4 we have analysed the difference and sum variances as a function of the atom number. If we extract from those measurements the hopping rate using Eqn. 5.16, we expect a constant thermal particle exchange rate for small atom numbers. For large atom numbers, however, the measurement shows a linear increase with the total particle number, as shown in Fig. 5.6(b), which indicates a density dependent effect, namely collisional hopping between the sites. Here the potential barrier height was $\Delta V / k_{\text{B}} = 1.4\,\text{mK}$.

## 5.3 Heavy-tailed velocity distribution

We have measured the hopping rate between the two sites of the double-well potential in different atom number regimes as a function of the barrier height and will now introduce a rate model, in an attempt to explain the observed features. As a simple criterion for a hopping event we require that the kinetic energy of a particle $E_{\text{kin}} = mv^2/2$ is equal to the potential barrier height $\Delta V$ (or higher). From this we obtain a critical velocity $v_{\text{c}} = \sqrt{2\Delta V/m}$. The hopping rate, expressed as the probability $P$ of having a thermal velocity larger than $v_{\text{c}}$ over a time period $t$, then reads

$$r = \frac{P}{t} = \frac{1}{t} \int_{v_{\text{c}}}^{\infty} f(v)\,\mathrm{d}v, \tag{5.17}$$

where $f(v)$ is the velocity distribution. Let us consider the Maxwell-Boltzmann distribution for the one-dimensional velocity $v$ of a thermal atomic sample

$$\mathcal{T}(v) = \sqrt{\frac{m}{2\pi k_{\text{B}} T}} \exp\left(-\frac{mv^2}{2k_{\text{B}}T}\right), \tag{5.18}$$

where $m$ is the atomic mass. Since the particle exchange between the sites happens along one direction, we have already used a one-dimensional description of the potential and we will restrict ourselves to the Maxwell-Boltzmann distribution for a single component of the velocity vector. Evaluating Eqn. 5.17 with $\mathcal{T}(v)$ as the velocity distribution leads to the exponential decrease of the hopping rate as a function of the barrier height, in accordance with Arrhenius' law, shown in Fig. 5.7 for a MOT temperature of $T = 80\,\mu\text{K}$, where $t^{-1}$, the intercept for $\Delta V \to 0$, is a free parameter and turns out to be $160(20)\,\text{s}^{-1}$. This corresponds to $t = 6\,\text{ms}$, which is on the same order as the time an atom needs to move through the MOT without light-sheet.

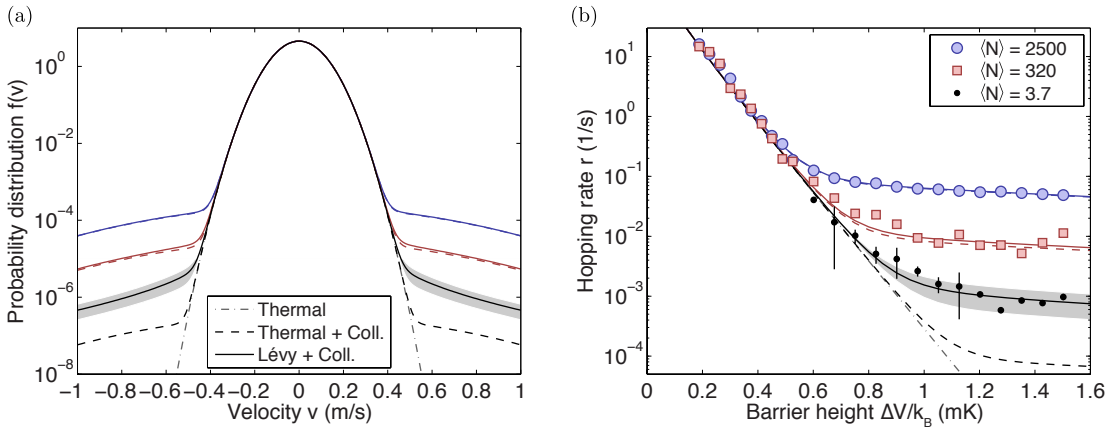


Figure 5.7: Heavy-tailed velocity distribution describing the hopping rates in various regimes. (a) In addition to the thermal distribution (dash-dotted line) we include an exponential energy distribution to account for light-assisted collisions at different atom numbers (dashed lines). The remaining one-body effects can be modelled by substituting the thermal distribution for the Lévy velocity distribution $\mathcal{L}_\alpha$ (solid lines). (b) The steep exponential decrease of the hopping rate at low barrier heights is well described by a thermal velocity distribution (dash-dotted line). At large barrier heights, the inclusion of light-assisted collisions explains the measured rates for large atom numbers (dashed lines), while small atom numbers require the inclusion of a non-Gaussian velocity distribution (solid lines). The shaded area indicates the uncertainty in the exponent $\alpha$.

In Section 3.3 we have established that the energy gained by the process of light-assisted collisions is exponentially distributed, which can be modelled by $\mathcal{C}(E) = E_0^{-1} \exp(-E/E_0)$ with an energy scale $E_0$ depending on the detuning of the light that excites the atoms into the S + P molecular potential. With this we can describe the deviation of the hopping rate from the thermal description at large barrier heights. An energy scale of $E_0/h = 60\,\mathrm{MHz}$ describes the weak, but significant dependence of the hopping rate due to light-assisted collisions on the potential barrier height, shown in Fig. 5.7(b), for mean atom numbers of 2500 and 320. We compare this to simulated values of $E_0/h \sim 30 - 50\,\mathrm{MHz}$ for $^{85}$Rb [95]. The exact value is not crucial, since the hopping rate in this regime is dominated by the tail of the exponential energy distribution, which is similar for all these values of $E_0$. In order to compare this energy scale to the thermal distribution, we can express $E_0$ as an effective temperature via $k_\mathrm{B}\tilde{T} = E_0$ and with $E = \frac{1}{2}mv^2$ obtain a velocity distribution for the light-assisted collisions

$$\mathcal{C}(v) = \sqrt{\frac{m}{2\pi k_\mathrm{B}\tilde{T}}} \exp\left(-\frac{mv^2}{2k_\mathrm{B}\tilde{T}}\right) \tag{5.19}$$

with $\tilde{T} = 3\,\mathrm{mK}$. The combined velocity distribution $f(v) = (1 - \varepsilon N)\mathcal{T}(v) + \varepsilon N \mathcal{C}(v)$, with an occupation of the high energy mode of $\varepsilon = 1.2(1) \times 10^{-7}$, describes the hopping rate measurements for large atom numbers $N$ over the entire range of barrier heights. However, we

measure an increased hopping rate for small atom numbers at large barrier heights, which is not described by collisional activation. Instead we shall generalise the thermal velocity distribution to a family of *stable* distributions, including heavy-tailed distributions for which the tail does not decrease exponentially, but according to a power law. As a consequence, these non-Gaussian distributions generally do not have a finite variance. Heavy-tailed momentum distributions are used to describe anomalous diffusion – sometimes called Lévy flight – in systems, typically out of thermal equilibrium, which exhibit rare but large fluctuations [96–100].

Any probability distribution can be expressed as the Fourier transform of a characteristic function $\varphi(t)$, given by

$$f(x) = \frac{1}{2\pi} \int_{-\infty}^{\infty} \varphi(t) e^{-ixt} \, \mathrm{d}t. \tag{5.20}$$

A distribution is called *Lévy alpha-stable* if the characteristic function can be written as [101]

$$\varphi(t) = \exp\left[it\mu - |ct|^{\alpha}(1 - i\beta \mathrm{sgn}(t)\Phi)\right], \tag{5.21}$$

where $\mathrm{sgn}(t)$ is the sign of $t$ and $\Phi = \tan(\pi\alpha/2)$ for $\alpha \neq 1$. For a skewness parameter $\beta = 0$, we obtain a symmetric alpha-stable distribution. We further set the shift parameter $\mu = 0$ and obtain the Lévy velocity distribution

$$\mathcal{L}_{\alpha}(v) = \frac{1}{2\pi} \int_{-\infty}^{\infty} \exp\left(-ivt - |ct|^{\alpha}\right) \, \mathrm{d}t, \tag{5.22}$$

where the scale parameter $c \in (0, \infty)$ measures the width of the distribution and $\alpha \in (0, 2]$ determines the asymptotic behaviour. In fact, $\mathcal{L}_{\alpha}(v) \sim 1/|v|^{\alpha+1}$ for $\alpha < 2$ [102]. For $\alpha = 2$ the Lévy stable distribution reduces to the normal distribution, i. e. $\mathcal{L}_2(v) \equiv \mathcal{T}(v)$, with a variance $\sigma^2 = 2c^2$. From this we identify $c = \sqrt{k_{\mathrm{B}}T/2m}$ and the parameter $t$ has the dimension of an inverse velocity.

Using the combined velocity distribution $f(v) = (1 - \varepsilon N)\mathcal{L}_{\alpha}(v) + \varepsilon N \mathcal{C}(v)$, we can finally describe all hopping rate measurements in the different regimes across four orders of magnitude, including for small atom numbers at large barrier heights, as shown in Fig. 5.7(b). We obtain a stability parameter $\alpha = 1.999\,90(5)$, which is only distinguishable from 2 due to the high measurement resolution of our detector.

We would also like to mention another velocity distribution, which has been used to describe anomalous transport in optical lattices [102, 103]. As a member of the family of Tsallis distributions, the so-called *q-Gaussian* is the q-analogue of the normal distribution and is given by [104]

$$\mathcal{P}_q(v) = Z_q^{-1} \left[1 - \tilde{\beta}(1-q)v^2\right]^{1/(1-q)}, \tag{5.23}$$

with normalisation parameter $Z_q$, scale parameter $\tilde{\beta} = m/2k_{\mathrm{B}}T$ and $1 < q < 3$. For $q \to 1$ the generalised q-Gaussian $\mathcal{P}_q(v)$ recovers the original normal distribution $\mathcal{T}(v)$. The asymptotic behaviour is given by $\mathcal{P}_q(v) \sim 1/v^{2/(q-1)}$ for $q \neq 1$ [103]. In an optical lattice, the index $q$ can be related to the potential depth $\Delta V$ via $q = 1 + 44E_{\mathrm{r}}/\Delta V$, where $E_{\mathrm{r}}$ is the recoil energy [102], hence $q \to 1$ for large potential barrier heights. However, from our measurements we expect instead a Gaussian behaviour ($q \sim 1$) at low barrier heights and non-Gaussian diffusion ($q > 1$)

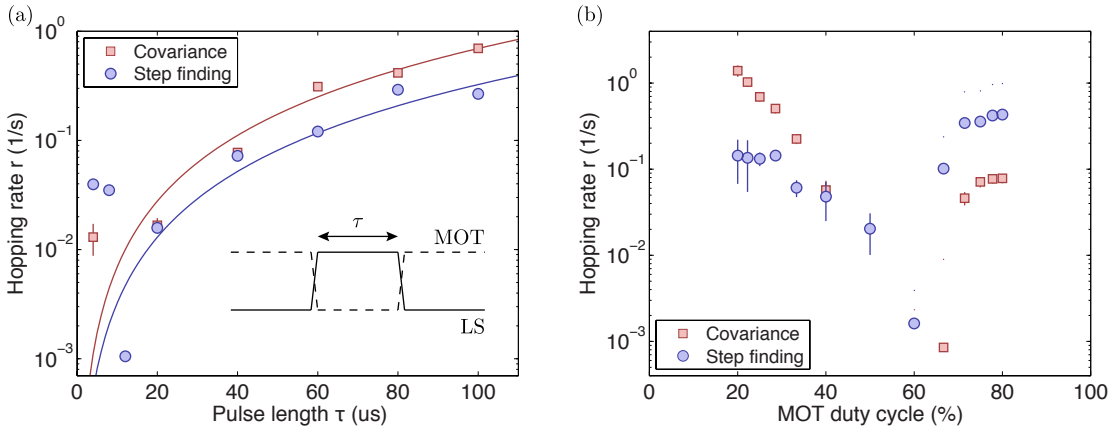


Figure 5.8: Measured hopping rates for varying pulsing of the light-sheet. (a) A longer pulse length $\tau$, equal for both the light-sheet and the MOT light, leads to an increased hopping rate, measured via the step finding algorithm, as well as extracted from the covariance analysis. We plot $r \propto \tau^2$ as a guide to the eye (blue line). We find an optimal pulse length of about $10\,\mu s$, while for shorter pulse lengths the hopping rate increases again. (b) Changing the pulse length of one component, while keeping the other one fixed, we find a minimal hopping rate for a MOT duty cycle around $60\%$.

at large barrier heights. Consequently, applying $\mathcal{P}_q(v)$ as a velocity distribution does not fit our measured hopping rates for any constant index $q$ or one that decreases with increasing barrier height.

Note that quantum tunnelling through the potential barrier would require the de Broglie wavelength $\lambda_{\mathrm{dB}} = h/p$ to be comparable to the width of the barrier [105], say $\sim 10^{-5}\,\mathrm{m}$. The particle momentum $p \sim \sqrt{m k_{\mathrm{B}} T}$ leads to an associated wavelength $\lambda_{\mathrm{dB}} \sim 10^{-8}\,\mathrm{m}$ for a MOT temperature of $80\,\mu\mathrm{K}$, thus tunnelling as a particle exchange mechanism between the sites can be neglected.

## 5.4 Effects of light-sheet pulsing and finite spatial extent

Our approach of generating a dissipative double-well potential intrinsically relies on the alternate pulsing between the potential barrier and the trapping light. For all measurements so far, we have used equal pulse lengths of $\tau = 4\,\mu s$ for the light-sheet and for the MOT, where we understand $\tau$ to be the time interval during which one of the light sources is on. Here we investigate the effect of the light-sheet pulsing on the hopping rate. For this we choose a barrier height of $\Delta V/k_{\mathrm{B}} = 0.9\,\mathrm{mK}$. First we vary the pulse length in an equal manner for both light-sheet and MOT light, shown in Fig. 5.8(a), to find a quadratic increase of the hopping rate for $\tau \gtrsim 20\,\mathrm{ms}$. Below an optimal pulse length of about $10\,\mu s$, where the hopping rate is minimal, we observe an increase of the rate.

We also vary the MOT duty cycle, by keeping the MOT pulse length $\tau_{\mathrm{MOT}}$ at $4\,\mu s$ and changing the light-sheet pulse length $\tau_{\mathrm{LS}}$ between $6\,\mu s$ and $16\,\mu s$ or keeping $\tau_{\mathrm{LS}} = 4\,\mu s$ and changing $\tau_{\mathrm{MOT}}$ from $6\,\mu s$ to $16\,\mu s$. Figure 5.8(b) shows an optimal duty cycle of about $60\%$. If the light-sheet

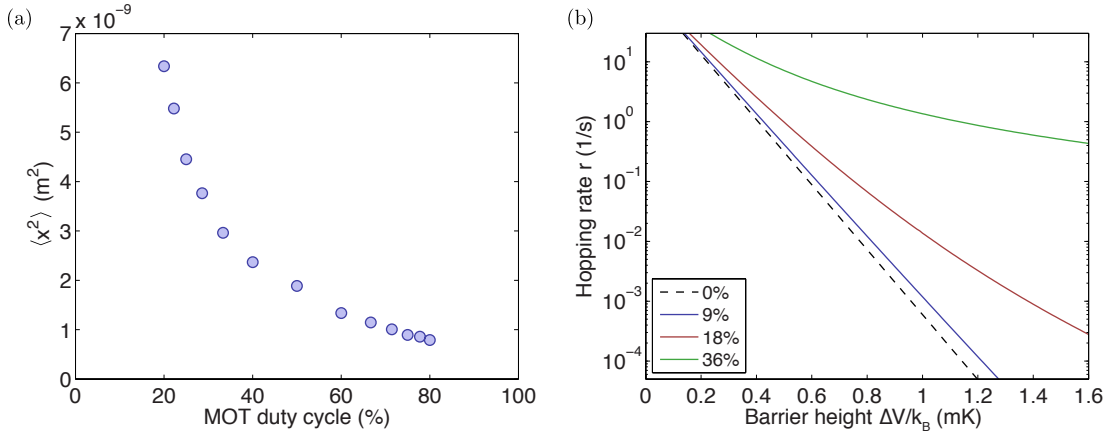


Figure 5.9: (a) MOT size $\langle x^2 \rangle$ as a function of the MOT duty cycle. We measure the width of the Gaussian atomic density distribution and interpret the increased size as a higher temperature, as long as $k_\mathrm{B}T = \kappa\langle x^2 \rangle$ holds. (b) The finite spatial extent of the light-sheet results in a reduced effective barrier height, which increases the hopping rate. The magnitude of the effect is shown for different ratios $\sigma/w_2$.

duration is reduced too much, the atoms see a lower average barrier height which increases the probability of crossing the barrier. If, on the other hand, the MOT light period is too short, laser cooling is not efficient and the hotter atoms have again a higher probability of crossing the barrier. We see indications for the latter effect in the increased MOT size $\langle x^2 \rangle$ for short MOT duty cycles[2], which indicates a higher temperature, given $T = \kappa\langle x^2 \rangle / k_\mathrm{B}$ (see Fig. 5.9(a)).

We have chosen the waist $w_2$ of the light-sheet to be much larger than the waist $\sigma$ of the atomic density distribution in order to prevent atoms from passing *around* the potential barrier. However, since the spatial extent of the light-sheet is finite, there is a certain probability, that an atom will travel far enough from the center of the MOT, where it experiences a reduced barrier height. We have calculated analytically how the smaller effective barrier influences the hopping rate by taking into account the full three-dimensional Gaussian profile of the light-sheet with spot sizes $w_1$ and $w_2$, as well as the Rayleigh length $z_\mathrm{R}$ along the $k$-vector. Figure 5.9(b) shows calculations for different ratios $\sigma/w_2$. For an infinitely small MOT we recover the simple exponential decay of the hopping rate with the barrier height, given by Arrhenius' law. In reality, the ratio is about $10\%$, in which case we observe a small increase of the hopping rate. Much bigger MOT sizes would be required in order to see a strong increase of the hopping rate, which may be able to explain the levelling off for small atom numbers at large barrier height, as described in the previous section. Even then, however, the effect would also be visible at smaller barrier heights, which we do not see in our measurements.

[2]For this measurement the light-sheet was turned off.

# 6 Stochastic resonance

The term *stochastic resonance* describes the signal-to-noise optimisation of a non-linear system's response by introducing additional noise. The requirements for this to occur are an activation barrier or threshold, a weak periodic input and a noise source intrinsic to the system. A dissipative double-well potential is a paradigm example of such a system. The potential barrier acts as the threshold for atoms hopping from one site to the other, while control over the temperature allows one to change the thermal noise level. Hence, by applying a weak periodic modulation to the potential, we expect the emergence of a stochastic resonance, where the response signal is the density distribution of the atoms.

We consider a heavily damped particle in a dissipative symmetric double-well potential $V(x)$. In Section 5.1 we have seen that in the strong-friction regime the Kramers rate of hopping between the two sites of the potential is given by

$$r_{\mathrm{K}} = \frac{\omega_0 \omega_{\mathrm{b}}}{2\pi\gamma} \exp\left(-\frac{\Delta V}{k_{\mathrm{B}} T}\right), \tag{6.1}$$

which depends exponentially on the temperature $T$. A weak periodic modulation with frequency $\Omega$ results in an asymmetric tilt of the potential, illustrated in Fig. 6.1. We assume the modulation to be too weak to introduce hopping, however, by varying the temperature, the noise-induced hopping rate $r_{\mathrm{K}}$ can be synchronised with it, meaning that the average waiting time $T_{\mathrm{K}} = r_{\mathrm{K}}^{-1}$ between two hopping events is comparable to half the driving period $T_\Omega = 2\pi/\Omega$. This leads to the *time-scale matching condition* $2T_{\mathrm{K}} = T_\Omega$ or equivalently $\Omega = \pi r_{\mathrm{K}}$.

If we denote the periodic driving of the system as $A(t) = A_0 \cos(\Omega t)$, the Brownian motion of the particle is described by

$$m\ddot{x} = -\gamma m\dot{x} - V'(x) + mA_0 \cos(\Omega t) + \sqrt{2m\gamma k_{\mathrm{B}} T}\,\xi(t), \tag{6.2}$$

where $\xi(t)$ denotes zero-mean, Gaussian white noise with the property $\langle \xi(t)\xi(t')\rangle = \delta(t-t')$ (compare to $f(t)$ in Eqn. 5.5). If the driving is absent ($A_0 = 0$), the particle will experience a random motion with $\langle x(t)\rangle_0 = 0$ and a statistical variance $\langle x^2\rangle_0$ which depends on the temperature. A periodic driving breaks the reflection symmetry of the system and $\langle x(t)\rangle$ does no longer vanish. We can reduce the information in $x(t)$ to merely being either in site 1 (left) or in site 2 (right) of the double-well. This leads to a two-state model based on a master equation for the probabilities $n_1$ and $n_2$ of being in either site, with the normalisation $n_1 + n_2 = 1$. The master equation, proposed by McNamara and Wiesenfeld [106], reads

$$\dot{n}_1(t) = -T_{12}(t) n_1 + T_{21}(t) n_2, \tag{6.3}$$
$$\dot{n}_2(t) = -T_{21}(t) n_2 + T_{12}(t) n_1, \tag{6.4}$$

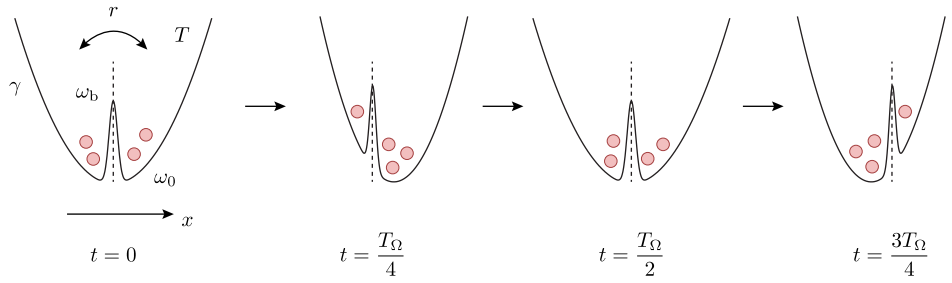


Figure 6.1: Periodic driving of the double-well potential. The atoms are equally populating both sites of the potential at $t = 0$. A periodic modulation with frequency $\Omega$ of the potential leads to an increased probability of hopping from left to right after a time $t = T_\Omega/4$ and vice versa at $t = 3T_\Omega/4$. The temperature $T$ of the atoms can be used to tune the hopping rate $r$, matching it to the driving frequency in order to observe the stochastic resonance effect.

with the Arrhenius type periodic transition rates

$$T_{12}(t) = r_\mathrm{K} \exp\left[\frac{A_0 x_0}{k_\mathrm{B} T} \cos(\Omega t)\right], \tag{6.5}$$

$$T_{21}(t) = r_\mathrm{K} \exp\left[-\frac{A_0 x_0}{k_\mathrm{B} T} \cos(\Omega t)\right], \tag{6.6}$$

where $\pm x_0$ are the positions of the potential minima, with $\langle x^2 \rangle_0 = x_0^2$ in the two-state approximation [107].

Choosing initial conditions $x_0 = x(t_0)$, one can take the average over many noise realisations for $x(t)$ to obtain $\langle x(t)|x_0, t_0\rangle$. In the asymptotic limit $t_0 \to -\infty$ this expression is independent of the initial conditions and becomes a periodic function $\langle x(t)\rangle_\mathrm{as} = \langle x(t + T_\Omega)\rangle_\mathrm{as}$. For small amplitudes, $A_0 x_0 \ll k_\mathrm{B} T$, the system response can be expressed as $\langle x(t)\rangle_\mathrm{as} = \bar{x}\cos(\Omega t - \phi)$ with amplitude

$$\bar{x}(T) = \frac{A_0 \langle x^2 \rangle_0}{k_\mathrm{B} T} \frac{2 r_\mathrm{K}}{\sqrt{4 r_\mathrm{K}^2 + \Omega^2}} \tag{6.7}$$

and phase lag

$$\phi(T) = \arctan\left(\frac{\Omega}{2 r_\mathrm{K}}\right). \tag{6.8}$$

For small temperatures, the amplitude $\bar{x}$ rises with $T$, due to the exponential increase of the hopping rate $r_\mathrm{K}$. For large temperatures, the $T^{-1}$ dependence of the amplitude dominates, which leads to a decreasing $\bar{x}$ with the noise intensity. In between, at the optimal noise level, we have a maximum of $\bar{x}$, i. e. the stochastic resonance effect. The phase lag transitions from $\pi/2$ at low noise intensity to 0 at high noise intensity and reaches a value of $\phi = 1$, when the time-scale matching condition $\Omega = \pi r_\mathrm{K}$ is fulfilled [52, 106, 108].

In this chapter we will discuss a scheme of temperature control, that relies on periodically switching the detuning of the laser cooling light. We will obtain the power spectral density of the system response and extract from it the linear response amplitude and phase, demonstrating the stochastic resonance of the signal-to-noise ratio. Furthermore, the spectrum reveals the non-linear character of the system. Finally, we investigate the effect of stochastic resonance for collisional dynamics, where the hopping rate tuning is not given by a change in the temperature, but by a modulation of the atomic density.

## 6.1 Tuning the hopping rate via temperature control

Magneto-optically trapped atoms exhibit complicated dynamics, due to the random scattering events during the position dependent laser cooling. Nevertheless, we can pretend that the atoms are in thermal equilibrium and attribute a temperature to the ensemble. The velocity distribution can be approximated by a Maxwell-Boltzmann probability density function (PDF)

$$f(v) = \sqrt{\left(\frac{m}{2\pi k_\mathrm{B} T}\right)^3} 4\pi v^2 \exp\left(-\frac{m v^2}{2 k_\mathrm{B} T}\right), \tag{6.9}$$

where the temperature $T$ depends on the detuning of the laser cooling light. In the Doppler cooling limit a detuning of $\delta = -\Gamma/2$ yields the lowest temperature of $T_\mathrm{D} \sim 150\,\mu\mathrm{K}$. Due to the effect of polarisation gradient cooling we expect a detuning further into the red to result in a lower temperature, thus we choose $\delta = -\Gamma$. It is possible to increase the temperature by switching to a blue detuning of $+\Gamma$, thereby heating the sample, for a short amount of time $\tau_\mathrm{b}$ compared to the period of red detuning $\tau_\mathrm{r}$. The total period is $\tau_\mathrm{b} + \tau_\mathrm{r}$, after which the process is repeated, as illustrated in the inset of Fig. 6.2. We choose a total period of $100\,\mu\mathrm{s}$, corresponding to a switching frequency of $10\,\mathrm{kHz}$, and find a maximum of the duty cycle $D = \tau_\mathrm{b}/(\tau_\mathrm{b} + \tau_\mathrm{r})$ of about $25\%$ above which the MOT becomes unstable. We observe a considerable increase in the size of the atomic density distribution, which indicates a higher temperature.

The temperature can be measured by a release and recapture method, in which an initial number of atoms $N_0$ is prepared and the laser beams are turned off at $t = 0$. Each atom[1] undergoes free propagation with the thermal velocity it had at the instant of release. We vary the release time $t_\mathrm{r}$ before the trapping laser is turned on again and determine the final number $N$ of recaptured atoms. Assuming a fixed recapture radius $r_\mathrm{c}$, the release time can be translated into a corresponding thermal velocity $v = r_\mathrm{c}/t_\mathrm{r}$. The ratio $N/N_0$ as a function of the velocity $v$ yields the cumulative distribution function (CDF) of the Maxwell-Boltzmann distribution

$$F(v) = \mathrm{erf}\left(\frac{v}{\sqrt{2}a}\right) - \sqrt{\frac{2}{\pi}}\frac{v}{a}\exp\left(-\frac{v^2}{2a^2}\right) \tag{6.10}$$

with parameter $a = \sqrt{k_\mathrm{B} T/m}$. An example measurement for a duty cycle of $18\%$ is shown in Fig. 6.2(a). The softening of the measured CDF compared to the theoretical expectation could be due to spatial variations in the capture volume. The CDF fit yields a most probable velocity of $v_\mathrm{p} = \sqrt{2}a \sim 0.2\,\mathrm{m/s}$, corresponding to a temperature of $T \sim 200\,\mu\mathrm{K}$.

[1] We prepare an initial atom number of about 2000 instead of repeating the experiment many times for a single atom.

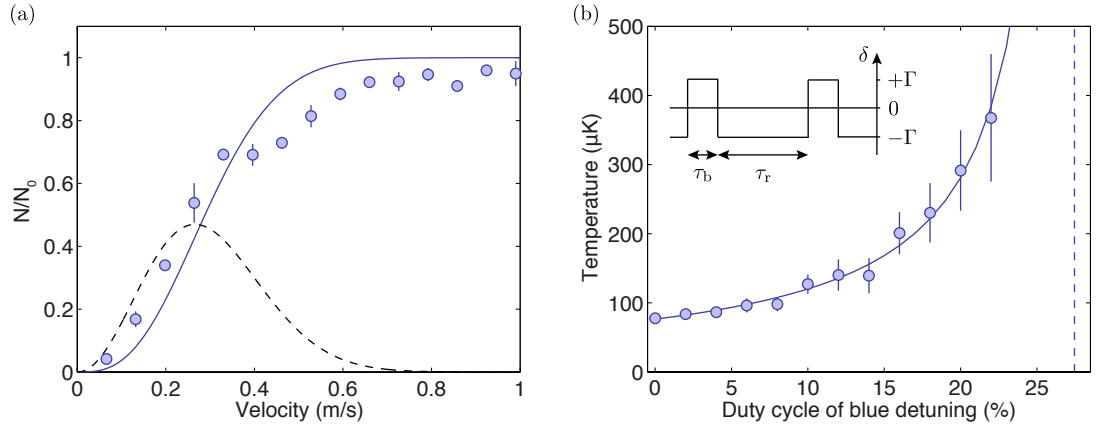


Figure 6.2: Temperature measurement and control. (a) The ratio of final and initial atom numbers $N/N_0$ in a release and recapture experiment for varying release times yields the CDF of the Maxwell-Boltzmann velocity distribution (blue solid line), shown here for a duty cycle of $18\%$. The derivative corresponds to the PDF, plotted here as an illustration with arbitrary amplitude (black dashed line). (b) The temperature of the ensemble can be controlled via the duty cycle of blue detuning, as illustrated in the inset. The model (solid line) predicts a divergence of the temperature at about $27\%$ (dashed line).

Increasing the duty cycle of blue detuning we observe an increase of the temperature, as shown in Fig. 6.2(b), and we model the dependence by considering the cooling and heating rates during the process. While the light is red detuned, the cooling rate is given by Eqn. 2.26. During the period of blue detuning there is heating with the same magnitude $\alpha v_x^2$. The heating rate due to isotropic emission of photons, given by Eqn. 2.27, is present the entire time. This adds up to a total balance of

$$\frac{D_p}{m} - (1-D)\alpha v_x^2 + D\alpha v_x^2 = 0, \tag{6.11}$$

with $D \in [0,1]$. Using the relation $v_x^2 = k_\mathrm{B}T/m$ we obtain

$$T = \frac{D_p}{\alpha k_\mathrm{B}(1-2D)}. \tag{6.12}$$

For $D \to 0$, this expression reduces to the Doppler temperature given in Eqn. 2.30. Furthermore, there is a pole at $D = 0.5$, where the temperature diverges. It is evident, that no stable condition can be achieved, if the blue detuned heating period is longer than the cooling time, i. e. the duty cycle surpasses $50\%$. Since we additionally have polarisation gradient cooling in our system, we modify Eqn. 6.12 and fit $T(D) = T_0(1-\xi D)^{-1}$ to our measurement of the temperature. Here the fit parameter $T_0$ represents the lowest possible temperature for $D = 0$, while $\xi$ quantifies how strong the temperature depends on the duty cycle. In this case the temperature diverges at $D = \xi^{-1}$. Choosing a recapture radius of $r_\mathrm{c} = 3.3\,\mathrm{mm}$ yields a minimum temperature of $T_0 = 76(4)\,\mu\mathrm{K}$, in accordance with earlier temperature measurement (see Section 3.3), and a

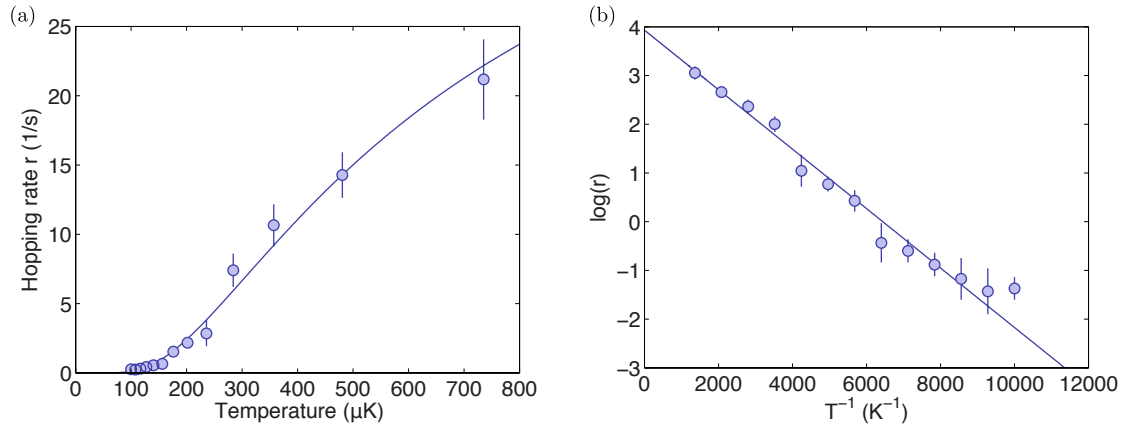


Figure 6.3: Hopping rate dependence on the temperature. (a) The hopping rate increases as a function of the temperature according to the Arrhenius equation. (b) The same measurement represented as an Arrhenius plot of the natural logarithm of the hopping rate versus the inverse temperature shows the expected linear dependence.

calibration parameter $\xi = 3.6(1)$. The latter is independent on $r_c$ and leads to a cut-off at a duty cycle of about $27\%$.

We can now measure the hopping rate for different duty cycles and analyse the dependence of the rate on the calibrated temperature. We choose a potential barrier height of $\Delta V/k_B = 0.64\,\mathrm{mK}$ and use the initial imbalance method for extracting the hopping rate (see Section 5.2)[2]. Fitting the Arrhenius equation $r = A\exp(E_a/k_B T)$, as shown in Fig. 6.3, sets a constraint on the activation energy $E_a$, which should correspond to the potential barrier height $\Delta V$. In order to satisfy this condition, we have to change our temperature calibration by setting $T_0 = 100\,\mu\mathrm{K}$. This yields a fit parameter $E_a/k_B = 0.61(6)\,\mathrm{mK}$. This calibration method does not depend on the knowledge of the MOT recapture radius $r_c$, which is difficult to obtain, however, it assumes a correct calibration of the potential barrier height. Here the pre-factor is $A = 51(8)\,\mathrm{s}^{-1}$, independent of the value chosen for $T_0$, which is smaller than in earlier measurements, possibly due to the different detuning of the MOT light.

## 6.2 Non-uniform power spectral density

Having established control over the hopping rate via adjusting the temperature of the atoms, we now turn to the modulation of the potential as a weak input signal. We periodically modulate the magnetic offset field perpendicular to the light-sheet with a driving frequency of $\Omega = 2\pi \cdot 0.2\,\mathrm{Hz}$, leading to a harmonic oscillation of the offset $\tilde{x} = \xi_0 \cos(\Omega t)$, which changes the static potential

[2]For the measurements in this chapter, the light-sheet detuning was changed to $\Delta = 2\pi \times 9\,\mathrm{GHz}$, resulting in a different potential barrier height calibration.

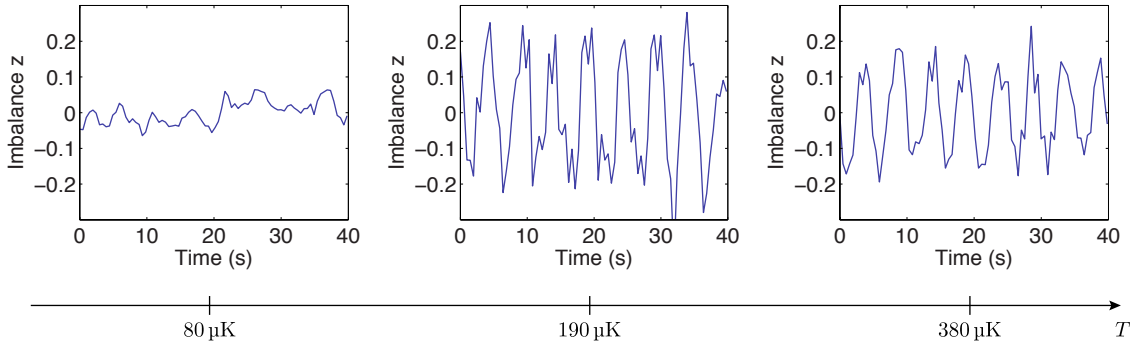


Figure 6.4: Example traces of the atom number imbalance $z$ for increasing temperatures. The driving frequency of $0.2\,\mathrm{Hz}$ can be clearly seen in the traces with improved signal-to-noise ratio.

$V(x) = m\omega^2 x^2/2 + V_{\mathrm{LS}}(x)$ into the time-dependent potential

$$\begin{aligned}\tilde{V}(x,t) &= \frac{1}{2}m\omega^2(x-\tilde{x})^2 + V_{\mathrm{LS}}(x) \\ &= V(x) + \frac{1}{2}m\omega^2\tilde{x}^2 - m\omega^2 x\tilde{x}. \end{aligned} \tag{6.13}$$

Taking the negative spatial derivative of this potential, we obtain

$$-\tilde{V}'(x,t) = -V'(x) + m\omega^2\xi_0\cos(\Omega t), \tag{6.14}$$

which we can compare to Eqn. 6.2 and identify $A_0 \equiv \omega^2\xi_0$, i. e. an increasing amplitude of the magnetic offset field oscillation leads to a linear increase in the parameter $A_0$.

The system response can be observed in the normalised atom number difference, which we define as the imbalance $z = (N_1 - N_2)/(N_1 + N_2)$. Figure 6.4 intuitively shows the stochastic resonance effect in a series of example signal traces, in which the amplitude of the output signal first increases and then decreases as a function of the temperature.

For a quantitative analysis of the stochastic resonance, we calculate the power spectral density (PSD) of the measured signal. In fact, slight variations of the CCD read-out time lead to irregularly spaced time samples $t_n$ for the discrete imbalances $z_n$, hence we perform a non-uniform discrete Fourier transform

$$\tilde{z}_k = \sum_{n=-N/2}^{N/2-1} z_n e^{-i2\pi\nu_k t_n}, \tag{6.15}$$

where $N$ is the total number of samples. Note that the frequency samples $\nu_k = k/N$ are uniformly distributed. Since the signal is real valued, the PSD is an even function and we consider only positive frequencies. The non-uniform power spectral density is given by

$$P_k = \frac{\langle t_n \rangle}{N}|\tilde{z}_k|^2, \tag{6.16}$$

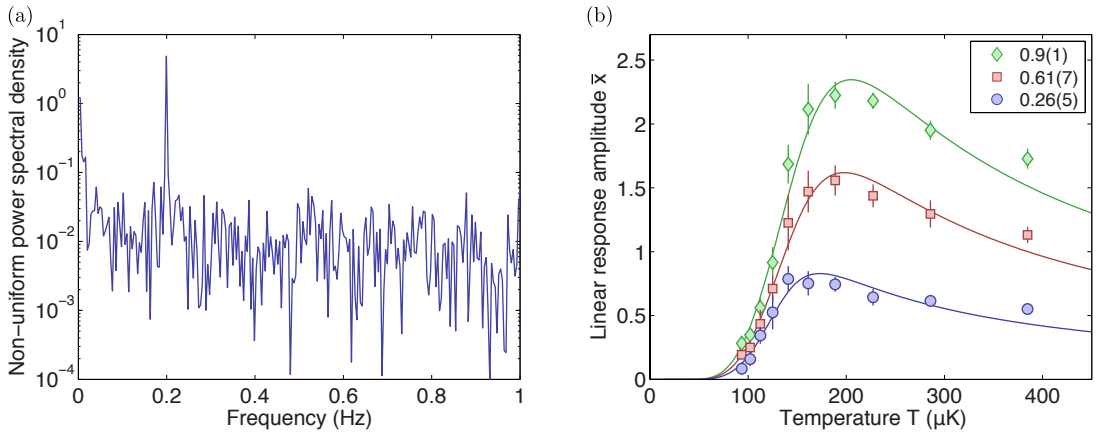


Figure 6.5: Amplitude extraction from the power spectral density. (a) An example of a non-uniform PSD, shown here for a temperature of $T = 190\,\mu\text{K}$, exhibits a strong peak at the driving frequency. (b) The amplitude of the periodic response, calculated from the peak strength in the non-uniform PSD, reveals the stochastic resonance behaviour as a function of temperature. Different driving amplitudes $\xi_0$ with a ratio of 1:2:3 lead to the extracted amplitudes $A_0 x_0/\Delta V$ stated in the legend. The barrier height for this measurement was $\Delta V/k_\text{B} = 0.64\,\text{mK}$.

where $\langle t_n \rangle = N^{-1} \sum_n t_n$ is the mean sampling time. Fig. 6.5(a) shows an example of such a non-linear PSD at a temperature of 190 μK and a driving amplitude of $A_0 x_0/\Delta V = 0.6$. A distinct peak at the driving frequency represents the linear response of the system.

## 6.3 Linear response amplitude and phase

The amplitude of the linear response $\bar{x}(T)$ can be related to the integrated power $p_1$ in the peak of the power spectral density at the driving frequency $\nu_0 = \Omega/2\pi$ via $2p_1 = \pi \bar{x}^2(T)$ [51, 109]. We integrate the non-linear PSD $P(\nu)$ in a narrow window of $\Delta\nu = 0.02\,\text{Hz}$ about the driving frequency $\nu_0$ and subtract the background power spectral density $P_\text{N}$ to obtain

$$p_1 = \int_{\nu_0 - \Delta\nu}^{\nu_0 + \Delta\nu} P(\nu) - P_\text{N}\,\text{d}\nu. \tag{6.17}$$

The extracted linear response amplitude $\bar{x}(T)$, shown in Fig. 6.5(b) for a potential barrier height of $\Delta V/k_\text{B} = 0.64\,\text{mK}$, first increases upon adding thermal noise, then decreases again after reaching a maximum at a temperature of about 200 μK. We repeat the experiment for twice and three times the driving amplitude and see an indication that the linear response amplitude increases linearly with the driving amplitude, i. e. $\bar{x}(T) \propto A_0$. Here we chose a temperature calibration parameter $T_0 = 80\,\mu\text{K}$, in order for the fit parameter $\Delta V$ entering the Kramer's rate $r_\text{K}$ in Eqn. 6.7 to comply with the given potential barrier height.

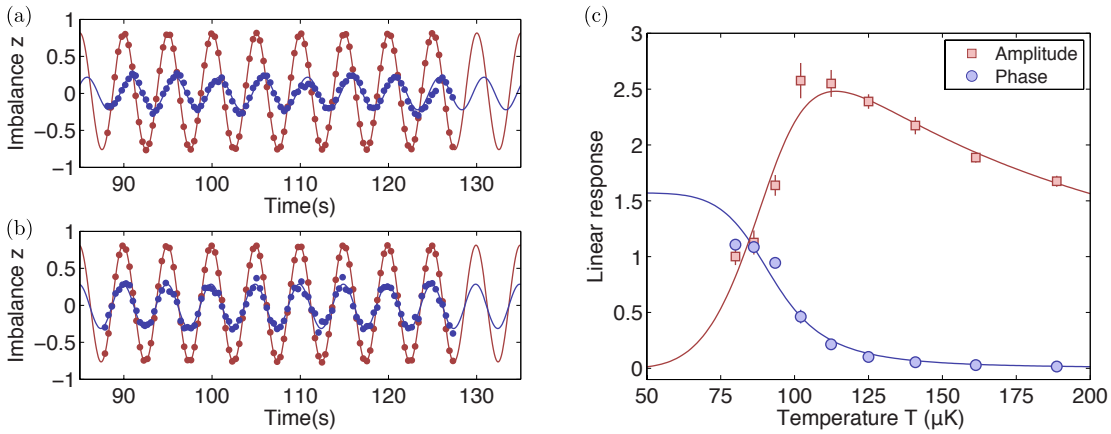


Figure 6.6: Measurement of the linear response phase. (a) A cosine fit to both the imbalance $z$ (blue dots) and input signal $B_z$ (red dots) reveals a phase lag close to $\pi/2$ at $T = 80\,\mu\text{K}$, i. e. below the stochastic resonance. (b) At $T = 190\,\mu\text{K}$, above the resonance, the phase lag is consistent with zero. (c) A fit to the linear response phase measurement (blue circles) shows good agreement in the experimentally accessible temperature regime. The linear response amplitude (red squares) reveals the resonance to be close to a temperature of $T = 110\,\mu\text{K}$, for $\Delta V/k_\text{B} = 0.64\,\text{mK}$ and $A_0 x_0/\Delta V = 1.5$.

The stochastic resonance effect can be interpreted as tuning the noise level in order to obtain a maximum of the signal-to-noise ratio [110–114], which can be defined as

$$\text{SNR} = 2\left[\lim_{\Delta\omega\to 0}\int_{\Omega-\Delta\omega}^{\Omega+\Delta\omega} P(\omega)\,\mathrm{d}\omega\right] \Big/ P_\text{N}(\Omega). \tag{6.18}$$

The factor of 2 in this definition reflects the symmetry property $P(\omega) = P(-\omega)$. In leading order the signal-to-noise ratio can be expressed as

$$\text{SNR} = \pi\left(\frac{A_0 x_0}{k_\text{B} T}\right)^2 r_\text{K}, \tag{6.19}$$

which does not depend on the driving frequency $\Omega$ [106, 112, 115, 116]. Like the linear response amplitude, the signal-to-noise ratio exhibits a maximum as a function of the system temperature. Although the optimal noise levels in both cases are similar, they do not necessarily coincide.

The phase of the linear response can be obtained in two ways. We record the signal $B_z$ from a function generator, which controls the current for the magnetic offset field modulation, as the input signal to the atomic system, here with an average atom number of about one hundred. First we fit a cosine to multiple oscillations of each the imbalance $z$ and the input signal $B_z$, as shown in Fig. 6.6(a-b), to obtain the phase difference. Alternatively, we can compute the phase lag as the phase angle difference of the non-uniform Fourier transform of both input and response signal. Both phase extraction methods yield the same result, the latter being shown in Fig. 6.6(c). While the phase lag $\phi$ is zero for temperatures above the resonance, as predicted from Eqn. 6.8,

it approaches $\pi/2$ below the resonance[3]. Since the coldest temperature we can achieve is the intrinsic MOT temperature, we cannot reach the limit of $\phi = \pi/2$ in this experiment.

## 6.4 Non-linear response

A typical consequence of having a non-linear system, like the threshold realised by the potential barrier, are higher harmonics of the driving frequency, manifested in higher order frequency components in the power spectral density. In particular, for a periodically driven *symmetric* system, odd higher frequencies $\omega_n = (2n+1)\Omega$ are expected. This can be understood by considering the expansion of an ideal square wave

$$S(t) = \frac{4}{\pi}\left(\sin(\Omega t) + \frac{1}{3}\sin(3\Omega t) + \frac{1}{5}\sin(5\Omega) + ...\right), \tag{6.20}$$

with an infinite number of odd higher harmonics. Taking the expansion only up to the first higher order ($n = 1$), leads to slight rectification of the linear response ($n = 0$), which is exactly what the threshold behaviour of the potential barrier induces. If for some reason, however, the system is to some extent *asymmetric*, also even higher harmonics can be expected. Note that higher harmonics in the PSD do *not* correspond to actual hopping timescales, since there is no periodic particle exchange on a timescale faster than $r = \Omega/\pi$. There can be a *slower* timescale, when the particle hop skips one driving period, however, these events do not lead to peaks in the PSD, because of statistical averaging.

The peak strength of the frequency components in the PSD is known to decay with $A_0^{2n}$ [107]. Hence, in an attempt to measure non-linear effects in our system, we increase the driving amplitude up to $A_0 x_0/\Delta V = 4.5$, for a constant potential barrier height of $\Delta V/k_\mathrm{B} = 0.64\,\mathrm{mK}$ and a temperature of $T = 190\,\mu\mathrm{K}$, where the stochastic resonance yields the best signal-to-noise ratio. First, we confirm that the the linear response amplitude $\bar{x}$ scales linearly with $A_0$ over a wide range of driving amplitudes, as shown in Fig. 6.7(a). Calculating the peak strength $p_3$ by integrating the non-uniform PSD in a narrow frequency window about $3\nu_0$, analogous to Eqn. 6.17, we observe an increase beyond a driving amplitude of $A_0 x_0/\Delta V \sim 3$. However, we perform the same measurement without the light-sheet barrier and also see an increasing peak strength $p_3$ for large driving amplitudes (see Fig. 6.7(b)). This artefact can be explained with a saturation of the imbalance $z$. For example, if all atoms are located in the $N_1$ region of interest, the imbalance analysis will yield $z = 1$, even though the atomic cloud might still perform a harmonic motion. This technical issue leads to a rectification of the output signal, which shows up in the power spectral density. In order to avoid this effect, we calculate the centroid of the atomic density distribution and investigate its non-linear PSD. The centroid $c$ is obtained by summing the pixel values $I_{xy}$ inside both regions of interest along the direction $x$ of the light-sheet separation in order to obtain the sum profile $I_y = \sum_x I_{xy}$. The centroid is the weighted average along the perpendicular direction $y$ given by

$$c = \frac{\sum_y y \cdot I_y}{\sum_y I_y}. \tag{6.21}$$

[3] A time lag between the CCD trigger and the time stamp registered by the experimental control leads to a phase offset of $\phi_0 = -0.06(1)$, which we correct for.

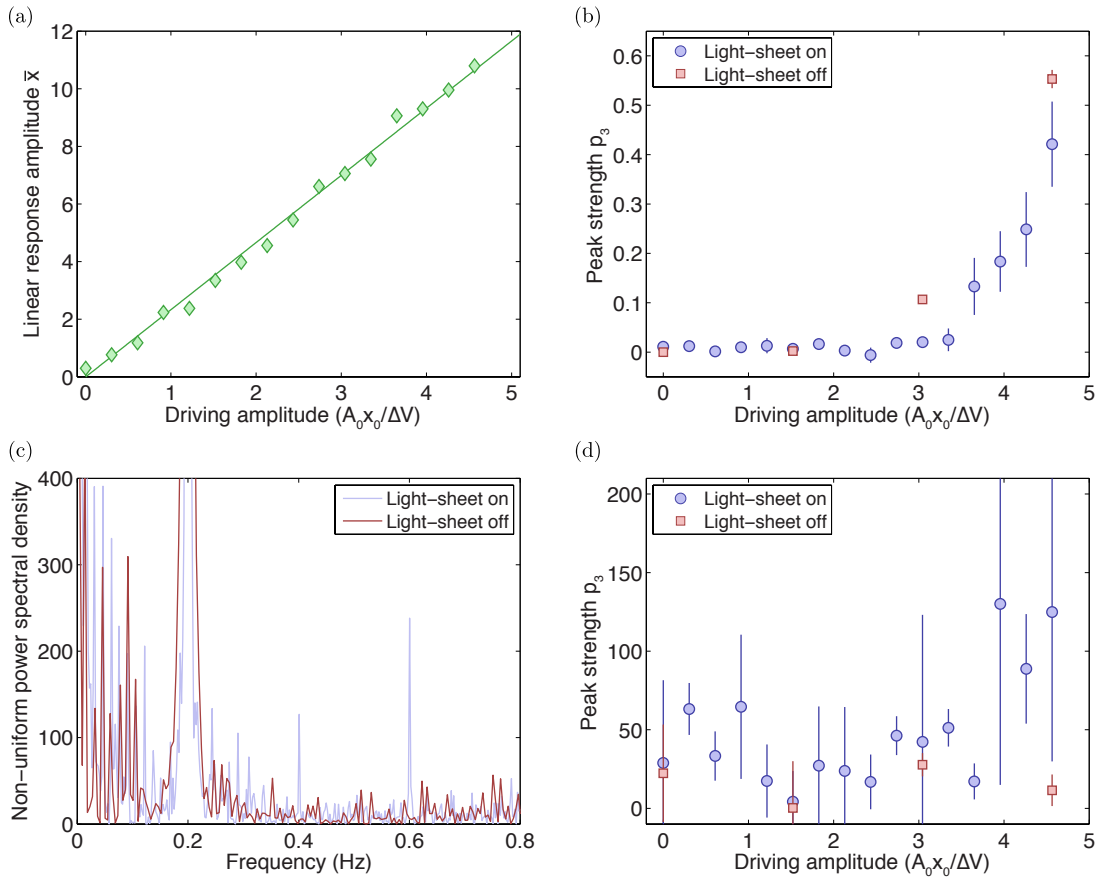


Figure 6.7: Indications of non-linear scaling. (a) The linear response amplitude $\bar{x}$, obtained from the peak strength $p_1$ at the driving frequency $\nu_0$, increases linearly with the driving amplitude $A_0$, as predicted by Eqn. 6.7. (b) For the imbalance analysis, the integrated peak strength at $3\nu_0$ shows an increase at large driving amplitudes (blue circles), however this artefact is also present, when the barrier is absent (red squares). (c) For a driving amplitude of $A_0 x_0/\Delta V = 4.5$, the non-uniform PSD of the centroid analysis reveals higher frequency components at $2\nu_0$ and $3\nu_0$ (blue line), which are not detected when the light-sheet is switched off (red line). (d) For the centroid analysis, we observe a slight increase of the peak strength $p_3$ above $A_0 x_0/\Delta V \sim 3$ (blue circles), which is not detected without the barrier (red squares). Note that the peak strength in general is much greater than for the imbalance evaluation method.

Figure 6.7(c) shows the non-uniform PSD of the centroid analysis. When the light-sheet is turned on, we observe a distinct peak at $3\nu_0$, indicating a non-linear behaviour of our system. This peak vanishes when the potential barrier is absent, which indicates that it is not arising from a technical issue of the analysis method. We also observe a peak at $2\nu_0$, an indication of asymmetry in the system, which can be explained by slightly different hopping rates $r_{12}$ and $r_{21}$ between sites 1 and 2, possibly due to different well depths. The peak strength $p_3$ for the centroid analysis increases as a function of the driving amplitude $A_0$, as shown in Fig. 6.7(d). At the largest driving amplitude the peak strength measured without the light-sheet is at least an order of magnitude smaller and consistent with the background noise level. However, concerning the peak strength $p_3$ with the potential barrier present, due to its apparently sudden increase above a driving amplitude of $A_0 x_0/\Delta V \sim 3$ and the large measurement scatter even at lower amplitudes, one has to be careful with the interpretation of the non-linear response being intrinsic to the system.

## 6.5 Implications of intra-well motion

For small driving amplitudes $A_0 x_0/\Delta V$, the behaviour of both amplitude and phase of the linear system response at small noise intensities, i. e. low temperatures $T$, are qualitatively altered due to intra-well dynamics [117, 118]. In a regime where inter-well dynamics dominate, the phase lag $\phi$ reaches a limit of $\pi/2$ for $T \to 0$, according to Eqn. 6.8. For small driving amplitudes, or equivalently large barrier heights, intra-well dynamics become relevant and the linear response phase is described by

$$\phi = \arctan\left(\frac{\Omega}{\omega_0} \cdot \frac{2\omega_0^2 r_\mathrm{K} + \Omega^2 D}{4\omega_0 r_\mathrm{K}^2 + \Omega^2 D}\right), \tag{6.22}$$

where the trapping frequency $\omega_0$ at the minima of the double-well potential describes the intra-well relaxation rate and $D \propto T$ is the noise intensity [119]. For large temperatures, i. e. $T \to \infty$, we recover Eqn. 6.8. In the limit of small temperatures, however, Eqn. 6.22 reduces to

$$\phi = \arctan\left(\frac{\Omega}{\omega_0}\right). \tag{6.23}$$

Since in our experiment $\omega_0 \gg \Omega$, the phase lag approaches zero in the limit of small noise intensities. For noise intensities in between there is a maximum of the linear response phase, however, the peak is not a fundamental feature of the stochastic resonance effect, but merely originates from a competition between intra- and inter-well dynamics [119–121]. Fig. 6.8(a) shows a measurement of the phase lag for a barrier height of $\Delta V/k_\mathrm{B} = 1.3\,\mathrm{mK}$, corresponding to a driving amplitude of $A_0 x_0/\Delta V = 0.75$. The linear response amplitude reveals a shift of the stochastic resonance to a temperature of about $200\,\mu\mathrm{K}$, compared to the $100\,\mu\mathrm{K}$ in a previous measurement for half the potential barrier height. The suppression of the inter-well motion due to the increased barrier height shifts the turnover of the phase lag to an accessible temperature regime, such that we can confirm that $\phi \to 0$ for $T \to 0$.

We turn our interest to the implications of the intra-well dynamics on the linear response amplitude. The spectral amplification $\eta = [\bar{x}(T)/A_0]^2$ is given by

$$\eta = D^{-2}\left[\frac{4r_\mathrm{K}^2}{4r_\mathrm{K}^2 + \Omega^2} + \frac{g^2\omega_0^2}{\omega_0^2 + \Omega^2} + \frac{4g\omega_0 r_\mathrm{K}(2\omega_0 r_\mathrm{K} + \Omega^2)}{(4r_\mathrm{K}^2 + \Omega^2)(\omega_0^2 + \Omega^2)}\right], \tag{6.24}$$

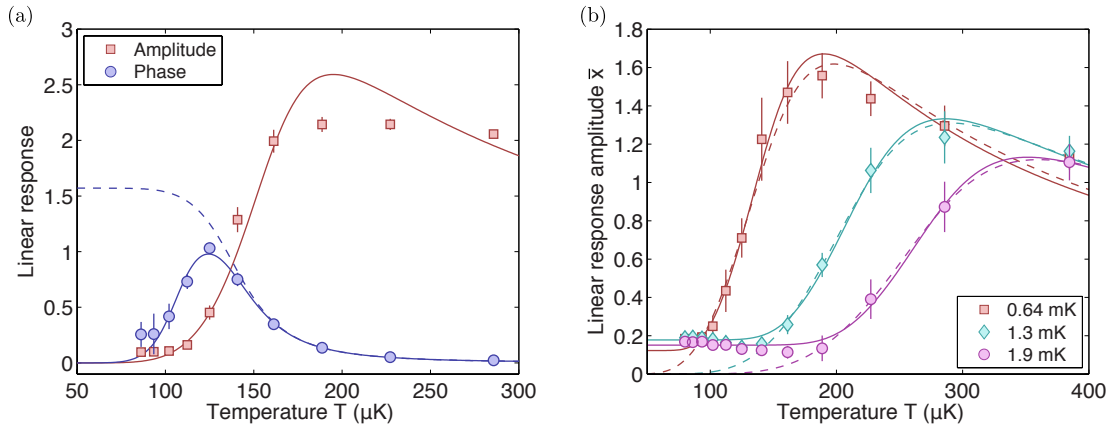


Figure 6.8: Impact of intra-well dynamics on the linear system response amplitude and phase. (a) For a barrier height of $\Delta V/k_\mathrm{B} = 1.3\,\mathrm{mK}$, the phase lag approaches zero at low temperatures, which is well described by taking into account intra-well dynamics (blue solid line). Neglecting this effect leads to a completely different behaviour (blue dashed line). (b) For large barrier heights, the values being stated in the legend, we observe deviations from the simple linear response theory given by Eqn. 6.7 (dashed lines). The data is correctly described by including intra-well dynamics (solid lines).

where the weight $g = D/\omega_0$ for $D \to 0$ [51, 122]. We can neglect the last term in the sum of Eqn. 6.24 and use the simplified expression to obtain the linear response amplitude

$$\bar{x}(T) = \frac{A_0\langle x^2\rangle_0}{k_\mathrm{B}T}\sqrt{\frac{4r_\mathrm{K}^2}{4r_\mathrm{K}^2+\Omega^2}+\frac{g^2\omega_0^2}{\omega_0^2+\Omega^2}}. \tag{6.25}$$

For large temperatures, this takes the form of Eqn. 6.7. On the other hand, for $T \to 0$, the linear response amplitude reduces to

$$\bar{x}(T) \propto \frac{A_0\langle x^2\rangle_0}{\sqrt{\omega_0^2+\Omega^2}}, \tag{6.26}$$

which is a finite constant, independent of the temperature. Experimentally, we set the barrier heights $\Delta V_1/k_\mathrm{B} = 0.64\,\mathrm{mK}$, $\Delta V_2/k_\mathrm{B} = 1.3\,\mathrm{mK}$ and $\Delta V_3/k_\mathrm{B} = 1.9\,\mathrm{mK}$, and measure the linear response amplitude, as shown in Fig. 6.8(b). For increased barrier heights, or equivalently smaller driving amplitudes $A_0x_0/\Delta V$, we observe the effect of intra-well dynamics. While the measured amplitude can be well described using Eqn. 6.7 for large temperatures, we see a clear deviation at low temperatures for the large barrier heights $\Delta V_2$ and $\Delta V_3$. Using Eqn. 6.25 to fit the data, correctly describes the behaviour in the limit of small noise intensities.

Intra-well dynamics alter the behaviour of the signal-to-noise ratio as well [119], which is then given by

$$\mathrm{SNR} = \pi\left(\frac{A_0x_0}{k_\mathrm{B}T}\right)^2\cdot\frac{\omega_0^2r_\mathrm{K}^2+\Omega^2D^2}{\omega_0^2r_\mathrm{K}+\Omega^2D}. \tag{6.27}$$

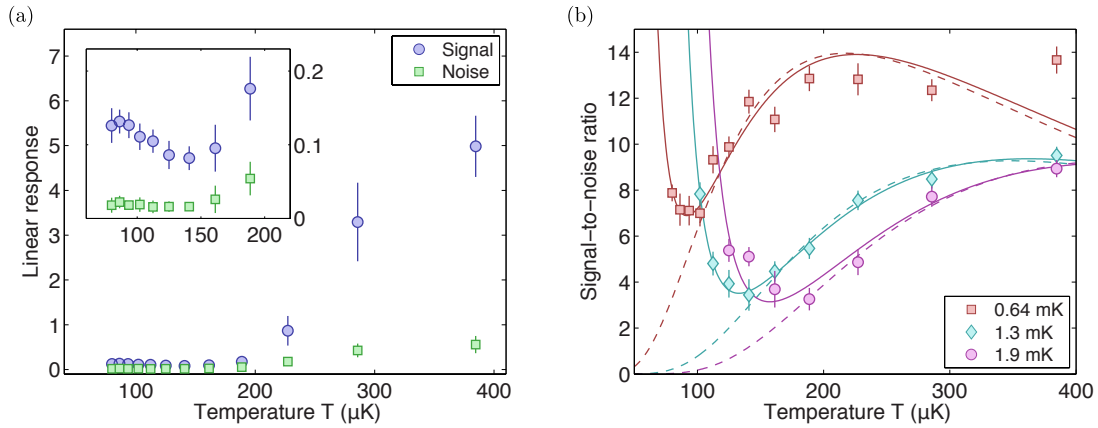


Figure 6.9: Impact of intra-well dynamics on the signal-to-noise ratio. (a) Due to the stochastic resonance effect, the linear response signal increases faster than the noise as a function of the temperature. While for small temperatures the signal tends to a constant value, the noise decreases monotonically, as shown in the inset, ultimately leading to a divergence of the signal-to-noise ratio. (b) We observe the divergence of the SNR at low temperatures due to intra-well motion (solid lines), measured for the different potential barrier heights stated in the legend. Simply applying Eqn. 6.19 does not match our observations (dashed lines).

For large noise intensities, i. e. $T \to \infty$, we recover Eqn. 6.19, for which the signal-to-noise ratio exhibits a maximum at the optimal noise intensity and would vanish for small temperatures. However, if we consider the limit of $T \to 0$, Eqn. 6.27 yields

$$\mathrm{SNR} = \pi \left( \frac{A_0 x_0}{k_\mathrm{B} T} \right)^2 D, \tag{6.28}$$

which diverges for small temperatures. We measure the linear response signal and noise individually, as shown in Fig. 6.9(a) for a potential barrier height of $\Delta V / k_\mathrm{B} = 1.9\,\mathrm{mK}$, and find that the signal increases faster than the noise as a function of the temperature, due to the stochastic resonance effect. In the limit $T \to 0$, the signal tends to a constant value due to intra-well motion, as we have seen earlier in the case of the linear response amplitude, while the noise is expected to decrease monotonically to zero. Experimentally, the noise levels off at a finite value, which may be explained by the limited resolution of the PSD, due to a restricted measurement time. As a consequence, we cannot use some of the data for slow temperatures and large barrier heights. Still we observe clearly the divergence of the signal-to-noise ratio for $T \to 0$, as described by Eqn. 6.27. Figure 6.9(b) shows the SNR for different potential barrier heights and how strongly it is affected by intra-well motion.

# 7 Conclusion

We have experimentally and theoretically investigated the limits of atom number detection with single-particle resolution in mesoscopic samples via fluorescence imaging. Following first observations of discrete equidistant peaks in the fluorescence histogram, we have developed a noise model which incorporates all relevant contributions in the form of photon shot noise, fluorescence noise and noise due to atom loss. The later can be derived from a master equation approach and shows how the detector performance depends on the lifetime $\tau$ of the magneto-optical trap and the rate of light-assisted collisions $\beta$. The noise model explains the scaling of the signal variance with the number of atoms in the ensemble. As reported in [56], we find for an optimal exposure time of $100\,\mathrm{ms}$ a single-particle resolution limit of 1080 atoms. This limit can be improved by correcting the signal for mean atoms loss, which is described by the parameters $\tau$ and $\beta$, increasing the maximum atom number for which single-particle resolution is achieved to 1200. As a result, the measurement fidelity for determining the exact particle number with this detector is larger than $98\%$ for atom numbers up to 100.

The scheme can be extended to a state-selective atom number detection by using radiation pressure to remove particles in one of the two internal hyperfine states. By measuring the total atom number before the experiment, in the end it is sufficient to know the population of only one state. With this technique we reach the single-particle resolution limit for 250 atoms and the state-selective single-atom measurement fidelity is $99.6\%$. Simultaneous state-selective detection can be achieved by splitting the MOT with a focused blue-detuned light-sheet posing a potential barrier between two sites in which the atom number is measured individually. While we have not shown the Stern-Gerlach splitting and recapturing sequence, we investigated in detail the particle detection in two spatially separated potential wells. In addition to loss from the trap, here we have to take into account particle exchange between the sites, both thermal and due to light-assisted collisions. This effect is an important source of noise in the detector performance. With a potential barrier height limited only by the available laser power, we reach the single-particle resolution limit for detecting the atom number difference at a total of 500 atoms in the ensemble. Due to the high energy scale of light-assisted collisions, increasing the barrier height does not lower the rate of collisional particle exchange as much as it does for the thermal hopping rate. The collisional hopping rate might rather be reduced, and thus the detector performance improved, by decreasing the atomic density or increasing the laser detuning.

We have analysed the dynamics in the dissipative double-well potential by varying the potential barrier height and using reaction-rate theory to describe the observed effects. While for sufficiently low barrier heights the rate scales according to Arrhenius' law, at large barrier heights, where thermal dynamics are frozen out, collisional dynamics dominate the particle exchange between the two sites. For single atoms and large barrier heights we observe an additional effect which renders the hopping rate much larger than would be expected from thermal exchange. This can be explained by the inclusion of a heavy-tailed velocity distribution, arising from laser cooling effects

beyond the polarisation gradient cooling theory (Lévy flights). Single-atom resolution allows the measurement of very rare events, down to one in $10^4$ seconds, spanning in total a measurement range of five orders of magnitude.

Finally, we have introduced and demonstrated the stochastic resonance effect in a driven dissipative double-well. We achieve good temperature control by switching to blue detuning of the laser cooling light, effectively heating the atomic sample for a short period of time during the cooling cycle. The temperature change directly carries forward to a variation of the hopping rate as described by Arrhenius' law. In matching the hopping rate to the frequency of an external drive, the signal-to-noise ratio of the weak linear response signal can be improved. We have shown the correct scaling of the linear response amplitude with the driving amplitude and measured the linear response phase lag. There are indications for a non-linearity system response, as would be expected from the threshold behaviour of the light-sheet. Furthermore, we observe the implications of intra-well motion, which alters the behaviour of both linear response amplitude and phase in the limit of small temperatures.

In summary, the magneto-optical trap is not only ideal for detecting mesoscopic atom numbers with single-particle resolution, but extended to a dissipative double-well potential it gives insights in reaction rates, important for many chemical systems, and effects such as the stochastic resonance, which can be found in a multitude of areas, including biology and medical science.

## Outlook

Having presented a detector with single-atom resolution for samples with more than one thousand particles, the focus is now on generating interesting quantum states with mesoscopic occupation. In the future, fluorescence imaging is to be combined with the production of Bose-Einstein condensates, where the spatial separation and subsequent retrapping of the individual hyperfine states is a challenge by itself. Such a system allows the creation of highly-entangled states via spin-changing collisions, leading to the ultimate limit of matter wave interferometry.

Another route is the investigation of multidimensional transport in controlled dissipative systems, which is difficult to calculate theoretically, but experimentally accessible as an extension of the one-dimensional double-well system presented in this thesis to a hybrid optical lattice.

# List of constants

The following table lists the constants and their abbreviations relevant for this thesis.

| Natural constants [123] | symbol | value |
|---|---|---|
| Planck constant | $h$ | $6.626\,069\,57(29) \times 10^{-34}\,\mathrm{J\,s}$ |
| Reduced Planck constant | $\hbar$ | $h/2\pi$ |
| Speed of light | $c$ | $299\,792\,458\,\mathrm{m\,s^{-1}}$ |
| Magnetic constant | $\mu_0$ | $4\pi \times 10^{-7}\,\mathrm{N\,A^{-2}}$ |
| Electric constant | $\varepsilon_0$ | $(\mu_0 c^2)^{-1} = 8.854\,187\,817\,\ldots \times 10^{-12}\,\mathrm{F\,m^{-1}}$ |
| Bohr magneton | $\mu_\mathrm{B}$ | $9.274\,009\,68(20) \times 10^{-24}\,\mathrm{J\,T^{-1}}$ |
| Bohr radius | $a_0$ | $5.291\,772\,109\,2(17) \times 10^{-11}\,\mathrm{m}$ |
| Boltzmann constant | $k_\mathrm{B}$ | $1.380\,648\,8(13) \times 10^{-23}\,\mathrm{J\,K^{-1}}$ |
| Rubidium 87 properties [124] | | |
| Atomic number | $Z$ | 37 |
| Atomic mass | $m$ | $1.443\,160\,648(72) \times 10^{-25}\,\mathrm{kg}$ |
| Melting point | $T_\mathrm{M}$ | 39.30 °C |
| Nuclear spin | $I$ | 3/2 |
| Rubidium 87 $\mathrm{D}_1$ line properties [124] | | |
| Transition frequency | $\omega_0$ | $2\pi \cdot 377.107\,463\,380(11)\,\mathrm{THz}$ |
| Wavelength | $\lambda$ | $794.978\,851\,156(23)\,\mathrm{nm}$ |
| Lifetime | $\tau$ | $27.679(27)\,\mathrm{ns}$ |
| Natural linewidth | $\Gamma$ | $2\pi \cdot 5.7500(56)\,\mathrm{MHz}$ |
| Recoil velocity | $v_\mathrm{r}$ | $5.7754\,\mathrm{mm\,s^{-1}}$ |
| Rubidium 87 $\mathrm{D}_2$ line properties [124] | | |
| Transition frequency | $\omega_0$ | $2\pi \cdot 384.230\,484\,468\,5(62)\,\mathrm{THz}$ |
| Wavelength | $\lambda$ | $780.241\,209\,686(13)\,\mathrm{nm}$ |
| Lifetime | $\tau$ | $26.2348(77)\,\mathrm{ns}$ |
| Natural linewidth | $\Gamma$ | $2\pi \cdot 6.0666(18)\,\mathrm{MHz}$ |
| Recoil velocity | $v_\mathrm{r}$ | $5.8845\,\mathrm{mm\,s^{-1}}$ |

# Bibliography


1. Chu, S. The manipulation of neutral particles. *Reviews of Modern Physics* **70,** 685–706 (1998).
2. Cohen-Tannoudji, C. N. Nobel Lecture: Manipulating atoms with photons. *Reviews of Modern Physics* **70,** 707–719 (1998).
3. Phillips, W. D. Nobel Lecture: Laser cooling and trapping of neutral atoms. *Reviews of Modern Physics* **70,** 721–741 (1998).
4. Hänsch, T. W. & Schawlow, A. L. Cooling of gases by laser radiation. *Optics Communications* **13,** 68–69 (1975).
5. Wineland, D. J. & Itano, W. M. Laser cooling of atoms. *Physical Review A* **20,** 1521–1540 (1979).
6. Chu, S, Hollberg, L, Bjorkholm, J. E., Cable, A & Ashkin, A. Three-dimensional viscous confinement and cooling of atoms by resonance radiation pressure. *Physical Review Letters* **55,** 48–51 (1985).
7. Chu, S, Bjorkholm, J. E., Ashkin, A & Cable, A. Experimental observation of optically trapped atoms. *Physical Review Letters* **57,** 314–317 (1986).
8. Raab, E. L., Prentiss, M, Cable, A., Chu, S. & Pritchard, D. E. Trapping of neutral sodium atoms with radiation pressure. *Physical Review Letters* **59,** 2631–2634 (1987).
9. Dalibard, J. & Cohen-Tannoudji, C. Laser cooling below the Doppler limit by polarization gradients: simple theoretical models. *JOSA B* **6,** 2023–2045 (1989).
10. Estève, J, Gross, C, Weller, A, Giovanazzi, S & Oberthaler, M. K. Squeezing and entanglement in a Bose–Einstein condensate. *Nature* **455,** 1216–1219 (2008).
11. Appel, J *et al.* Mesoscopic atomic entanglement for precision measurements beyond the standard quantum limit. *Proceedings of the National Academy of Sciences of the United States of America* **106,** 10960–10965 (2009).
12. Gross, C, Zibold, T, Nicklas, E, Estève, J & Oberthaler, M. K. Nonlinear atom interferometer surpasses classical precision limit. *Nature* **464,** 1165–1169 (2010).
13. Riedel, M. F. *et al.* Atom-chip-based generation of entanglement for quantum metrology. *Nature* **464,** 1170–1173 (2010).
14. Einstein, A, Podolsky, B & Rosen, N. Can Quantum-Mechanical Description of Physical Reality Be Considered Complete? *Physical Review* **47,** 777–780 (1935).
15. Bell, J. S. On the Einstein-Podolsky-Rosen paradox. *Physics* **1,** 195–200 (1964).
16. Bell, J. S. On the problem of hidden variables in quantum mechanics. *Reviews of Modern Physics* **38,** 447–452 (1966).

17. Aspect, A., Dalibard, J. & Roger, G. Experimental test of Bell's inequalities using time-varying analyzers. *Physical Review Letters* **49,** 1804–1807 (1982).

18. Weihs, G., Jennewein, T., Simon, C., Weinfurter, H. & Zeilinger, A. Violation of Bell's inequality under strict Einstein locality conditions. *Physical Review Letters* **81,** 5039–5043 (1998).

19. Rowe, M. *et al.* Experimental violation of a Bell's inequality with efficient detection. *Nature* **409,** 791–794 (2001).

20. Greenberger, D. M. Bell's theorem without inequalities. *American Journal of Physics* **58,** 1131 (1990).

21. Chen, Y.-A. *et al.* Heralded Generation of an Atomic NOON State. *Physical Review Letters* **104,** 043601 (2010).

22. Haas, F, Volz, J, Gehr, R, Reichel, J & Estève, J. Entangled States of More Than 40 Atoms in an Optical Fiber Cavity. *Science* **344,** 180–183 (2014).

23. Afek, I, Ambar, O & Silberberg, Y. High-NOON States by Mixing Quantum and Classical Light. *Science* **328,** 879–881 (2010).

24. Saunders, D. J., Jones, S. J., Wiseman, H. M. & Pryde, G. J. Experimental EPR-steering using Bell-local states. *Nature Physics* **6,** 845–849 (2010).

25. Gross, C *et al.* Atomic homodyne detection of continuous-variable entangled twin-atom states. *Nature* **480,** 219–223 (2011).

26. Hu, Z & Kimble, H. J. Observation of a single atom in a magneto-optical trap. *Optics letters* **19,** 1888–1890 (1994).

27. Willems, P. A., Boyd, R. A., Bliss, J. L. & Libbrecht, K. G. Stability of magneto-optical traps with large field gradients: Limits on the tight confinement of single atoms. *Physical Review Letters* **78,** 1660 (1997).

28. Gomer, V & Meschede, D. A single trapped atom: Light-matter interaction at the microscopic level. *Annalen der Physik* **10,** 9–18 (2001).

29. Haubrich, D *et al.* Observation of individual neutral atoms in magnetic and magneto-optical traps. *EPL (Europhysics Letters)* **34,** 663 (1996).

30. Nelson, K. D., Li, X. & Weiss, D. S. Imaging single atoms in a three-dimensional array. *Nature Physics* **3,** 556–560 (2007).

31. Karski, M *et al.* Nearest-Neighbor Detection of Atoms in a 1D Optical Lattice by Fluorescence Imaging. *Physical Review Letters* **102,** 053001 (2009).

32. Sherson, J. F. *et al.* Single-atom-resolved fluorescence imaging of an atomic Mott insulator. *Nature* **467,** 68–72 (2010).

33. Gibbons, M. J., Hamley, C. D., Shih, C.-Y. & Chapman, M. S. Nondestructive Fluorescent State Detection of Single Neutral Atom Qubits. *Physical Review Letters* **106,** 133002 (2011).

34. Fuhrmanek, A, Bourgain, R, Sortais, Y. R. P. & Browaeys, A. Free-Space Lossless State Detection of a Single Trapped Atom. *Physical Review Letters* **106,** 133003 (2011).

35. Poldy, R, Buchler, B & Close, J. Single-atom detection with optical cavities. *Physical Review A* **78** (2008).
36. Gehr, R. *et al.* Cavity-Based Single Atom Preparation and High-Fidelity Hyperfine State Readout. *Physical Review Letters* **104,** 203602 (2010).
37. Bücker, R *et al.* Single-particle-sensitive imaging of freely propagating ultracold atoms. *New Journal of Physics* **11,** 103039 (2009).
38. Fuhrmanek, A *et al.* Imaging a single atom in a time-of-flight experiment. *New Journal of Physics* **12,** 053028 (2010).
39. Henkel, F *et al.* Highly Efficient State-Selective Submicrosecond Photoionization Detection of Single Atoms. *Physical Review Letters* **105** (2010).
40. Streed, E. W., Jechow, A., Norton, B. G. & Kielpinski, D. Absorption imaging of a single atom. *Nature Communications* **3,** 933–5 (2012).
41. Muessel, W. *et al.* Optimized absorption imaging of mesoscopic atomic clouds. *Applied Physics B* **113,** 69–73 (2013).
42. Ockeloen, C. F., Tauschinsky, A. F., Spreeuw, R. J. C. & Whitlock, S. Detection of small atom numbers through image processing. *Physical Review A* **82,** 061606 (2010).
43. Zhang, H. *et al.* Collective State Measurement of Mesoscopic Ensembles with Single-Atom Resolution. *Physical Review Letters* **109,** 133603 (2012).
44. Grünzweig, T, Hilliard, A, McGovern, M & Andersen, M. F. Near-deterministic preparation of a single atom in an optical microtrap. *Nature Physics* **6,** 951–954 (2010).
45. Serwane, F *et al.* Deterministic Preparation of a Tunable Few-Fermion System. *Science* **332,** 336–338 (2011).
46. Schlosser, N, Reymond, G, Protsenko, I & Grangier, P. Sub-poissonian loading of single atoms in a microscopic dipole trap. *Nature* **411,** 1024–1027 (2001).
47. Kuhr, S. *et al.* Deterministic delivery of a single atom. *Science* **293,** 278–280 (2001).
48. Hanggi, P., Talkner, P. & Borkovec, M. Reaction-rate theory: fifty years after Kramers. *Reviews of Modern Physics* **62,** 251–341 (1990).
49. Pollak, E. & Talkner, P. Reaction rate theory: What it was, where is it today, and where is it going? *Chaos: An Interdisciplinary Journal of Nonlinear Science* **15,** 026116 (2005).
50. Weiner, J., Bagnato, V. S., Zilio, S. & Julienne, P. S. Experiments and theory in cold and ultracold collisions. *Reviews of Modern Physics* **71,** 1 (1999).
51. Jung, P. & Hanggi, P. Amplification of small signals via stochastic resonance. *Physical Review A* **44,** 8032 (1991).
52. Nicolis, C. Stochastic aspects of climatic transitions—response to a periodic forcing. *Tellus* **34,** 1–9 (1982).
53. Hanggi, P. Stochastic resonance in biology how noise can enhance detection of weak signals and help improve biological information processing. *ChemPhysChem* **3,** 285–290 (2002).

54. McDonnell, M. D. & Abbott, D. What Is Stochastic Resonance? Definitions, Misconceptions, Debates, and Its Relevance to Biology. *PLoS Computational Biology* **5,** e1000348 (2009).
55. Moss, F. Stochastic resonance and sensory information processing: a tutorial and review of application. *Clinical Neurophysiology* **115,** 267–281 (2004).
56. Hume, D *et al.* Accurate Atom Counting in Mesoscopic Ensembles. *Physical Review Letters* **111,** 253001 (2013).
57. Scully, M. O. & Zubairy, M. S. *Quantum optics* 6th ed. (Cambridge University Press, Cambridge, 2008).
58. Fox, M. *Quantum optics: an introduction* (Oxford University Press Inc., New York, 2006).
59. Allen, L. & Eberly, J. H. *Optical Resonance and Two-Level Atoms* (Dover Publications, Inc., New York, 1987).
60. Frisch, R. Experimenteller Nachweis des Einsteinschen Strahlungsrückstosses. *Z. Physik* **86,** 42–48 (1933).
61. Lett, P. D. *et al.* Optical molasses. *JOSA B* **6,** 2084–2107 (1989).
62. Foot, C. J. *Atomic Physics* (Oxford University Press Inc., 2005).
63. Lett, P. D. *et al.* Observation of atoms laser cooled below the Doppler limit. *Physical Review Letters* **61,** 169–172 (1988).
64. Salomon, C, Dalibard, J., Phillips, W. D., Clairon, A & Guellati, S. Laser cooling of cesium atoms below 3 $\mu$K. *EPL (Europhysics Letters)* **12,** 683 (1990).
65. Cohen-Tannoudji, C. N. & Phillips, W. D. New Mechanisms for Laser Cooling. *Physics Today* **43,** 33 (1990).
66. Wineland, D. J., Dalibard, J. & Cohen-Tannoudji, C. Sisyphus cooling of a bound atom. *JOSA B* **9,** 32–42 (1992).
67. Cohen-Tannoudji, C. & Guéry-Odelin, D. *Advances in Atomic Physics* (World Scientific Publishing Co. Pte. Ltd., 2011).
68. Monroe, C., Swann, W, Robinson, H & Wieman, C. Very cold trapped atoms in a vapor cell. *Physical Review Letters* **65,** 1571–1574 (1990).
69. Metcalf, H. J. & Straten, P. V. D. *Laser Cooling and Trapping* (Springer Verlag GmbH, 1999).
70. Prentiss, M *et al.* Atomic-density-dependent losses in an optical trap. *Optics letters* **13,** 452–454 (1988).
71. Sesko, D, Walker, T, Monroe, C., Gallagher, A & Wieman, C. Collisional losses from a light-force atom trap. *Physical Review Letters* **63,** 961–964 (1989).
72. Grimm, R., Weidemüller, M. & Ovchinnikov, Y. B. Optical dipole traps for neutral atoms. *Advances in atomic, molecular, and optical physics* **42,** 95–170 (2000).
73. Metcalf, H. J. & van der Straten, P. Laser cooling and trapping of atoms. *JOSA B* **20,** 887–908 (2003).
74. Alt, W. *et al.* Single atoms in a standing-wave dipole trap. *Physical Review A* **67** (2003).

75. Puppe, T *et al.* Trapping and Observing Single Atoms in a Blue-Detuned Intracavity Dipole Trap. *Physical Review Letters* **99,** 013002 (2007).
76. Goldwin, J, Trupke, M, Kenner, J, Ratnapala, A & Hinds, E. A. Fast cavity-enhanced atom detection with low noise and high fidelity. *Nature Communications* **2,** 418–6 (2011).
77. Bakr, W. S. *et al.* Probing the superfluid-to-Mott insulator transition at the single-atom level. *Science* **329,** 547–550 (2010).
78. Fuhrmanek, A, Bourgain, R, Sortais, Y. R. P. & Browaeys, A. Light-assisted collisions between a few cold atoms in a microscopic dipole trap. *Physical Review A* **85,** 062708 (2012).
79. Chanelière, T., Meunier, J.-L., Kaiser, R., Miniatura, C. & Wilkowski, D. Extra-heating mechanism in Doppler cooling experiments. *JOSA B* **22,** 1819–1828 (2005).
80. Browaeys, A *et al.* Two body loss rate in a magneto-optical trap of metastable He. *The European Physical Journal D-Atomic, Molecular, Optical and Plasma Physics* **8,** 199–203 (2000).
81. Anderson, M., Petrich, W, Ensher, J. & Cornell, E. Reduction of light-assisted collisional loss rate from a low-pressure vapor-cell trap. *Physical Review A* **50,** R3597–R3600 (1994).
82. Julienne, P. S. & Vigué, J. Cold collisions of ground-and excited-state alkali-metal atoms. *Physical Review A* **44,** 4464 (1991).
83. Wallace, C. D., Dinneen, T. P., Tan, K.-Y. N., Grove, T. T. & Gould, P. L. Isotopic difference in trap loss collisions of laser cooled rubidium atoms. *Physical Review Letters* **69,** 897–900 (1992).
84. Hodapp, T. W. *et al.* Three-dimensional spatial diffusion in optical molasses. *Applied Physics B* **60,** 135–143 (1995).
85. Adams, C. S. & Riis, E. Laser cooling and trapping of neutral atoms. *Progress in Quantum Electronics* **21,** 1–79 (1997).
86. Joffe, M. A., Ketterle, W., Martin, A. & Pritchard, D. E. Transverse cooling and deflection of an atomic beam inside a Zeeman slower. *JOSA B* **10,** 2257–2262 (1993).
87. Larmore, L. *Introduction to Photographic Principles* 2nd ed. (Dover Publications, Inc., New York, 1965).
88. Saleh, B. E. A. & Teich, M. C. *Fundamentals of Photonics* (John Wiley and Sons, Inc., New Jersey, 2007).
89. Wallace, C. D. *et al.* Measurements of temperature and spring constant in a magneto-optical trap. *JOSA B* **11,** 703–711 (1994).
90. Arrhenius, S. Über die Reactionsgeschwindigkeit bei der Inversion von Rohrzucker durch Säuren. *Z. Phys. Chem.* **4,** 226–248 (1889).
91. Eyring, H. The activated complex in chemical reactions. *J. Chem. Phys.* **3,** 107–115 (1935).
92. Kramers, H. A. Brownian motion in a field of force and the diffusion model of chemical reactions. *Physica* **7,** 284 (1940).
93. Van Kampen, N. G. *Stochastic processes in physics and chemistry* Third printing (Elsevier Science Publishers B.V., Amsterdam, 1984).

94. Trautz, M. Das Gesetz der Reaktionsgeschwindigkeit und der Gleichgewichte in Gasen. Bestätigung der Additivität von Cv-3/2R. Neue Bestimmung der Integrationskonstanten und der Moleküldurchmesser. *Zeitschrift für anorganische und allgemeine Chemie* **96,** 1–28 (1916).

95. Sompet, P, Carpentier, A. V., Fung, Y. H., McGovern, M & Andersen, M. F. Dynamics of two atoms undergoing light-assisted collisions in an optical microtrap. *Physical Review A* **88,** 051401 (2013).

96. Bardou, F, Bouchaud, J. P., Emile, O, Aspect, A & Cohen-Tannoudji, C. Subrecoil laser cooling and Levy flights. *Physical Review Letters* **72,** 203–206 (1994).

97. Marksteiner, S, Ellinger, K & Zoller, P. Anomalous diffusion and Lévy walks in optical lattices. *Physical Review A* **53,** 3409 (1996).

98. Katori, H., Schlipf, S. & Walther, H. Anomalous dynamics of a single ion in an optical lattice. *Physical Review Letters* **79,** 2221 (1997).

99. Sagi, Y., Brook, M., Almog, I. & Davidson, N. Observation of Anomalous Diffusion and Fractional Self-Similarity in One Dimension. *Physical Review Letters* **108** (2012).

100. Lutz, E. Beyond Boltzmann–Gibbs statistical mechanics in optical lattices. *Nature Physics* **9,** 615–619 (2013).

101. Lévy, P. *Calcul des probabilités* (Gauthier Villars, 1925).

102. Lutz, E. Anomalous diffusion and Tsallis statistics in an optical lattice. *Physical Review A* **67,** 051402 (2003).

103. Douglas, P, Bergamini, S & Renzoni, F. Tunable Tsallis Distributions in Dissipative Optical Lattices. *Physical Review Letters* **96,** 110601 (2006).

104. Tsallis, C. Possible generalization of Boltzmann-Gibbs statistics. *Journal of statistical physics* **52,** 479–487 (1988).

105. Leggett, A. J. *Quantum Liquids* (Oxford University Press Inc., New York, 2006).

106. McNamara, B. & Wiesenfeld, K. Theory of stochastic resonance. *Physical Review A* **39,** 4854 (1989).

107. Gammaitoni, L., Hanggi, P., Jung, P. & Marchesoni, F. Stochastic resonance. *Reviews of Modern Physics* **70,** 223–287 (1998).

108. Gammaitoni, L, Marchesoni, F, Martinelli, M, Pardi, L & Santucci, S. Phase shifts in bistable EPR systems at stochastic resonance. *Physics Letters A* **158,** 449–452 (1991).

109. Jung, P. & Hanggi, P. Stochastic nonlinear dynamics modulated by external periodic forces. *EPL (Europhysics Letters)* **8,** 505 (1989).

110. McNamara, B., Wiesenfeld, K. & Roy, R. Observation of stochastic resonance in a ring laser. *Physical Review Letters* **60,** 2626–2629 (1988).

111. Debnath, G, Zhou, T & Moss, F. Remarks on stochastic resonance. *Physical Review A* **39,** 4323 (1989).

112. Gammaitoni, L, Marchesoni, F, Menichella-Saetta, E & Santucci, S. Stochastic resonance in bistable systems. *Physical Review Letters* **62,** 349–352 (1989).

113. Vemuri, G. & Roy, R. Stochastic resonance in a bistable ring laser. *Physical Review A* **39,** 4668 (1989).

114. Zhou, T. & Moss, F. Analog simulations of stochastic resonance. *Physical Review A* **41,** 4255 (1990).

115. Presilla, C, Marchesoni, F & Gammaitoni, L. Periodically time-modulated bistable systems: Nonstationary statistical properties. *Physical Review A* **40,** 2105 (1989).

116. Dykman, M. I., Mannella, R, McClintock, P. V. & Stocks, N. G. Comment on "Stochastic resonance in bistable systems". *Physical Review Letters* **65,** 2606 (1990).

117. Hu, G., Haken, H & Ning, C. Z. A study of stochastic resonance without adiabatic approximation. *Physics Letters A* **172,** 21–28 (1992).

118. Jung, P. Periodically driven stochastic systems. *Physics Reports* **234,** 175–295 (1993).

119. Dykman, M. I., Mannella, R, McClintock, P. V. & Stocks, N. G. Phase shifts in stochastic resonance. *Physical Review Letters* **68,** 2985 (1992).

120. Gammaitoni, L & Marchesoni, F. Phase shifts in periodically modulated bistable potentials. *Physical Review Letters* **70,** 873 (1993).

121. Dykman, M. I., Mannella, R, McClintock, P. V. & Stocks, N. G. Dykman et al. reply. *Physical Review Letters* **70,** 874 (1993).

122. Jung, P. & Hanggi, P. Hopping and phase shifts in noisy periodically driven bistable systems. *Zeitschrift für Physik B Condensed Matter* **90,** 255–260 (1993).

123. Mohr, P. J., Taylor, B. N. & Newell, D. B. CODATA recommended values of the fundamental physical constants: 2010. *Reviews of Modern Physics* **84,** 1527–1605 (2012).

124. Steck, D. A. Rubidium 87 D Line Data. *available online at http://steck.us/alkalidata* (revision 2.1.4, 23 December 2010).